

Spin and magnetization dependent two-photon photoemission from ultrathin ferromagnetic cobalt films

Dissertation

zur Erlangung des akademischen Grades
doctor rerum naturalium (Dr. rer. nat.)

vorgelegt der

Naturwissenschaftlichen Fakultät II
der Martin-Luther-Universität Halle-Wittenberg

von Herrn Cheng-Tien Chiang
geb. am 26. Juni 1984 in Taipeh, Taiwan

angefertigt am

Max-Planck-Institut für Mikrostrukturphysik
in Halle an der Saale

Gutachter

1. Prof. Dr. J. Kirschner
2. Prof. Dr. W. Widdra
3. Prof. Dr. Th. Fauster

Halle (Saale), 30. Juni 2010

Tag der Verteidigung: 31. Januar 2011

Contents

1	Introduction	1
2	Basic concepts of two-photon photoemission from magnetic thin films	4
2.1	Two-photon photoemission	4
2.2	Magnetic dichroism in photoemission	6
2.3	Spin-polarized photoemission	10
2.4	Quantum well states in ultrathin films	12
2.5	Cobalt films on Cu(001)	13
3	Experimental setup	15
3.1	Femtosecond laser system	15
3.2	Angle-resolved photoemission	17
3.3	Spin-polarization analysis	17
3.4	Sample preparation	20
4	Results	22
4.1	Film growth monitored by photoemission	22
4.2	Magnetic dichroism in photoemission	24
4.3	Spin-resolved measurements	30
4.3.1	Films grown at 310 K	30
4.3.2	Films grown at 170 K	32
4.4	Spin-resolved magnetic dichroism	36
4.5	Excitation power dependence	39
5	Discussion	43
5.1	Characterization of unoccupied quantum well states	43
5.1.1	Energy dispersion	43
5.1.2	Spin character and spin-orbit coupling	48
5.2	Tuning interference between photoexcitation channels in ferromagnets	53
5.3	Comparison between one- and two-photon photoemission	59
5.4	Relation between spin-polarization and magnetic dichroism	66
5.5	Photoemission intensity oscillations as a function of cobalt thickness	70

5.6	Information depth of two-photon photoemission	73
6	Conclusion and outlook	75

Chapter 1

Introduction

The electronic structure of materials is fundamental in understanding their electrical, optical, and magnetic properties. Besides the energy and momentum of electrons, the electron spin offers an additional degree of freedom and introduces the exchange and spin-orbit interaction into the electronic structure. The exchange interaction is connected to the Pauli-exclusion principle, and results in an effective coupling between the spins of electrons. The spin-orbit interaction is based on the relativistic coupling between the spin and the motion of a single electron. Both interactions are two essential ingredients of magnetism and spin-dynamics. Their simultaneous presence leads to diverse magneto-transport and magneto-optical phenomena such as the anomalous Hall effect [1, 2] and the Faraday effect [3–5]. Spin-orbit coupling gives rise to the magnetocrystalline anisotropy in magnetic systems [6–9], and in non-magnetic systems it contributes significantly to spin-dependent transport [10–14]. As also intensively studied in recent years, the spin-orbit interaction plays a crucial role in optically driven spin-dynamics [15], in the dispersion of spin-waves [16] as well as in non-collinear spin structures at surfaces [17–20]. It is therefore important to have analytical access to spin-orbit coupling in a system of interest. For ferromagnets, the spin-orbit coupling in the electronic structure can be analyzed with energy and momentum resolution by observation *e. g.* of the intensity change of spectra features in angle-resolved photoelectron spectroscopy upon magnetization reversal (magnetic dichroism) [21, 22]. For non-magnetic materials the effects of spin-orbit coupling can be revealed in spin-resolved photoemission measurements [23–25]. The spin-analysis of photoelectrons from ferromagnets provides a direct observation of the exchange interaction in the electronic structure [26, 27]. Photoelectron spectroscopy combined with spin-resolution and magnetic dichroic methods is therefore a very general tool to investigate the spin-orbit coupling in materials.

Although the influence of spin-orbit interaction to photoemission processes has been shown from more than two decades [28–31], most photoemission experiments at solid state surfaces could only detect the spin-orbit coupling in occupied electronic states. It is schematically shown in Fig. 1.1 that both conventional valence as well as core-level photoemission couple the initial states below the Fermi level to the final states above the vacuum

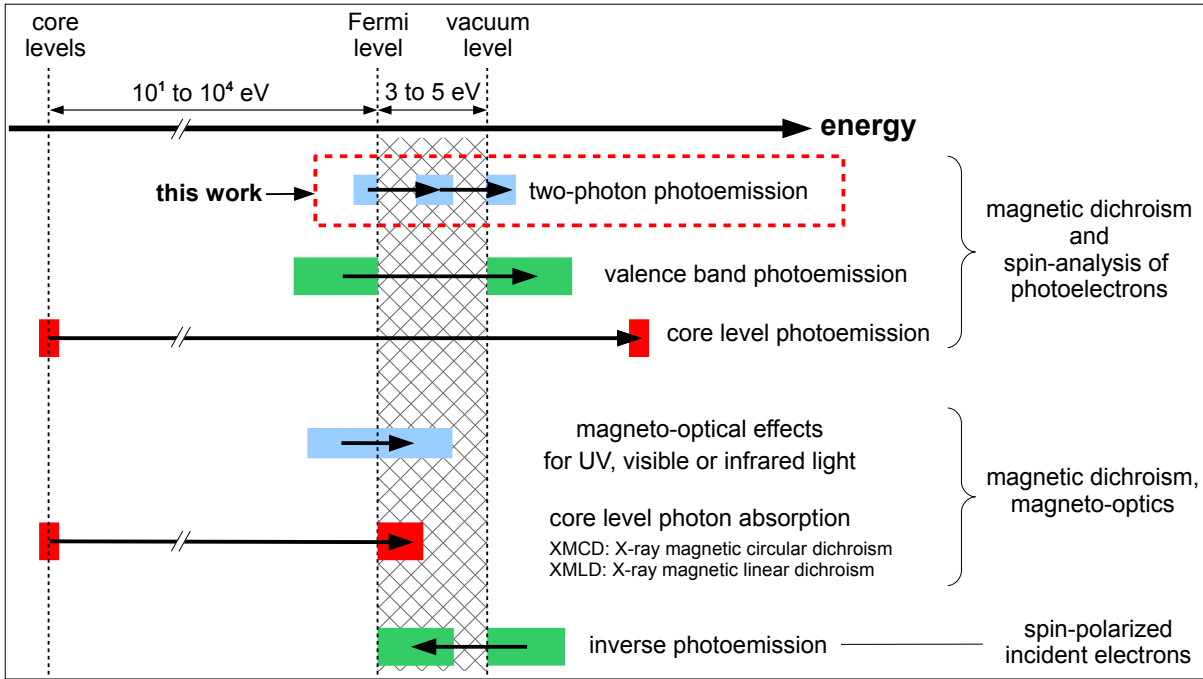


Figure 1.1: Comparison between selected methods for investigating the electronic structure of materials. The relevant initial and final states are marked by the color blocks. The transitions are marked by arrows. The magnetic and spin-resolved information can be gained by additional methods written on the right.

level. These linear photoemission processes can therefore barely give any information on the unoccupied states between the Fermi and vacuum levels (gray-hatched area). These unoccupied states are relevant *e. g.* to optically driven spin- and magnetization-dynamics. The electronic states within this energy range can also be probed with momentum resolution by inverse photoemission which, however, not yet be capable to resolve the spin-orbit coupling despite its spin-resolution [32, 33].

In this work, we use spin-resolved two-photon photoemission (2PPE) to probe unoccupied electronic states at magnetic surfaces. The 2PPE process is sensitive to the intermediate states located between the Fermi and vacuum levels (Fig. 1.1). 2PPE has established itself as a powerful method to study the unoccupied electronic structure and the dynamics of excited electrons at surfaces [34–36]. There are also several previous investigations of magnetic systems using 2PPE [37]. Wallauer *et al.* investigated the exchange splitting of image potential states around 4 eV above the Fermi level on Fe/Cu(001) as well as Co/Cu(001) [38]. Schmidt *et al.* studied the spin-dynamics of excited electrons in the image potential states on Fe/Cu(001) in the femtosecond time scale [39]. Aeschlimann *et al.* probed the spin-dependent lifetime of unoccupied states in Co/Cu(001) around 0.6-1.1 eV above the Fermi level [40] and Andreyev *et al.* analyzed the influence of unoccupied image resonance states to the spin-polarization in 2PPE [41]. Recently, Pickel *et al.* utilized the image potential states as sensors for detecting the exchange and spin-orbit interaction in the occupied electronic structure of cobalt and iron films [42, 43]. They observed evidence of exchange splitting in Fe/Cu(001) films above the Curie temperature [42] and

magnetic linear dichroism from the spin-orbit coupling in the occupied electronic states of Co/Cu(001) films [43]. Hild *et al.* [44] and Nakagawa *et al.* [45] observed magnetic circular dichroism in the total yield of two-photon photoemission, which did not resolve specific intermediate electronic states. In our spectroscopic two-photon photoemission experiments, by analyzing the photoelectrons with energy-, angle- and spin-resolution, we identify unoccupied quantum well states in ultrathin cobalt films grown on Cu(001) surfaces. We observe magnetic dichroic signals from the excited quantum well states [46]. This is systematically examined by varying the cobalt thickness in experiments and by comparison to the theoretical band structure. We also compare our experimental results with theoretical photoemission calculations [47].

By analyzing the photoelectron spin polarization and using it as an additional information channel, we further elucidate the role of the intermediate quantum well states in the two-photon photoexcitation process. Significant differences are observed when comparing the 2PPE to the one-photon photoemission (1PPE) measurements, in which electrons are excited directly from the occupied states without the influence of any intermediate states. Our observations not only provide insight into the spin-dependent two-photon photoemission processes but are also generally relevant to nonlinear optical excitations in magnetic systems. These excitation processes can be influenced by the exchange interaction in the intermediate states, possibly strongly modulating the spin-polarization of excited states.

This work is organized as follows. In chapter 2, two-photon photoemission is introduced, and basic concepts of magnetic dichroism and spin-resolved photoemission are described. In addition, the properties of cobalt thin films on Cu(001) are summarized. In chapter 3, the experimental details are described, and, in chapter 4, the results are presented. The results of our investigations are discussed in chapter 5. Finally, the conclusions are presented.

Chapter 2

Basic concepts of two-photon photoemission from magnetic thin films

In this chapter, the basic concepts underlying our experimental investigations are summarized. First, the results of perturbation theory for one- and two-photon photoemission processes are shown in section 2.1. This allows us to identify the signatures of the electronic structure in the photoemission spectra. Then, the effect of sample magnetization to photoemission is introduced in section 2.2, based on the concepts of hybridization between electronic states induced by spin-orbit coupling. This is followed by an introduction to the spin-polarization analysis of photoelectrons in section 2.3, which gives access to the spin-resolved band structure and allows to disentangle the influence of exchange and spin-orbit interaction in the electronic structure. In section 2.4, the quantum well states, which are the electronic states confined in thin films, are introduced. Finally in section 2.5, the well-known structural, magnetic as well as electronic properties of cobalt thin films grown on Cu(001) is summarized.

2.1 Two-photon photoemission

Photoemission experiments provide access to the electronic structure of various systems, ranging from atomic and molecular gases to solid state materials [48–50]. Modern photoemission spectroscopy relies on a well-characterized light source and a high resolution electron energy analyzer. Both of them are currently in remarkable progress aiming at attosecond time resolution and milli-electron-volt energy resolution [51–54].

The photoemission process is based on the coupling between incident electric field and the electronic states in the system. The current of photoemitted electrons can be derived perturbatively when the incident electric field is much weaker than the ionic potential that binds the electrons. Under this circumstance and when we restrict ourselves to the single particle excitation picture, the number of photoelectrons per unit time interval (I)

emitted with certain momentum, kinetic energy and spin (p_{\parallel} , E_k , s) can be obtained by the second order expansion of the population in the initially unoccupied states above the vacuum level in terms of the incident electric field, up to a proportional constant, by [48–50]:

$$I^{1PPE}(p_{\parallel}, s, E_k = E_f - \Phi) \propto |\langle \Psi_f | \Delta | \Psi_i \rangle|^2 \delta(E_f - E_i - h\nu). \quad (2.1)$$

Here Ψ_i and Ψ_f are the electron initial and final state wave function at energy E_i and E_f . Δ is the interaction operator between electronic states and the incident light with photon energy $h\nu$, which is often approximated by the electric dipole interaction $\Delta = -\vec{E} \cdot \vec{\mu}$ between the incident electric field \vec{E} and the electric dipole moment $\vec{\mu}^{fi}$ between the electronic states Ψ_i and Ψ_f [48–50, 55]. Here $\vec{\mu} = -e\vec{r}$ is the electric dipole operator, with e the electron charge and \vec{r} the position operator, and $\vec{\mu}^{fi} = \langle \Psi_f | \vec{\mu} | \Psi_i \rangle$ is its expectation value between states Ψ_i and Ψ_f . This coupling leads to selective excitation of certain transition between electronic states Ψ_i and Ψ_f by polarized light, as formulated by the dipole selection rules [56, 57]. Φ is the sample work function. p_{\parallel} and E_k are the photoelectron momentum parallel to the sample surface and its kinetic energy, which can be measured by the detection of photoelectrons using an electrostatic energy analyzer (see section 3.2). We use s to indicate the component of spin of photoelectrons along the measured direction which can only be $\pm\hbar/2$ for the case of spin-up and spin-down. In Eq. 2.1 we consider only the elastic transition, as indicated by the delta function $\delta(E_f - E_i - h\nu)$ that the initial and final states are separated by exact the same amount of energy as the incident photon energy (Fermi golden rule). The photoemission spectrum is usually shown by the number of collected photoelectrons as a function of kinetic energy E_k or parallel momentum p_{\parallel} (or wave vector $k_{\parallel} = p_{\parallel}/\hbar$). In an angle-resolved photoemission measurement, photoelectrons are collected at several off-normal angles θ around the sample surface, providing the distribution of photoelectrons over parallel wave vector k_{\parallel} as derived by $k_{\parallel} = \sqrt{2mE_k/\hbar^2} \sin \theta$ (m : electron mass) [58].

By relating the photoelectron wave vector k_{\parallel} to the momentum p_{\parallel} through $p_{\parallel} = \hbar k_{\parallel}$ and by the wave matching condition at the surface between the outgoing photoelectron and the wave function of electronic states in the sample (or at the sample surface) [49], the wave vector of the electronic states parallel to the surface (k_{\parallel}^{in}) can be determined up to an additional constant of reciprocal lattice vector parallel to the surface (G_{\parallel}). This relation reads: $k_{\parallel}^{in} = k_{\parallel} + G_{\parallel}$ [49]. From the kinetic energy of photoelectrons E_k , surface work function Φ and the employed photon energy $h\nu$, the energy of the initial state E_i which is involved in the photoemission process is obtained. The dispersion of electronic state energy E_i versus the parallel wave vector k_{\parallel}^{in} constitutes the band structure information in the angle-resolved photoemission spectroscopy (ARPES) with fixed photon energy. In this work, the dispersion of quantum well state in the cobalt thin films will be shown in Fig. 5.3. If the complete energy dispersion including the wave vector perpendicular to the surface k_{\perp}^{in} is required, one may need to (i) have an input from the calculated final state dispersion and a photon energy dependent study [59], or (ii) investigate different surface

orientations and search for energy coincidence of features from the electronic bands [60].

In Eq. 2.1, the final states are located above the initial states by one photon energy and we call this process one-photon photoemission (1PPE). If we expand perturbatively the photoelectron current due to the incident light to the fourth-order of the electric field, there is additionally a contribution as [55, 61, 62]:

$$I^{2PPE}(p_{\parallel}, s, E_k = E_f - \Phi) \propto \left| \sum_m \frac{\langle \Psi_f | \Delta | \Psi_m \rangle \langle \Psi_m | \Delta | \Psi_i \rangle}{E_m - E_i - h\nu} \right|^2 \delta(E_f - E_i - 2h\nu). \quad (2.2)$$

Here Ψ_m is an intermediate state wave function at energy E_m . The contribution from the initial states are located in the photocurrent I^{2PPE} at twice the photon energy above the initial state energy and this process is called two-photon photoemission (2PPE). Since there are additional intermediate states involved in 2PPE, one can obtain information on the originally unoccupied electronic states above the Fermi level. To distinguish the spectral features of the initial states from those of the intermediate states, it is helpful to investigate the position of spectral features as a function of photon energy. In the case without specific resonance between continuous bands, the energy of spectral features due to the initial state should disperse with twice the amount of the change in photon energy, whereas the features from the intermediate states should disperse with the same amount as the change in the photon energy [43, 62–64]. An other method to distinguish the features of intermediate states from those of the initial states is to compare the two-photon photoemission spectrum obtained with photon energy $h\nu$ to the one-photon photoemission spectrum with doubled photon energy $2h\nu$, which results from the same initial and final states and is not influenced by the intermediate states explicitly. This method will be explored and discussed in section 5.3.

In addition, one would expect a spin dependence in the transition going through the spin dependent intermediate states in 2PPE. In the non-relativistic approximation with incident linearly polarized light, the optical excitation conserves the electron spin and therefore only the electrons in the initial state with spin direction parallel to that of the intermediate state can be excited into the intermediate state. In this picture, a spin-polarized intermediate state effectively selects the spin of photoelectrons. This effect will be discussed in section 5.3.

2.2 Magnetic dichroism in photoemission

In magnetic materials, the intensity of photoemission can strongly depend on the relative orientation of sample magnetization with respect to the incident polarization of light. The mechanism leading to the magnetization dependent optical transition rate is the combined influence of the exchange interaction and spin-orbit coupling in the electronic structure [3, 65]. This results in diverse magneto-optical phenomena [3–5] as well as magnetic dichroism in X-ray absorption [28] and photoemission [21, 29, 66]. In the case of X-ray

absorption, magnetic dichroism has been used to image magnetic domains with element resolution in the nanometer scale [67] and to obtain the absolute values of the orbital and spin magnetic moments [30, 31]. The magnetic dichroism observed in photoemission spectroscopy is a tool to resolve the influence of spin-orbit coupling in the electronic band structure of magnetic materials, which leads to the hybridization of electronic bands with different spatial symmetry properties as well as different electron spins [21, 65].

Experimentally, the magnetic dichroic signal in photoemission is represented by the normalized intensity change under sample magnetization reversal A (dichroic asymmetry), as determined by the magnetization dependent photoemission intensities $I_{\pm M}$. For incident circularly (A_{MCD}) and linearly polarized light (A_{MLD}) we have magnetic circular and magnetic linear dichroism according to [29]:

$$A_{MCD,MLD} = (I_{+M} - I_{-M}) / (I_{+M} + I_{-M}). \quad (2.3)$$

In the literature, the magnetic circular and linear dichroism are usually measured in different geometries, the former with circularly polarized light and sample magnetization *in* the optical plane whereas the latter with incident p -polarized light and sample magnetization *perpendicular* to the optical plane [21]. In our experiment we use the identical geometry for both circularly and linearly polarized incident light, namely, the sample magnetization in the optical plane for both cases (Fig. 3.2). As will be shown by the experiments in section 4.2 and discussed in section 5.2, this geometry indeed yields a magnetic linear dichroism and can actually give us detailed information about the electronic structure. Despite the difference in the experimental geometries, all the magnetic dichroic phenomena in angle-resolved photoemission from valence band structure appears when there is an interference between photoexcitation channels [65, 68]. This will be deduced here for our experimental geometry in Fig. 3.2, that is, sample magnetization parallel to the surface and in the optical plane, and the photoelectrons are collected normal from the surface [68]. For the other cases the reader is referred to the experiments from Kuch and Rampe *et al.* [69, 70] and analytical relations from Henk *et al.* [65, 68].

In the following, we use an analytical description for the magnetic dichroism in one-photon photoemission (1PPE) within the electric dipole approximation. The electric field of incident light couples the transition dipole matrix element between electronic states, and the coupling results in the photoelectron current described by Eq. 2.1 with $\Delta = -\vec{E} \cdot \vec{\mu}$. Here we use $\vec{\mu}^{fi}$ for the expectation value of the transition dipole operator between initial and final states, and Eq. 2.1 reads [49]:

$$\begin{aligned} I^{fi}(E_f) &\propto \left| \vec{E} \cdot \vec{\mu}^{fi} \right|^2 = (\vec{E} \cdot \vec{\mu}^{fi})(\vec{E} \cdot \vec{\mu}^{fi})^* \\ &= \left| E_{\perp} \mu_{\perp}^{fi} \right|^2 + \left| E_{\parallel,p} \mu_{\parallel,p}^{fi} \right|^2 + \left| E_{\parallel,s} \mu_{\parallel,s}^{fi} \right|^2 \\ &\quad + 2\Re \left[E_{\perp} E_{\parallel,p}^* \mu_{\perp}^{fi} \mu_{\parallel,p}^{fi*} \right] + 2\Re \left[E_{\perp} E_{\parallel,s}^* \mu_{\perp}^{fi} \mu_{\parallel,s}^{fi*} \right] \\ &\quad + 2\Re \left[E_{\parallel,p} E_{\parallel,s}^* \mu_{\parallel,p}^{fi} \mu_{\parallel,s}^{fi*} \right]. \end{aligned} \quad (2.4)$$

Here $I^{fi}(E_f)$ is the one-photon photoemission (1PPE) intensity for a chosen initial (i) to final state (f) transition and is proportional to the square amplitude of the transition matrix element, which is the inner product of transition dipole moments $\vec{\mu}^{fi}$ and the incident electric field vector \vec{E} . From the first to the second line we decompose the electric field and transition dipole moment into the Cartesian coordinates as shown in Fig. 2.1a. Electric field components $E_{\parallel,p}$ and $E_{\parallel,s}$ are parallel to the surface and originate from the p - and the s -polarized incident light components. E_{\perp} is the electric field component perpendicular to the surface and originates solely from the incident p -polarized light component. The inner product of the electric field and the transition dipole moment contains only pairs along the same direction and therefore with the same subscript in our orthogonal basis of coordinates. The asterisk (*) indicates conjugation of a complex number. $\Re[z]$ represents the real part of the complex number z . In the above formula we consider only the elastic photoemission processes so that the initial state energy level E_i is located one photon energy ($h\nu$) lower than the final state energy level E_f . We see the interference effect in the last three terms of Eq. 2.4, each of which contains two mutually perpendicular components of the electric field, and they correspond to the interference between photoemission channels established by different components of the transition dipole moments. We schematically show these three channels in Fig. 2.1b.

The important information in Eq. 2.4 is a trace of the photoemission intensity back to the optical transition induced by specific Cartesian components of the dipole moment $\vec{\mu}^{fi}$. Due to the inner product of electric field and dipole moment, the electric field components E_{\perp} , $E_{\parallel,p}$ and $E_{\parallel,s}$ couple components of transition dipole moment μ_{\perp}^{fi} , $\mu_{\parallel,p}^{fi}$, and $\mu_{\parallel,s}^{fi}$ respectively, and through all of these channels the same initial $|\Psi_i\rangle$ and final states $|\Psi_f\rangle$ are coupled simultaneously. A selective excitation through one of these channels can be done by choosing one of the polarization component of electric field E_{\perp} , $E_{\parallel,p}$ or $E_{\parallel,s}$, which is the essence of the dipole selection rules [49, 56, 57]. By choosing a proper superposition of the polarization of light, we can simultaneously induce transitions through more than one of the channels described by μ_{\perp}^{fi} , $\mu_{\parallel,p}^{fi}$ and $\mu_{\parallel,s}^{fi}$ and consequently create an effect of interference in the final state population, as shown in Fig. 2.1b. The final state population is then measured by the photoemission intensity at the energy level E_f .

Depending on the symmetry properties of the sample crystal structure and the direction of the sample magnetization, some of the discussed interference terms may vanish. Combined with the chosen light polarization, this leads to different geometries which are employed for the different orientations of sample magnetization in the magnetic dichroic experiments [21, 70]. In our experiments on Co/Cu(001), the sample magnetization is parallel to the sample surface plane and aligned with the optical plane. The photoelectrons are detected normal to the surface (experimental geometry in Fig. 3.2). It can be shown, by using the symmetry property of initial and final states with respect to the mirror planes perpendicular to the optical plane [71–74], that the relevant interference terms in our geometry are reduced to the terms where $\mu_{\parallel,s}^{fi}$ and μ_{\perp}^{fi} simultaneously exist.

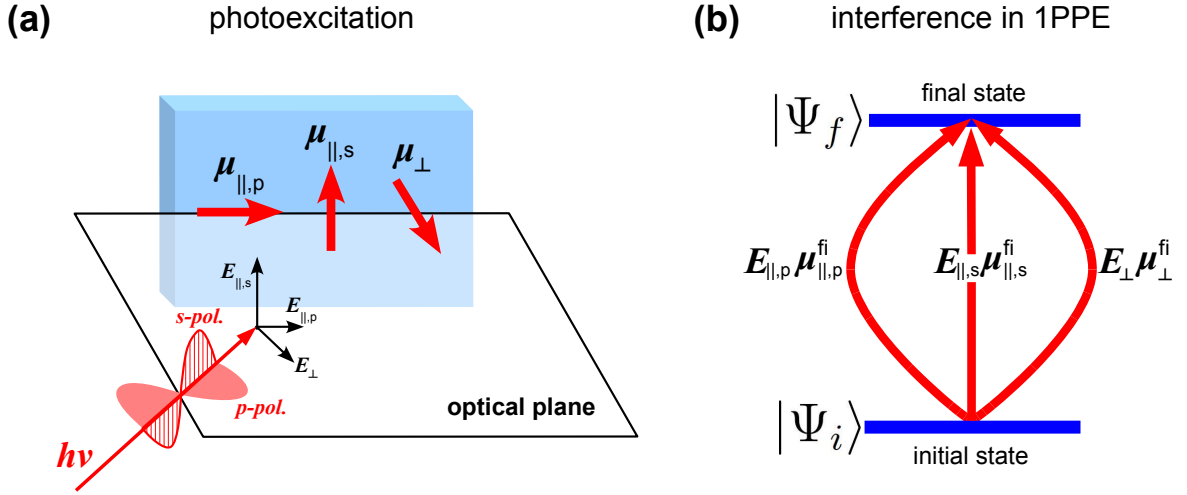


Figure 2.1: (a) Geometry of photoexcitation. The incident electric field is decomposed into E_{\perp} , $E_{\parallel,p}$ and $E_{\parallel,s}$ components. E_{\perp} is perpendicular to the sample surface, $E_{\parallel,p}$ and $E_{\parallel,s}$ are parallel to the sample surface. Both E_{\perp} and $E_{\parallel,p}$ are derived from the incident p -polarization. $E_{\parallel,s}$ is the s -polarized component. (b) Three different photoexcitation channels between the initial and final states in the transition matrix elements: $E_{\perp}\mu_{\perp}^{fi}$, $E_{\parallel,p}\mu_{\parallel,p}^{fi}$ and $E_{\parallel,s}\mu_{\parallel,s}^{fi}$.

The one-photon photoemission intensity now condenses from Eq. 2.4 into:

$$I^{fi}(E_f) \propto |E_{\perp}\mu_{\perp}^{fi}|^2 + |E_{\parallel,p}\mu_{\parallel,p}^{fi}|^2 + |E_{\parallel,s}\mu_{\parallel,s}^{fi}|^2 + 2\Re [E_{\perp}E_{\parallel,s}^*\mu_{\perp}^{fi}\mu_{\parallel,s}^{fi*}]. \quad (2.5)$$

As has been theoretically derived by Henk and Venus *et al.* [65, 68, 75] and experimentally verified [21, 43], the interference terms in photoemission intensity, the last term in Eq. 2.5, can give rise to magnetic dichroism in photoemission. This will be made clear in the following. In addition, the interference term in Eq. 2.5 depends on the details of the wave functions of initial and final states through the magnitude and phase of matrix elements μ_{\perp}^{fi} and $\mu_{\parallel,s}^{fi}$. If there is no spin-orbit coupling in the electronic structure, there will exist only one Cartesian component of the transition dipole moment pointing along one of the high symmetry directions of sample, hindering the simultaneous light induced coupling via different channels. These symmetry properties of electronic states, as have been shown by Henk *et al.* in analytical forms for magnetic dichroism in photoemission [65, 68], points to the spin-orbit coupling and the related hybridization between electronic states as a prerequisite of interference in photoemission in our geometry. This is in accordance with the general statement that the simultaneous existence of spin-orbit and exchange interaction is required for magnetic dichroism [21].

To describe the magnetic dichroic signal in photoemission upon sample magnetization reversal, approaches based on the symmetry operations are used in the literature [21, 70, 76, 77]. It is found that the electric field perpendicular to the magnetization and

lying in the sample surface plane ($E_{\parallel,s}$ in Eq. 2.5) changes its sign in the equivalent geometry when the sample magnetization is reversed. This is also in agreement with the analytical descriptions from Venus and Henk [65, 75] and points out a sign change of the corresponding transition dipole moment upon sample magnetization reversal ($\mu_{\parallel,s}^{fi}$ in Eq. 2.5). In our experimental geometry (Fig. 3.2), we have the consequent change in the photoemission intensity as the magnetization is reversed, following Eq. 2.5:

$$I^{fi,\pm M}(E_f) \propto \left| E_{\perp} \mu_{\perp}^{fi,+M} \right|^2 + \left| E_{\parallel,p} \mu_{\parallel,p}^{fi,+M} \right|^2 + \left| E_{\parallel,s} \mu_{\parallel,s}^{fi,+M} \right|^2 \pm 2\Re \left[E_{\perp} E_{\parallel,s}^* \mu_{\perp}^{fi,+M} \mu_{\parallel,s}^{fi,+M*} \right]. \quad (2.6)$$

The $+M$ index on the electric dipole moments refers quantities when the magnetization is along [110] crystalline direction of cobalt films. In addition, the material optical response such as refraction can be included by using Fresnel coefficients [68, 78] and will lead to an additional mixing of the real and imaginary parts of $\mu_{\perp}^{fi,+M} \mu_{\parallel,s}^{fi,+M*}$ in the magnetic dichroic signal [47, 68]. The magnetic dichroism can be deduced from Eq. 2.6 according to Eq. 2.3:

$$A_{MD}^{fi}(E_f) = \frac{2\Re \left[E_{\perp} E_{\parallel,s}^* \mu_{\perp}^{fi,+M} \mu_{\parallel,s}^{fi,+M*} \right]}{\left| E_{\perp} \mu_{\perp}^{fi,+M} \right|^2 + \left| E_{\parallel,p} \mu_{\parallel,p}^{fi,+M} \right|^2 + \left| E_{\parallel,s} \mu_{\parallel,s}^{fi,+M} \right|^2}. \quad (2.7)$$

To adapt the experimental geometry in Fig. 3.2, the incident circular polarization of light is assigned by $(E_{\perp}, E_{\parallel,s}, E_{\parallel,p}) = (E \sin \theta, \pm i E, E \cos \theta)$ with θ as the angle of incidence and the imaginary number $\pm i$ for left-/right-circular polarization. For the linearly polarized light such p - and s -polarization, the electric field components are described by $(E_{\perp}, E_{\parallel,s}, E_{\parallel,p}) = (E \sin \theta, 0, E \cos \theta)$, and $(E_{\perp}, E_{\parallel,s}, E_{\parallel,p}) = (0, E, 0)$ respectively. The p - and s -polarized components can be superimposed to form a linear polarization with a tunable angle α respect to the optical plane. The controllable angle α is a degree of freedom of the linearly polarized light and will be explored in the measurement of magnetic dichroism in Fig. 4.5. From Eq. 2.6 and Eq. 2.7 we can describe the magnetic dichroism in our experiments and they will be compared with the results in section 5.2.

2.3 Spin-polarized photoemission

The spin-polarization of photoelectrons is analyzed after the electron energy analyzer [26]. The electrostatic field in the energy analyzer influences the electron spin only negligibly in our case since the electrons move much slower than the speed of light ($E_K \leq 10$ eV, $v/c \leq 0.7\%$) [79]. Details of our spin-detector are specifically described in section 3.3. The spin-polarization of photoelectrons is defined as:

$$P = \frac{I_{+s} - I_{-s}}{I_{+s} + I_{-s}}. \quad (2.8)$$

$I_{\pm s}$ is the number of photoelectrons with spin-up and spin-down, along a defined direction in space (quantization axis). We use $\pm s$ here for the two opposite projections of electron spin on the quantization axis, and they correspond to the conventional symbol m_s in atomic physics. The spin-polarization is a three-dimensional vector quantity, and the spin-polarization in Eq. 2.8 is the projection of the spin-polarization vector along a quantization axis defined by the measurement [79].

The spin-polarization of photoelectrons has been analyzed for various systems. For non-magnetic materials, one can selectively photoexcite spin-polarized electrons from the spin-orbit split bulk electronic bands by polarized light [23, 26]. This process is described by the relativistic selection rule for photoemission which explicitly connects the electron spin with the transition dipole matrix elements [23, 24, 26]. In addition, on the surface of non-magnetic materials, the inversion symmetry is broken and there can exist Rashba-splitting in the electronic structure, resulting a shift in the electron wave vector between bands with opposite spins components [17, 18, 25]. For these cases, the spin-resolved photoemission spectra provide a way to measure the strength of spin-orbit coupling in the electronic structure.

For magnetic systems, spin-polarized photoemission has provided fundamental insight for an understanding of itinerant magnetism [26, 27], especially by measurements of the exchange splitting [80–84] and the absolute value of electron spin-polarization [85–89] in the valence band structure. Spin-resolved photoemission spectroscopy has also been used to resolve the spin-orbit splitting in the core levels in ferromagnets, which provides an explanation for the magnetic dichroic phenomena [66, 90–92].

Generally, the spin-polarization of photoelectrons depends on the sample magnetization as well as on the incident light polarization [65]. The effect of polarized light can be considered in analog to the case of non-magnetic systems according to the relativistic selection rules, while the magnetization plays a role due to the exchange interaction. Phenomenologically we can decompose the spin-polarization of photoelectrons into two components, one of them changes its sign as the sample magnetization is reversed (P_{ex}), and the other remains unchanged regardless of magnetization reversal (P_{so}). They are defined as the "exchange spin-polarization" (P_{ex}) and "spin-orbit spin-polarization" (P_{so}) [93, 94]. Here we use $P_{\pm M}^{\pm\sigma}$ for the photoelectron spin-polarization measured from two different sample magnetization directions $\pm M$ with left- or right-circularly polarized light $\pm\sigma$, and we use $I_{\pm s, \pm M}^{\pm\sigma}$ for the spin-up/down photoemission intensity from a sample magnetized along $\pm M$ with $\pm\sigma$ incident light. Then the exchange and spin-orbit spin-polarization P_{ex} and P_{so} are defined as [93, 94]:

$$P_{ex}^{\pm\sigma} = \frac{P_{+M}^{\pm\sigma} - P_{-M}^{\pm\sigma}}{2} = \frac{1}{2} \left(\frac{I_{+s, +M}^{\pm\sigma} - I_{-s, +M}^{\pm\sigma}}{I_{+s, +M}^{\pm\sigma} + I_{-s, +M}^{\pm\sigma}} - \frac{I_{+s, -M}^{\pm\sigma} - I_{-s, -M}^{\pm\sigma}}{I_{+s, -M}^{\pm\sigma} + I_{-s, -M}^{\pm\sigma}} \right) \quad (2.9)$$

$$P_{so}^{\pm\sigma} = \frac{P_{+M}^{\pm\sigma} + P_{-M}^{\pm\sigma}}{2} = \frac{1}{2} \left(\frac{I_{+s, +M}^{\pm\sigma} - I_{-s, +M}^{\pm\sigma}}{I_{+s, +M}^{\pm\sigma} + I_{-s, +M}^{\pm\sigma}} + \frac{I_{+s, -M}^{\pm\sigma} - I_{-s, -M}^{\pm\sigma}}{I_{+s, -M}^{\pm\sigma} + I_{-s, -M}^{\pm\sigma}} \right). \quad (2.10)$$

In the limit of vanishing magnetization, $P_{ex}^{\pm\sigma}$ reduces to zero since $P_{+M}^{\pm\sigma} = P_{-M}^{\pm\sigma}$, justifying its connection to the exchange interaction. The $P_{so}^{\pm\sigma}$, however, can remain finite in this ideal limit according to our definition, corresponding to the spin-dependent photoexcitation from non-magnetic systems. The quantities $P_{ex}^{\pm\sigma}$ and $P_{so}^{\pm\sigma}$ will be used to analyze the magnetic dichroism in our two-photon photoemission experiments in section 4.4 and discussed in section 5.4.

2.4 Quantum well states in ultrathin films

Modern technology makes it possible to fabricate smaller and thinner structures for device applications. In such small dimension of several nanometers, the electronic structure and consequently the optical and magnetic properties of materials can be dramatically different from the bulk materials. An ultrathin film system composed of several atomic layers is a typical example. Heteroepitaxy of thin layers on crystalline substrates can result in a spatially mismatched electronic structure due to different electronic properties of the substrate and the grown materials [95, 96]. As a consequence of the mismatch, there can be electronic states confined in the thin films, whose wave functions have only small penetration into the substrate, provided that the substrate has band gaps at the corresponding energies (see Fig. 2.2 as an example). Those confined electronic states in the film are named after the "quantum well states" which realize the particle in a box model of quantum mechanics [71, 96, 97].

For the case of metallic heteroepitaxy, if there is a band gap in the substrate within certain energy range, the electrons in the film within that energy range are strongly scattered by the periodic potential in the substrate, and then the electrons are reflected back to the film from the interface. At the surface of the film, if the electrons do not have enough energy to escape from the surface, the electrons within the film are reflected back to the film from the film surface by the surface potential barrier. The consequence of multiple reflection between the interface and surface is the existence of an electronic state with a standing-wave wave function in the film [96, 98, 99]. This picture is in analogy to the optical Fabry-Pérot interferometer [100, 101] and has provided quantitative understanding of the quantum well states and various types of surface states (phase-accumulation model, see Eq. 5.1) [98, 99, 102]. This model will be used later to evaluate the dispersion of the unoccupied quantum well states in Co/Cu(001) films and for comparison with the observations in section 5.1.1.

As a result of the spatial localization within the film, the binding energy of quantum well states depends strongly on the film thickness. This is because of the thickness dependent quantization condition for the electron wave function (Eq. 5.1), whose origin comes from the phase accumulation within the film and at the interface and surface (wave matching) [71, 99]. This thickness dependence can be used as a signature of quantum well states in electron spectroscopy experiments [96, 101] as well as in transport measure-

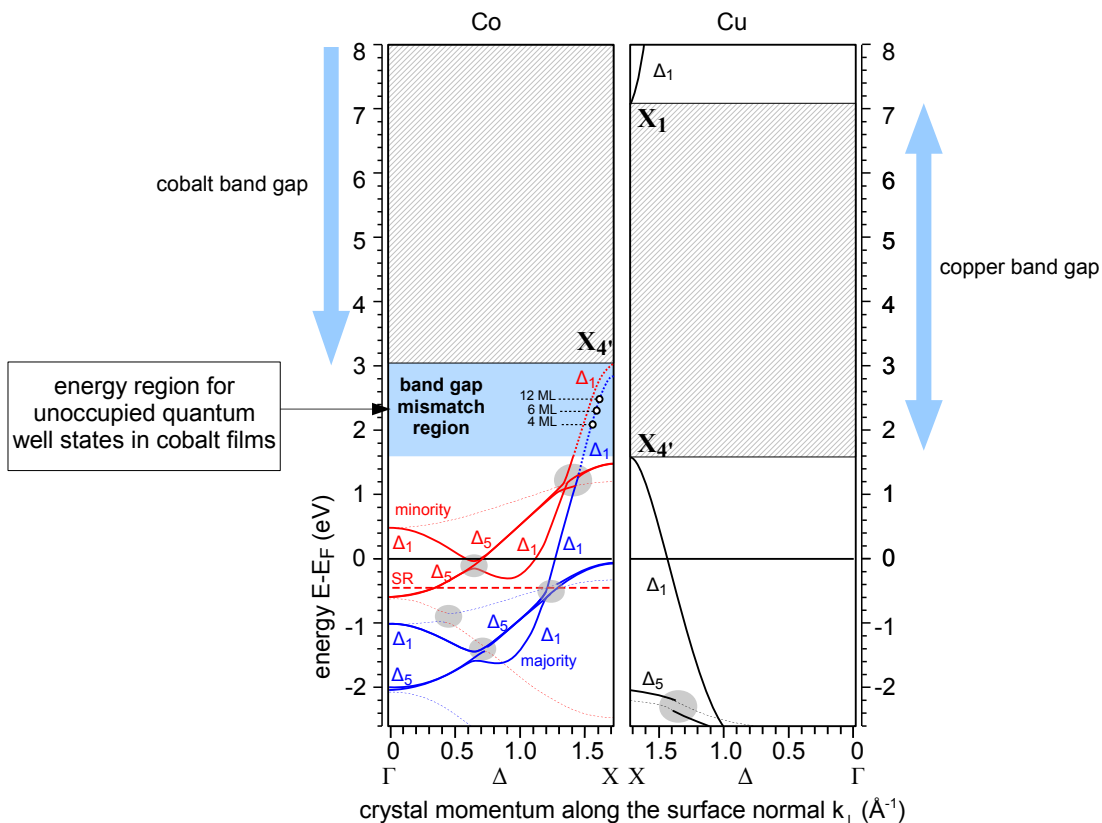


Figure 2.2: Relativistic face-centered cubic (fcc) bulk cobalt [47, 104] and copper band structure [105] along the [001] direction ($\Gamma - \Delta - X$ line in the fcc first Brillouin zone). The hatched area represents the band gap in copper and cobalt, and their mismatch from about 1.6 to 3.0 eV above the Fermi level is indicated by the blue area in the cobalt band structure. The cobalt band structure are adapted from Schmidt *et. al.* [104] for energy below the 1.2 eV, above which the unoccupied *sp*-band dispersion as well as the quantum well states energy are calculated by Henk for fct cobalt [47]. For simplicity, only the majority quantum well states for 4, 6 and 12 ML are shown. SR indicates the minority surface resonance state. Solid curves represent bands of dominant Δ_1 or Δ_5 symmetry, and dashed curves for Δ_2 or Δ_2' .

ments [103]. It is used in our photoemission study to identify the features of unoccupied quantum well states in Fig. 4.1.

2.5 Cobalt films on Cu(001)

The growth of cobalt thin films on Cu(001) has been widely studied by different microscopies [106, 107], diffraction and ion scattering experiments [108–117] as well as electron spectroscopies [111, 117, 118]. The cobalt layers grow in a layer-by-layer mode (Frank-van der Merve mode) after bilayer growth of first two monolayers (ML) on Cu(001) [106, 107, 112, 113, 117]. The structure is face-centered tetragonally distorted (fct) with interlayer spacing around 1.70 Å for the uppermost layer and 1.75 Å for the deeper layers [108–111, 118]. These values are smaller compared to the bulk interlayer spacing of face-centered cubic Co(001) (β -Co, 1.77 Å [119, 120]) and Cu(001) (1.805 Å [121]). The

lateral lattice constants of cobalt films follow the square lattice of Cu(001) up to 10-15 ML [108, 109, 118] until the tetragonal distortion starts to relax [115, 116]. After about 150 ML [122] the face-centered cubic structure gradually transforms into a hexagonal close-packed (hcp) structure, which is the bulk stable phase at 300 K. The growth of cobalt films at 150-170 K leads to small islands with structural disorder and rough morphology [114, 123]. The difference between 300 K and 150 K growth can be used to reveal the electronic states which are sensitive to the surface morphology (see section 5.3). Besides the growth mode, there are experimental observations indicating about 0.1-0.2 ML copper atoms on the surface of 300 K grown 5-7 ML cobalt films [113, 117] and a fast surface diffusion of substrate copper atoms through pin holes in 4 ML films after several minutes of annealing at 490 K [124]. Both of them are explained by the higher surface free energy of cobalt as compared to the sum of surface free energy of copper and the cobalt-copper interface energy [113, 117, 124].

The magnetic properties of fct cobalt films on Cu(001) have been characterized by various magneto-optical effects [112, 122, 125], spin-polarized electron spectroscopy and microscopy [126, 127] as well as ferromagnetic resonance (FMR) [128] and Brillouin light scattering experiments [129]. The films are ferromagnetic and have a Curie temperature that strongly depends on the film thickness. The Curie temperature rises above 300 K at around 1.8 ML and then increases to 600 K at around 3 ML [125, 129]. The easy axis of magnetization is in the surface plane (001) and parallel to the crystalline axis [110] and its equivalent directions [127–129]. This orientation of magnetization serves as the basis of our measurement geometry (Fig. 3.2).

The electronic structure of Co/Cu(001) thin films has been investigated by photoemission [22, 40, 41, 43, 81, 104, 130–134] and inverse photoemission spectroscopies [135, 136]. In the literature, several band structures have been calculated by various methods and used to interpret the experimental data [47, 104, 130, 132, 134, 137]. One of the example is shown in Fig. 2.2. It is instructive to notice their general features instead of comparing the precise energies of calculated electronic bands. There are generally majority and minority bands at different energies, signifying the exchange splitting in the electronic structure. The size of the exchange splitting, which can be estimated by the energy difference between majority and minority bands of the same spatial symmetry, can be large as 1 eV. Among the electronic bands, there are the less dispersive majority *d*-bands below the Fermi level and the minority *d*-bands near and above the Fermi level. Both the majority and minority *sp*-bands show significant dispersion up to around 2 eV above the Fermi level. As we will see later, these are the electronic bands from which the unoccupied quantum well states are derived. Besides, there is significant spin-orbit coupling within most of the bands. This is best seen from the hybridization between majority and minority bands, with a strength being estimated from the splitting at spin-orbit induced band gap up to 150 meV [43, 47, 104]. The spin-orbit coupling induced hybridization also occurs between bands of the same spin but different spatial symmetry properties [47].

Chapter 3

Experimental setup

In this chapter the main instruments in the experiments are introduced. This includes the femtosecond laser system and the electron energy analyzer with an electron spin-polarization analyzer. In the end the sample preparation procedure is described.

3.1 Femtosecond laser system

We use the frequency-doubled output from a Ti:sapphire oscillator as the light source for two-photon photoemission measurements ($\lambda \approx 400$ nm, $h\nu \approx 3.1$ eV). For one-photon photoemission, this output is again frequency-doubled ($\lambda \approx 200$ nm, $h\nu \approx 6.0$ eV). The setup of the oscillator and the optical path are shown in Fig. 3.1.

The Ti:sapphire crystal is pumped by a commercial laser (frequency-doubled Nd:YVO₄ laser, $\lambda=532$ nm, Millennia from Spectra-Physics). After mode-locking, the output of the Ti:sapphire oscillator has a repetition rate of 81 MHz, an average power around 700 mW, with central wavelength around 800 nm, and an estimated pulse width about 10 fs. This light beam is then focused into a nonlinear optical crystal (β -BaB₂O₄, BBO) to generate a frequency-doubled beam ($\lambda \approx 400$ nm), which is then guided into the ultrahigh vacuum (UHV) chamber. In addition, in the path there is a Mach-Zehnder interferometer, which can be used to split an optical pulse into two pulses with adjustable time delay with respect to each other [34], and several dielectric mirrors that control the phase between components of different wavelength within a pulse (chirp) [138]. The optical pulse width at the sample position in the UHV chamber is checked by the interferometric autocorrelation with the surface second-harmonic-generation (SSHG) signal [139], which gives an estimation of pulse width around 20 fs. The average power the frequency-doubled output at ≈ 400 nm can be varied up to 130 mW by inserting a $\lambda/2$ wave plate in front of the BBO crystal. This gives a maximum pulse energy of 1.6 nJ/pulse.

The linear and circular polarization of the incident light are controlled by achromatic $\lambda/2$ and $\lambda/4$ wave plates in the optical path before entering into the chamber (Fig. 3.1, inset). An optional setup for frequency-doubling can be inserted in order to obtain the light with wavelength ≈ 200 nm for one-photon photoemission experiments.

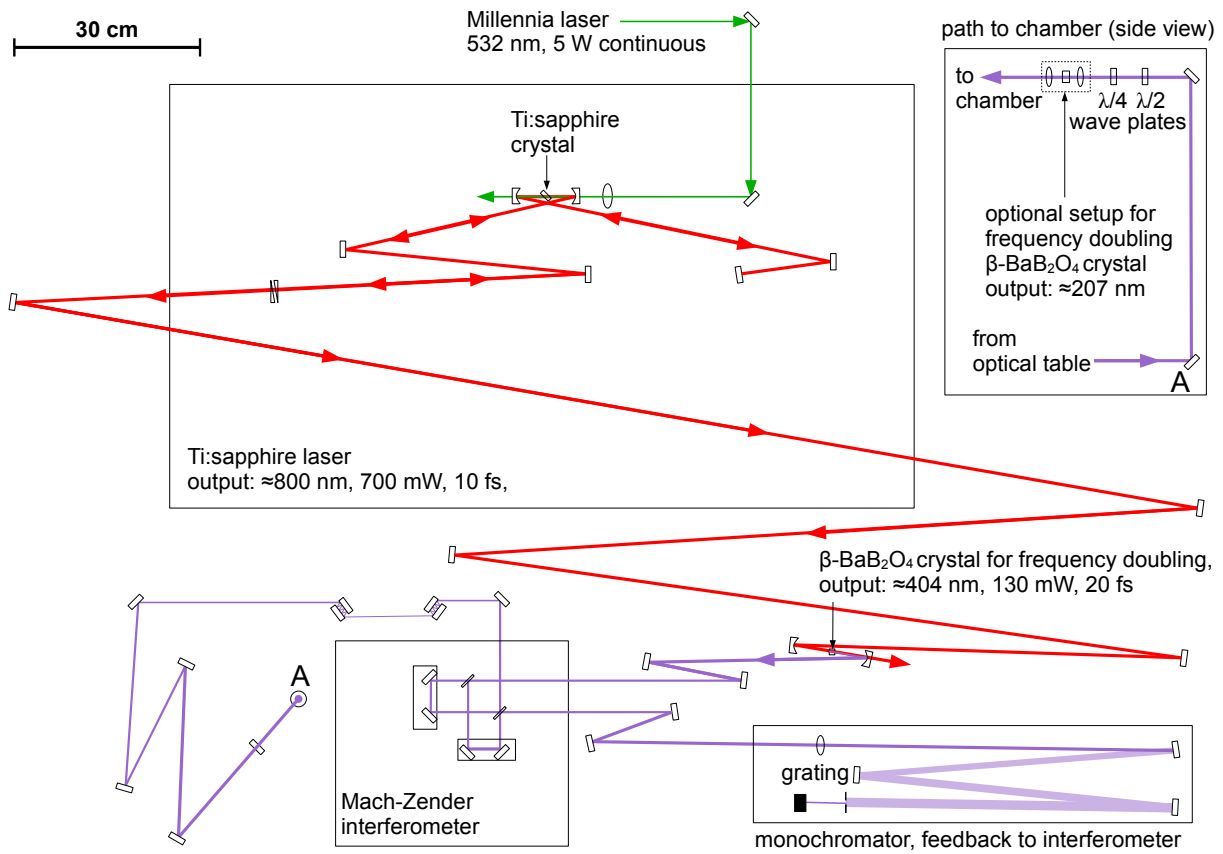


Figure 3.1: Top view drawing of the optical setup designed by Nývlt and Petek. For clarity, the optical elements are not shown with their true scale. The inset in the up-right corner shows the side view of erect optical path into the chamber after mirror A.

3.2 Angle-resolved photoemission

The geometry of the experiments is shown in Fig. 3.2. The polarization of the incident light can be selected to be circular or linear, with the latter at an angle α with respect to the optical plane. The adjustment of the polarization is done by the wave plates in the optical setup as shown in the inset of Fig. 3.1. The optical plane is defined by the incident direction and the sample surface normal.

Except when mentioned otherwise, the photoelectrons were collected in the normal direction of the surface at 300 K in the measurements. In an angle-dependent measurement, the sample can be rotated and the detected photoelectrons have non-zero momentum parallel to the surface. The photoelectrons were analyzed energy resolved by a commercial electrostatic cylindrical sector analyzer (CSA 300, Focus GmbH). The energy resolution was about 50 meV for the pass energy 2 eV and 100 meV for the pass energy 4 eV, as estimated from the vacuum cutoff of the photoemission spectra. The former setting was used for spin-integrated measurements and the latter was used for magnetic dichroism as well as spin-resolved measurements. Previous angle-dependent measurements on Cu(001), Cu(111) and Ag(111) give an estimation of the angular resolution better than 2° . The sample was biased by -1 V during the measurements in order to have higher transmission through the energy analyzer and to better observe the vacuum cutoff in the photoemission spectra. The resultant electric field distribution degraded slightly the angular resolution [140].

The [110] crystalline direction of Co/Cu(001) was aligned with the optical plane. The cobalt films were magnetized in the optical plane along [110] by a pulse current through a copper coil near the sample. The sensitivity direction of the spin-detector, as determined by the magnetization of the O/Fe/W(001) film (see sec. 3.3), was aligned parallel to the sample magnetization in the optical plane, detecting the component of spin-polarization of the photoelectrons along the direction of sample magnetization.

3.3 Spin-polarization analysis

In our measurement, an electron scattering process is used to measure the spin-polarization of photoelectrons. The spin dependence in scattering processes generally comes from two mechanisms. The first one is the coupling between the electron spin and its motion (spin-orbit coupling). For this type of experiments, one requires a sizable electric field in the scatter target and a high incident velocity of electron, which are combined into sizable effective magnetic field in the rest frame of the electron that couples the electron spin [79, 141]. The electron spin-detectors built according to this principle are the various types of Mott-detectors operating at incident electron kinetic energies around 100 keV [141, 142]. Alternative spin-polarimeters are based on the electron diffraction where the ionic potential of heavy atoms contributes significant spin-orbit interaction for electrons even with kinetic energy in the range of 100 eV. This underlies the princi-

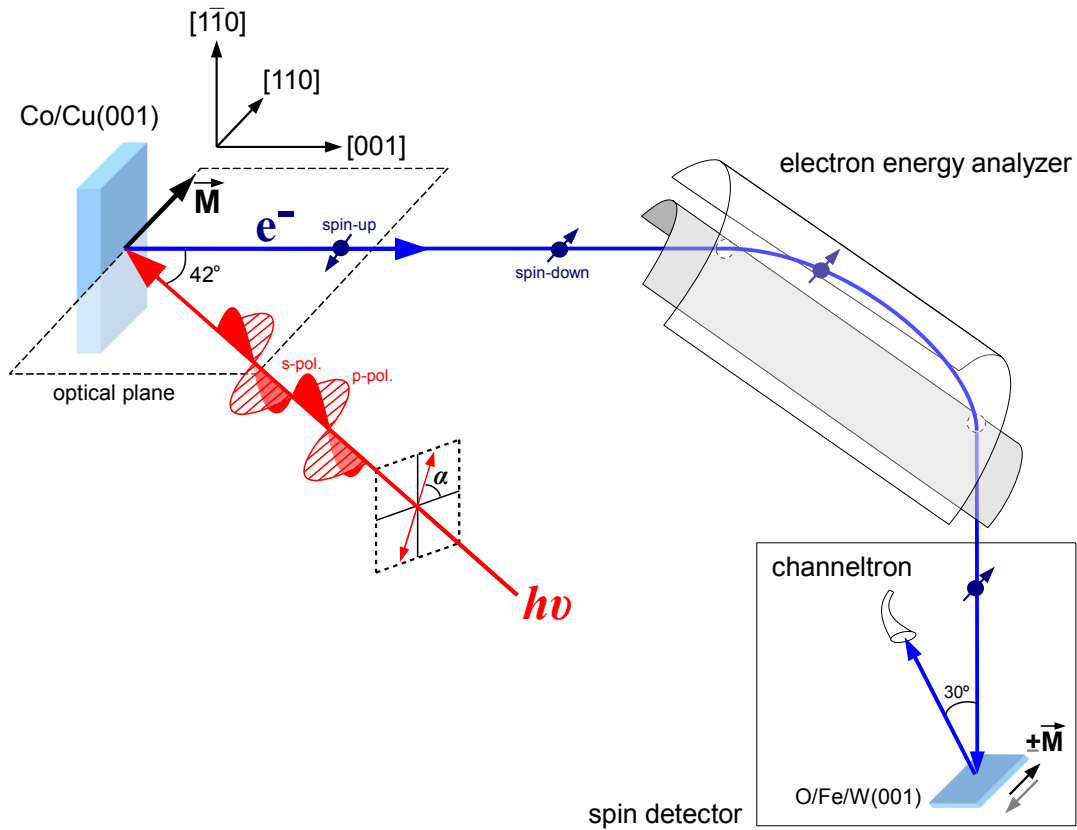


Figure 3.2: Geometry for spin-resolved photoemission measurements. The [110] crystalline direction of Co/Cu(001), as well as the sensitivity direction of spin-detector are aligned with the optical plane. The magnetization is aligned to [110] here which will be labeled as $+M$ later. The incident polarization of light can be controlled as a superposition of p - and s -polarization, which leads to linear polarization with angle α to the optical plane or left/right circular polarization.

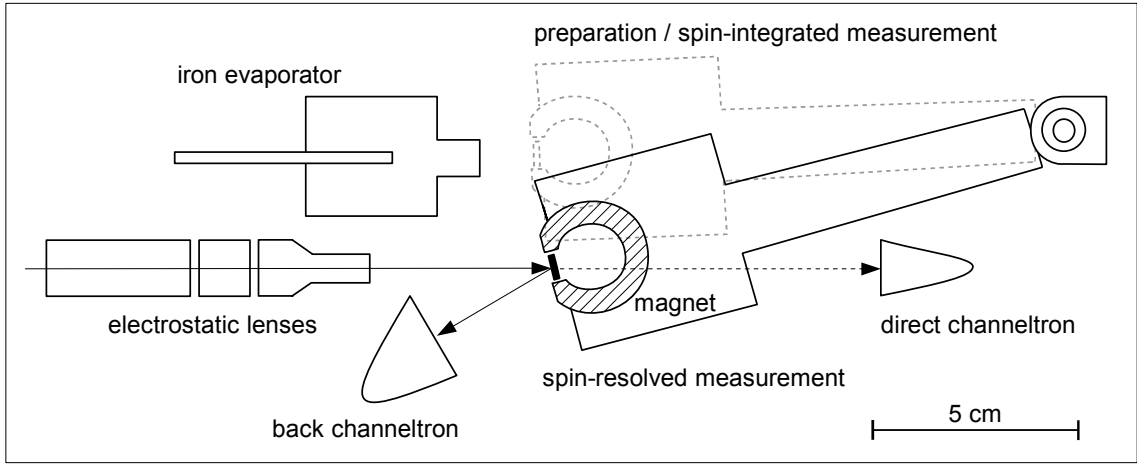


Figure 3.3: Simplified drawing of the spin detector designed by Hartung, Engelhard and Kirschner [152]. The arrows indicate the incident electron beam, which in the case of a spin-integrated measurement (dashed) goes into the direct channeltron and in a spin-resolved measurement (solid) is reflected to the back channeltron from the W(001) crystal covered by an oxygen adsorbed iron film (filled rectangular). The faint dashed parts mark the position for preparation of the iron film on W(001) as well as for the spin-integrated measurement.

ple of spin-polarized low-energy electron diffraction (SPLEED) [143] and the SPLEED spin-polarization analyzer [144, 145].

A second mechanism for spin dependent scattering is the exchange interaction in a ferromagnetic target. Pronounced effects were found, for example, at the energies between majority and minority band edges where one of the electron spin is more strongly reflected compared to the other spin channel [146–148]. More specifically, the surface of Fe(001) covered with oxygen is an ideal candidate for the spin-detector because of its enhanced exchange splitting near the band edge as well as its resistance against residual gas adsorption [149]. Based on these properties several spin-detectors have been built [150–152]. The basic setup of our spin detector is shown in Fig. 3.3, consisting of two channeltrons. One of them is responsible for a spin-integrated measurement and faces directly to the incoming electron beam (direct channeltron). The other (back) channeltron is responsible for the spin-resolved measurement, detecting the reflected specular electron beam from a ferromagnetic, oxygen covered iron film about 10 nm thick on W(001). The iron film is surrounded by an electromagnet which switches the direction of the film magnetization, and it can be moved out of the incident electron beam for the spin-integrated measurement. In our setup the angle of incidence is 15° with respect to the surface normal of the iron film [152].

To measure the number of spin-up and spin-down electrons in the incoming photoelectrons (I_0), the number of reflected electrons from the iron film are measured for two opposite directions of the magnetization of the iron film. This gives us two intensities $I_{\pm M}$. From this we derive the intensity asymmetry A as $A = (I_{+M} - I_{-M}) / (I_{+M} + I_{-M})$. This quantity is proportional to the spin-polarization of the incident electron beam P

along $+M$ by $P = A/S$. The proportional constant S (in analogy to the Sherman function of Mott detectors) depends strongly on the incident electron kinetic energy and was characterized by using a known spin-polarized electron beam. The value of S corresponds to the reflected intensity asymmetry (A) upon magnetization reversal of the iron film when a completely spin-polarized electron beam is analyzed ($P = 1$). In our measurements, the optimal condition of scattering is set at a maximum relative figure of merit $F = S^2 \times (I_{+M} + I_{-M})/I_0$ which is inversely proportional to the required measurement time for a given statistical error of spin-polarization [79]. The obtained S is 0.24 ± 0.03 , as calibrated with secondary electrons from cobalt and iron films [152]. In short, the projection of spin-polarization (P) of the electron beam along the magnetization direction of the iron film (along $+M$) is obtained by:

$$P = \frac{1}{S} \frac{I_{+M} - I_{-M}}{I_{+M} + I_{-M}}. \quad (3.1)$$

The spin-up and spin-down intensities ($I_{\pm s}$) are derived from the total number of measured electrons and the spin-polarization as [79]:

$$I_{\pm s} = \frac{(1 \pm P)}{2} (I_{+M} + I_{-M}). \quad (3.2)$$

In experiments, the magnetization of the iron film inside the spin-detector is sequentially switched between $\pm M$ so that intensities $I_{\pm M}$ can be accumulated independently with small time delay, reducing the extrinsic error due to intensity fluctuation of the laser or sample degradation. The experimental error is obtained by taking into account the statistical error of counting electrons, which is the standard deviation in Poisson statistics and is the square root of the measured number of electrons [79]. The error indicated in the spin-polarization as well as in the partial spectra are derived by error propagation.

For the geometry in Fig. 3.2, we analyze the photoelectron spin in the direction along the sample magnetization. The spin-up (-down) photoelectrons are defined to have their spin with component $-\hbar/2$ ($+\hbar/2$) along the quantization direction parallel to sample magnetization. They correspond to m_s in atomic physics and are labeled in this work as $\pm s$. The electrons in the sample are called majority (minority) electrons if they have spin component $-\hbar/2$ ($+\hbar/2$) projected along the sample magnetization. In our definition, the spin-up photoelectrons have the same $-\hbar/2$ projection of electron spin as the majority electrons. In our experiment, the projection of spin-polarization of photoelectrons along [110] is analyzed and it is equal to the intensity asymmetry between spin-up photoelectrons and spin-down photoelectrons according to Eq. 2.8.

3.4 Sample preparation

The Cu(001) substrate was cleaned by cycles of 2 keV Ar ion sputtering, with a sample current of around $3 \mu A$ and an estimated scanning range of 2 cm^2 . The cleanness of

sample was checked by the Auger electron spectroscopy of copper. After the sputtering, the copper substrate was annealed up to 900 K in order to recover a smooth surface morphology. The resultant surface quality was confirmed by sharp low-energy-electron-diffraction (LEED) spots and photoemission signal through the image potential state [35, 153]. The cobalt films were deposited on the prepared Cu(001) single crystal by an electron beam evaporator (EFM 3, Omicron) from a cobalt rod of 99.995% purity. The thickness of the cobalt films was estimated by the periodic intensity oscillations in medium-energy-electron-diffraction (MEED), as well as confirmed by the onset of magnetic signal in the surface second harmonic generation (SSHG) at around 1.8 ML at 300 K. The SSHG signal was measured in the reflection geometry by using prism pairs to select the ≈ 200 nm component of light [139]. The intensity change of SSHG signal upon sample magnetization reversal was observed when circularly incident light was used [154]. The estimated cobalt film thickness was also cross-checked by Auger electron spectroscopy, which shows no noticeable copper LMM Auger signal at around 15 ML of cobalt.

Chapter 4

Results

In this chapter the experimental results are presented. Ultrathin cobalt thin films of several atomic layer thickness were investigated by photoemission spectroscopy. We observed photoemission intensity changes upon sample magnetization reversal, indicating the magnetic dichroism. The spin-analysis of photoelectrons allows us to identify the relevant spin-polarized electronic states in the photoemission processes.

4.1 Film growth monitored by photoemission

We measured the thickness dependent photoemission spectra in normal-emission geometry using p -polarized light simultaneously with the cobalt film growth (experimental setup: Fig. 3.2). The spectra are displayed in Fig. 4.1a as a function of cobalt film thickness for a photon energy of 3.1 eV and in Fig. 4.1b for a photon energy 6.0 eV.

In Fig. 4.1a we can see three dominant features. The first is located at the energy around 7.0 to 7.4 eV above the Fermi level. This corresponds to the resonant three-photon photoemission (3PPE) from the Cu d -bands through the unoccupied image potential state [63, 155], as can be seen here by the high intensity before cobalt is deposited. The second feature is located at around 6.0 eV, nearby the feature at 6.2 eV due to the two-photon photoemission (2PPE) from the Fermi edge, whose energy remains fixed and the intensity increases gradually until 10 to 12 ML. This is attributed to the higher density of states in the cobalt d -bands near the Fermi level, as compared to the lower density of states in the copper sp -band near the Fermi level. The third feature is the dispersive intensity which starts from 4.8 eV at 4 ML and goes towards higher energy, remains clearly visible until 5.6 eV at 9 ML before it merges into the cobalt d -band feature. As will be characterized in detail in section 5.1, this feature is a result of the unoccupied quantum well states in the cobalt films. Its unoccupied nature can be proved by a comparison with the one-photon photoemission data as follows.

Comparing the one-photon photoemission data in Fig. 4.1b to the two-photon photoemission data in Fig. 4.1a within the energy range from 4.5 eV to 6.2 eV (dashed rectangle), the increasing photoemission intensity from just below the Fermi level is present again,

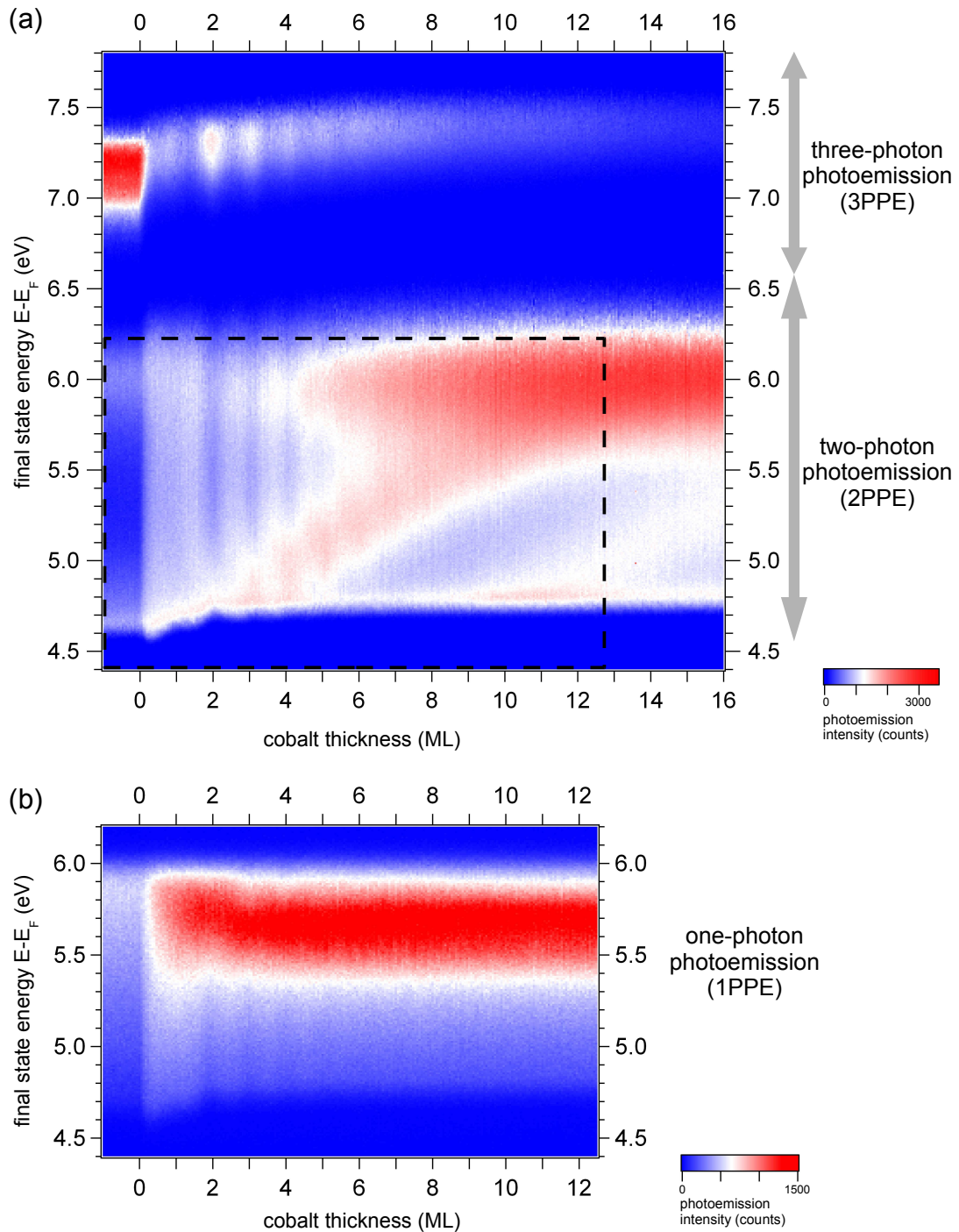


Figure 4.1: (a) Thickness dependent two- and three-photon photoemission (2PPE and 3PPE) spectra ($h\nu=3.1$ eV) measured in normal emission during the deposition of several monolayers (ML) of cobalt film on Cu(001). (b) Experiment as in (a) but with one-photon photoemission (1PPE, $h\nu=6.0$ eV). The excitation light is p -polarized in both cases. The dashed-rectangle indicates the comparable region of 2PPE to 1PPE.

centered at around 5.8 eV. However, the strongly dispersive feature is missing. If the dispersive feature in two-photon photoemission spectra comes from the initial state below the Fermi level, it should also be present in the one-photon photoemission spectra under the chosen condition. Its absence in Fig. 4.1b therefore indicates its origin in the unoccupied states. The states themselves are detected in a two-photon photoemission process as intermediate states in the transition, and they do not participate the one-photon photoemission process. This conclusion agrees with observations by inverse photoemission experiments [135, 136], as well as the recent theoretical calculations [47].

In addition, we clearly observe an intensity oscillation over all the observed energy range with monolayer cobalt thickness period up to 5 ML in two- and three-photon photoemission. The overall intensity oscillation is weaker in one-photon photoemission, but still visible. The intensity oscillation in the one- and two-photon photoemission energy range (4.5 eV to 6.2 eV) has lower intensity at integer thickness than that at the nominal half-integer thickness, whereas the three-photon photoemission intensity (around 7.2 eV) has the opposite behavior. We ascribe these out-of-phase monolayer oscillations to the enhanced photoemission intensity due to scattering at defects [35, 156, 157]. This will be further discussed in section 5.5.

4.2 Magnetic dichroism in photoemission

In the upper panels of Fig. 4.2a and Fig. 4.2b the two-photon photoemission spectra measured in normal emission geometry are shown for two magnetization directions along $[110]$ and $[\bar{1}\bar{1}0]$ ($\pm M$). The normalized intensity asymmetry under magnetization reversal A (Eq. 2.3) is displayed in the lower panels. Photoemission through the quantum well state and from the Fermi level are indicated by $E_{QW} + h\nu$ and $E_F + 2h\nu$ respectively.

The 2PPE spectra observed using circularly polarized light are shown in the upper panel of Fig. 4.2a, and the derived A_{MCD} curves for right- as well as for left-circularly polarized light ($\mp\sigma$) are shown in the lower panel. The A_{MCD} signal is about 5% for two-photon photoemission from near the Fermi level, comparable to the previous observations with conventional one-photon photoemission from Schneider *et al.* [22] and Nakagawa *et al.* [158]. More importantly, a signal of about 3% is observed at the position of the unoccupied QW state ($E_{QW} + h\nu$). In the case of circular dichroism, reversal of the light helicity combined with a reversal of the sample magnetization should not change the photoemission intensity in our setup (Fig. 3.2) [21, 65]. The average of A_{MCD} from $-\sigma$ and $+\sigma$ light, shown in the lower panel (gray diamonds), would thus give zero in the ideal case. We ascribe the remaining experimental average of below 1% to the apparatus asymmetry.

For the case of linearly polarized light in Fig. 4.2b, we cannot observe any dichroic asymmetry within our detection limit for nominally p - and s -polarized light. The magnetic dichroism only appears for a tilted polarization plane: $\alpha \neq 0^\circ, \pm 90^\circ, 180^\circ$, in agreement

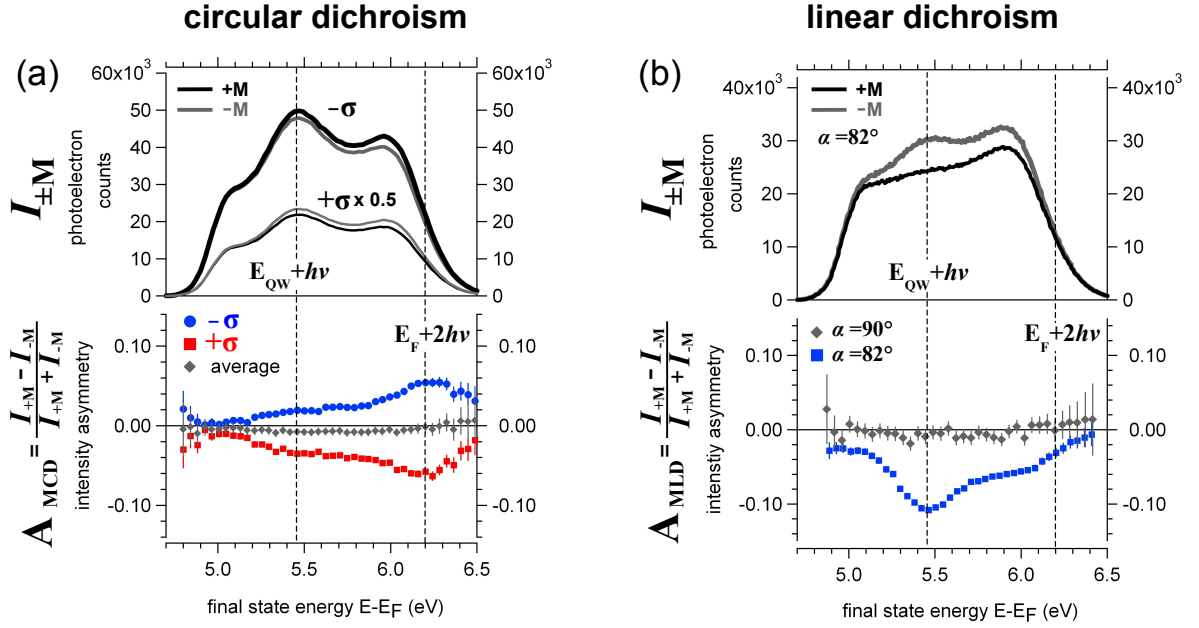


Figure 4.2: The magnetic (a) circular and (b) linear dichroism observed in two-photon photoemission from about 7 ML Co/Cu(001) in normal emission geometry. The linear polarization denoted by the angle α is defined as the deviation from p -polarization, as shown in Fig. 3.2. (a) upper panel: 2PPE spectra measured for opposite sample magnetizations $\pm M$ using right- ($-\sigma$) and left-circularly polarized light ($+\sigma$); lower panel: dichroic asymmetry A_{MCD} for $-\sigma$ (blue circles) and $+\sigma$ (red squares), and their average (gray diamonds). (b) upper panel: 2PPE spectra measured for $\pm M$ using linearly polarized light at $\alpha = 82^\circ$; lower panel: dichroic asymmetry A_{MLD} for s -polarized light ($\alpha = 90^\circ$, gray diamonds) and for $\alpha = 82^\circ$ (blue squares).

with symmetry requirements [21]. When we choose $\alpha = 82^\circ$, we observe a change in the photoemission spectra when we switch the sample magnetization, as shown in upper the panel of Fig. 4.2b. The derived dichroic asymmetry A_{MLD} is around 10% at the quantum well state peak ($E_{QW} + h\nu$) and 4% from the Fermi level ($E_F + 2h\nu$) as shown in the lower panel.

The magnetic dichroic signal at $E_{QW} + h\nu$ is special, since it may signal spin-orbit coupling in the unoccupied state if the dichroic signal would indeed come from the unoccupied quantum well state. As we always detect photoelectrons at the final state energy $E_{QW} + h\nu$, contributions from the spin-orbit coupling at the final state itself as well as from the initial states at energy $E_{QW} - h\nu$ is also present. To elucidate the origin of the dichroic signal at $E_{QW} + h\nu$ further, we investigated the influence of quantum well states at different cobalt thickness to the magnetic dichroism. The photoemission spectra from the 9 ML and 12 ML films are shown in Fig. 4.3a and b. The upper panels for circular dichroism and the middle panels are for linear dichroism. For the 9 ML film, the quantum well state is located at a higher energy of 5.7 eV compared to 5.45 eV on the 7 ML film. For the 12 ML film, the quantum well state feature overlaps with the initial d -band feature at around 6.0 eV. As marked by the dashed lines, there is an obvious intensity change in photoemission through the quantum well states for both film thicknesses, either with circularly or linearly polarized light. The derived dichroic signals are displayed in the lower panels. By this systematic cobalt thickness variation, we observe a roughly constant 10% magnetic linear dichroic signal associated with the quantum well states from 7 ML to 12 ML, as well as a small about 3% circularly dichroic signal overlapping with 5% signal from the Fermi level. The coincidence of the dichroic signal with the photoemission feature of the quantum well states at several different cobalt thicknesses points to the quantum well states themselves as the source of magnetic dichroism, and is therefore an indication of the spin-orbit coupling in the unoccupied quantum well states. This will be discussed in section 5.1.2. A measurement of magnetic circular dichroism during the growth of cobalt films is shown in Fig. 4.4. The contribution from the quantum well states in the photoemission intensity as well as in the dichroic signal are indicated by the arrows. The onset of magnetic dichroism is observed around 3 ML at energy 5.8 eV and 6.1 eV (near 2PPE from the Fermi level), closely related to the fact that the Curie temperature of Co/Cu(001) rises to 300 K at around 2 ML [125].

The photoemission intensity as a function of the incident linear polarization of light is shown in Fig. 4.5. In Fig. 4.5a, the two-photon photoemission intensities at the quantum well state feature for the 7 ML cobalt film, with magnetization $\pm M$, are displayed as functions of the angle α in Fig. 3.2. The intensities $I_{\pm M}$ can be fitted by a model $I_{\pm M}(\alpha) = I_s + I_p \cos^2(\alpha \pm \Delta\alpha/2)$ with $\Delta\alpha = 5^\circ$ (solid curves), with I_s and I_p labeled in Fig. 4.5a. In Fig. 4.5b we derive the dichroism from the intensity asymmetry upon magnetization reversal. The dichroic signal is zero when we use incident s -polarized light ($\alpha = \pm 90^\circ$) and p -polarized light ($\alpha = 0^\circ$) (discussed in section 5.2).

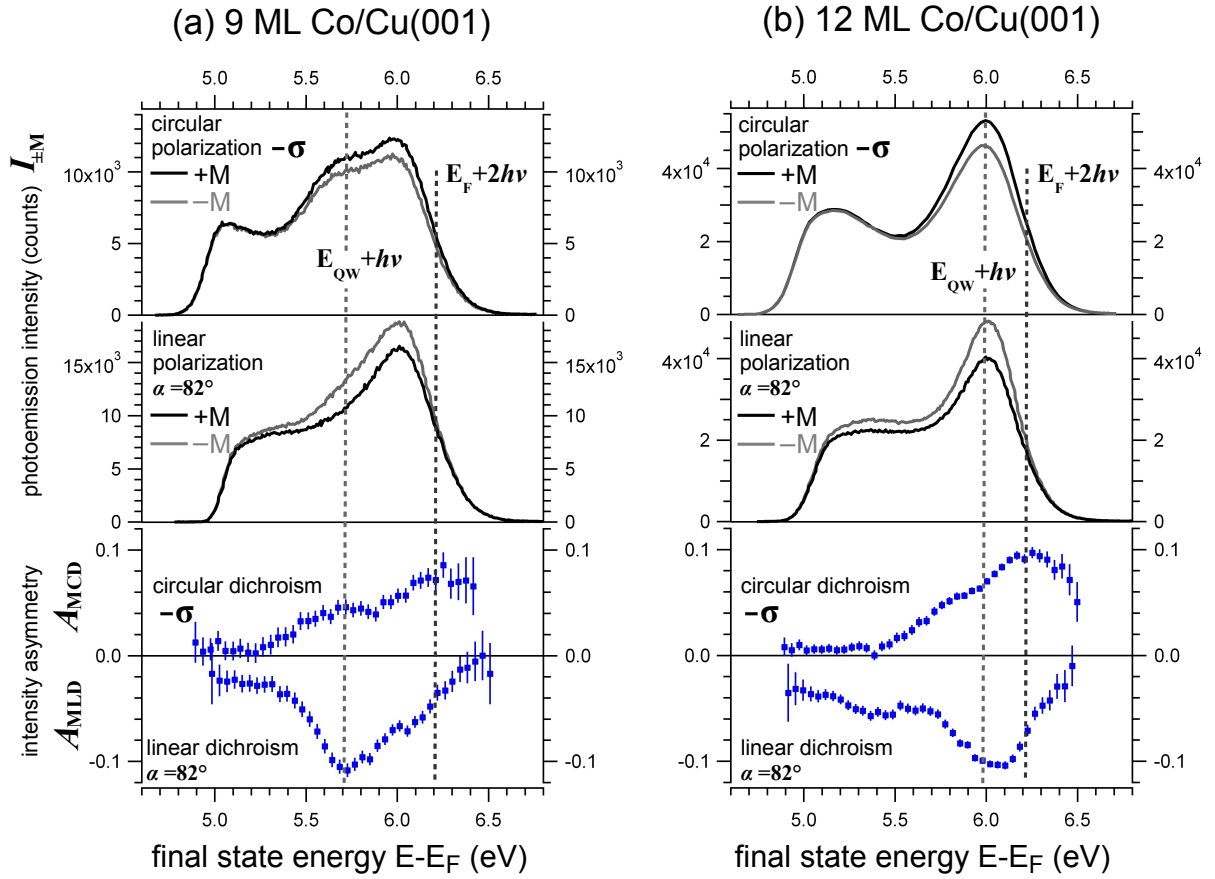


Figure 4.3: The magnetic dichroism in photoemission from (a) 9 ML and (b) 12 ML cobalt films. The spectra obtained with circularly and linearly polarized light are displayed in the upper and middle panels respectively. The dichroic signals are derived in the lower panels. The dashed lines mark the final state energy of photoemission processes through the quantum well state ($E_{QW} + h\nu$) and from the Fermi level ($E_F + 2h\nu$). The photon energy $h\nu$ is 3.1 eV.

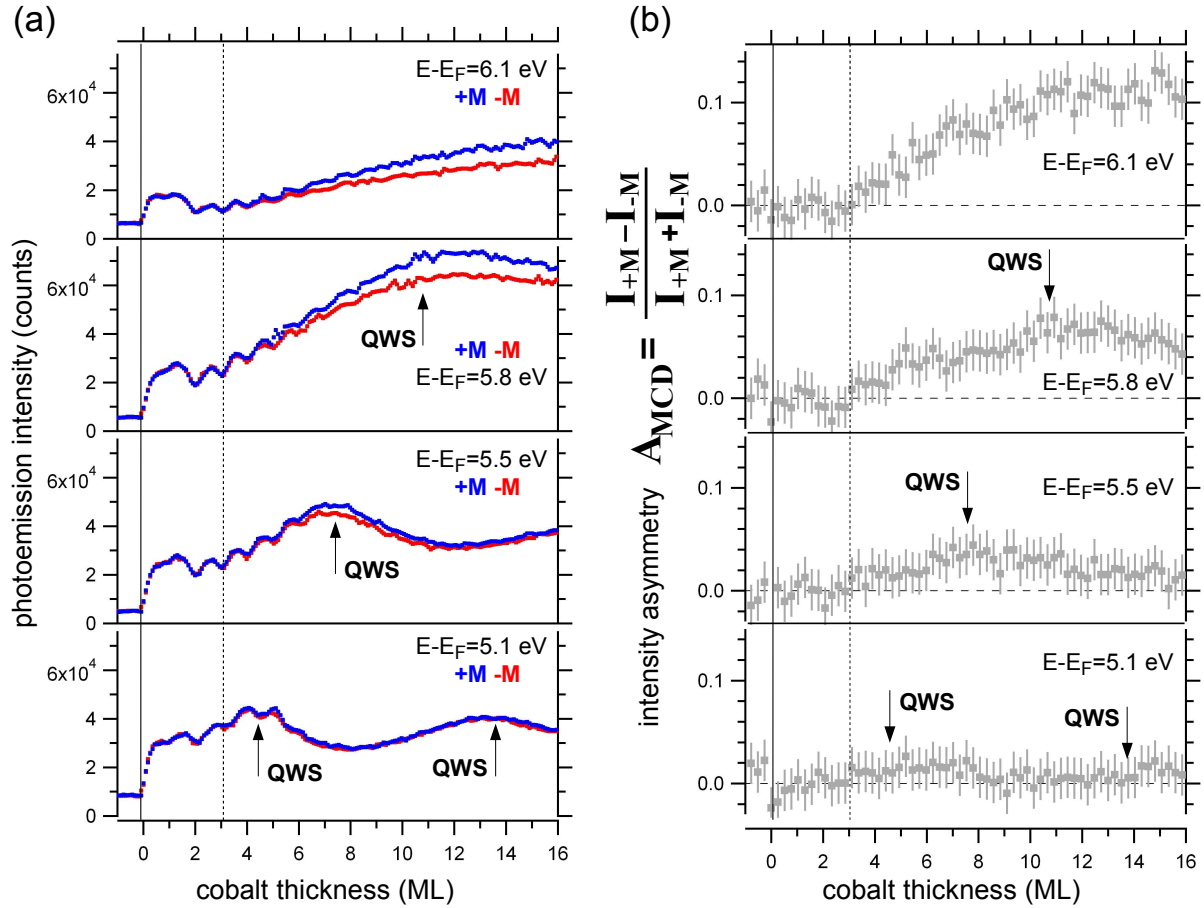


Figure 4.4: (a) Magnetization dependent two-photon photoemission intensities and (b) the derived magnetic circular dichroic signal as functions of cobalt thickness. The final state energies are referred to the Fermi level. The incident light is right-circularly-polarized and the photon energy is 3.1 eV. The vertical dashed lines indicate the onset of the dichroic signal for $E - E_F = 6.1$ eV at 3 ML. The arrows indicate the feature of quantum well states (QWS) which coincides to the slightly enhanced dichroic signal.

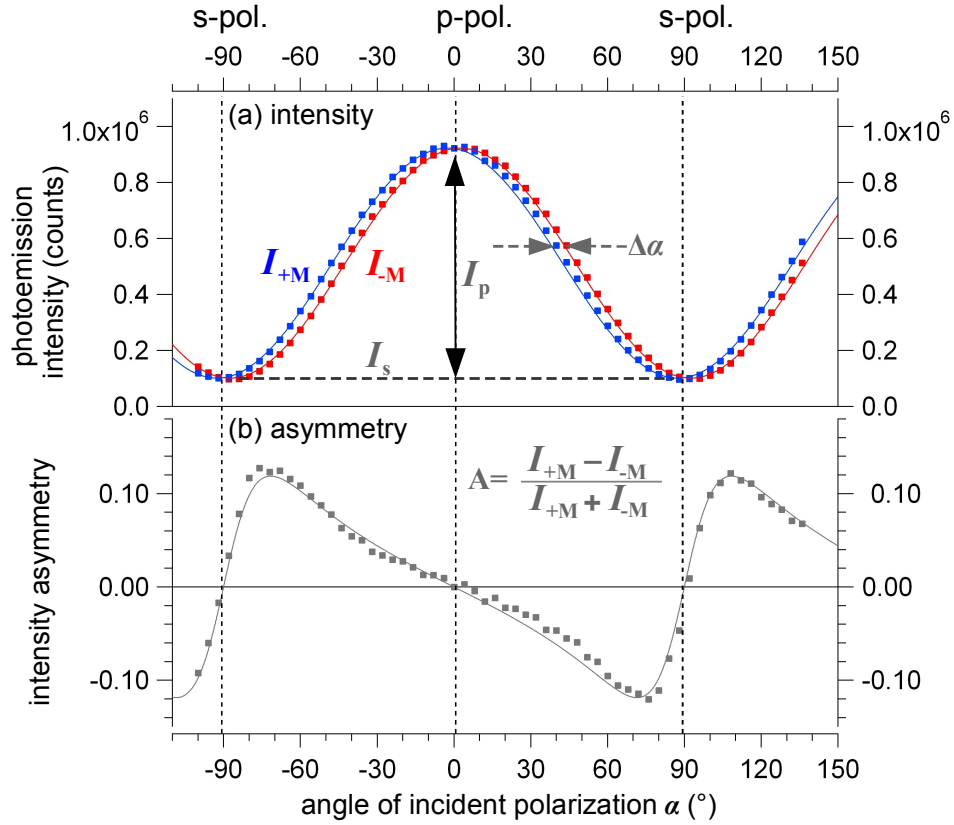


Figure 4.5: Magnetic linear dichroism in 2PPE through the quantum well state in 7 ML Co/Cu(001), measured at a final state energy $E_F + 5.45$ eV. The tilt angle α of the electric field vector of the incident light is defined in Fig. 3.2. (a) Photoemission intensities $I_{\pm M}$ for opposite magnetization directions $\pm M$. (b) Intensity asymmetry derived from the intensities in (a). The photon energy $h\nu$ is 3.1 eV. The solid curves are from the model described in the text. This data and the model will be discussed in section 5.2

4.3 Spin-resolved measurements

In this section, the spin-polarization of photoelectrons from Co/Cu(001) is analyzed. The role of the unoccupied quantum well states is investigated by cobalt thickness dependent measurements and by examining the spin-polarization with variable linear polarization of light. Moreover, the comparison between spin-resolved one- and two-photon photoemission reveals the different spin character of the electronic states involved in these photoemission processes.

4.3.1 Films grown at 310 K

We analyzed the spin-polarization of photoelectrons emitted from cobalt films in the thickness range from 3 to 14 ML. The spin-resolved two-photon photoemission (2PPE) spectra and spin-polarization are shown in the left and right panels of Fig. 4.6, for (a) p -polarized and (b) s -polarized incident light.

For all 2PPE spectra we can find characteristic cutoffs at 6.2 eV (Fermi level) and at around 4.7 to 4.8 eV (work function). The spin-polarization for the p - and s -polarized cases shows a weak variation from the low energy cutoff up to about 6.0 eV and then drops at around 6.2 eV. This general trend in spin-polarization can be expected from the cobalt electronic structure: the majority d -band gives rise to the positive spin-polarization up to near the Fermi level, where the minority d - and sp - bands start to contribute and therefore reduce the spin-polarization (see band structure in Fig. 2.2). Within our thickness range, we observe an increasing spin-polarization for the full energy range as the cobalt thickness increases. This can be attributed to the influence of a finite electron mean free path, which decreases the number of unpolarized photoelectrons coming from the copper substrate with increased cobalt film thickness (see section 5.6).

In the 2PPE spectra obtained with p -polarized light, after 4 ML we observe clear features due to the enhanced photoemission intensity through the unoccupied quantum well states in the cobalt films, as is indicated by the arrows in Fig. 4.6a, left panel. As the thickness increases from 4 to 11 ML, the quantum well state feature disperses upward in energy. The arrows in the right panel indicate the same energies as that in the left panel. For 6 to 11 ML cobalt films, the spin-polarization around the feature of quantum well state is about 10% higher than that of the lower energy side. When the thickness increases further to 14 ML, the second quantum well state appears at about 5.2 eV and one can identify a corresponding enhancement in the spin-polarization as compared to the 11 ML.

With s -polarized light, the intensity of 2PPE through the quantum well states is suppressed as is shown in Fig. 4.6b and comparing with spectra in Fig. 4.6a. This is consistent with the dominant Δ_1 symmetry of the cobalt sp -band, from which the quantum well states are derived, because the selection rules allow only intermediate states with Δ_5 symmetry to be detected in our normal emission geometry using s -polarized light [56, 57].

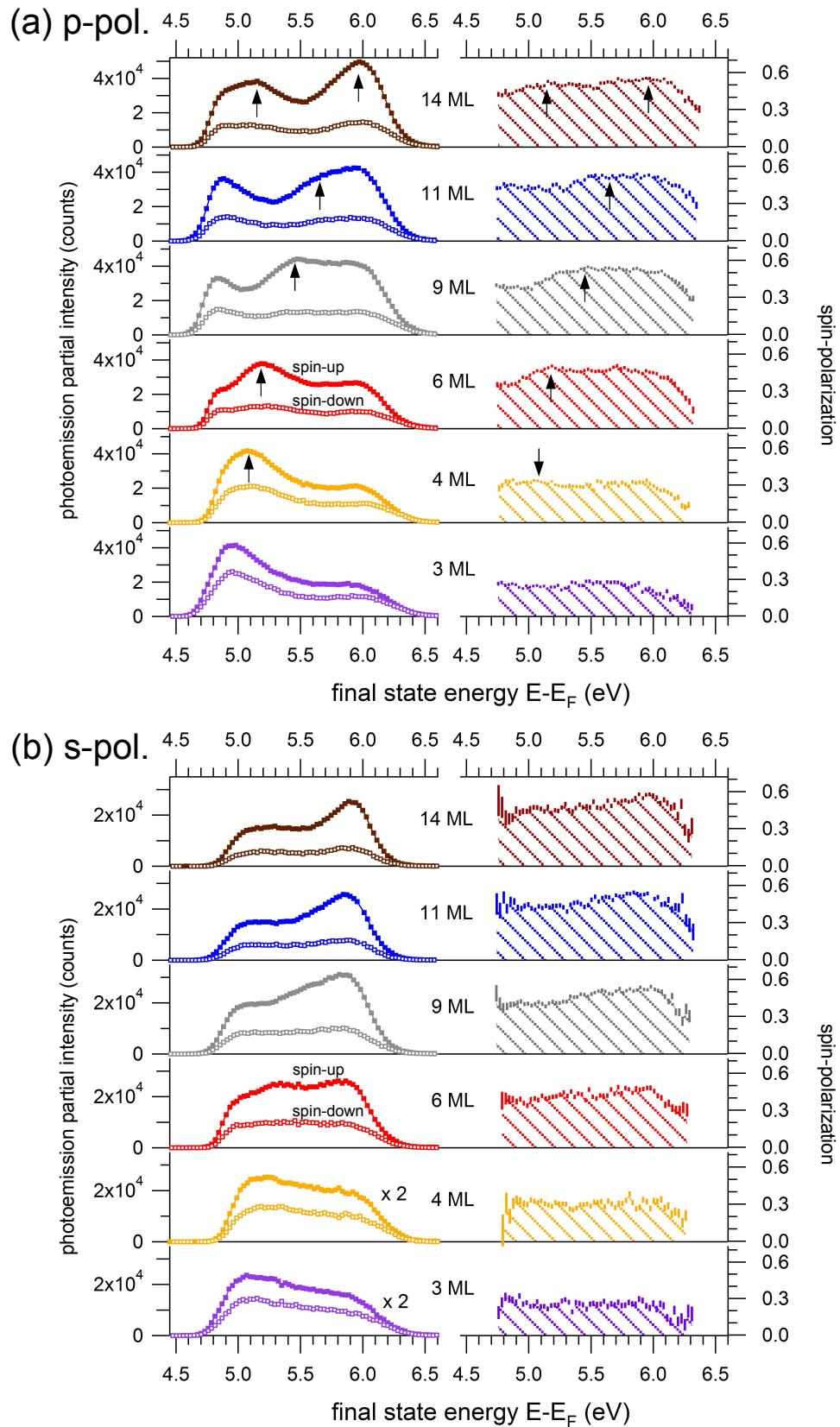


Figure 4.6: Spin-polarized 2PPE spectra measured from different thickness of cobalt films on Cu(001). The photon energy is 3.1 eV. Solid and open symbols represent spin-up and spin-down spectra, respectively. The cobalt films are magnetized along [110] direction (+ M).

In the spin-polarization on the right side, we observe the positive spin-polarization plateau and the drop near the two-photon Fermi edge at 6.2 eV, as found in the p -polarized case in Fig. 4.6a. This general shape of spin-polarization is dominant over our cobalt thickness range whereas the features owing to the quantum well states are apparently suppressed.

The effect of selection rules in photoemission [49, 56, 57] is further studied by tuning the linear polarization of light from p - to s -polarization. This is shown in Fig. 4.7a where the spin-up and spin-down photoemission intensities measured at the quantum well state feature on a 6 ML cobalt film are shown as functions of the linear polarization of light, indicated by the angle α (see Fig. 3.2). The sample is magnetized along the $[\bar{1}\bar{1}0]$ direction ($-M$). Dashed curves are the spin-up and spin-down intensity from a phenomenological model as previously used for magnetic dichroism (section 4.2): $I^{up/down} = I_s^{up/down} + I_p^{up/down} \cos^2(\alpha - \Delta\alpha/2)$, with $I_s^{up/down}$ and $I_p^{up/down}$ indicated in the graph and $\Delta\alpha$ is 4.5° . The spin-polarization is shown in Fig. 4.7b. The *magnitude* of spin-polarization is slightly ($\approx 5\%$) higher in the p -polarized case than the s -polarized case. This is a consequence of a higher spin-down photoelectrons intensity when we used p -polarized light as compared to the case with s -polarized light, *i.e.*, $I_p^{down}/I_p^{up} > I_s^{down}/I_s^{up}$. This slightly higher spin-polarization in photoemission through the quantum well states is also observed in the comparison with the spin-polarization at 0.3 eV lower than the quantum well state feature (black squares in Fig. 4.7). The spin dependence in photoemission through the quantum well states will be discussed in section 5.3.

4.3.2 Films grown at 170 K

Two-photon photoemission (2PPE) spectra were measured from 5 ML cobalt films deposited at 170 K. The spectra were subsequently measured with p -polarized light at various temperatures as shown in Fig. 4.8a. Each measurement took about 2 minutes. The grown film at 170 K has the lowest work function as compared to the values at elevated temperature. This implies a rough surface morphology of the 170 K grown film. This interpretation agrees with the suppressed oscillation in reflection high energy electron diffraction (RHEED) [114] and helium ion reflection [117] during low temperature growth of Co/Cu(001). As the temperature increases, we observe an increasing intensity of 2PPE through the unoccupied quantum well states ($E_{QW} + h\nu$) as well as 3PPE via the image potential state ($E_{IP} + h\nu$). They are summarized in Fig. 4.8b. This enhanced intensity can be attributed to the smoothing of an originally rough surface by thermally activated surface diffusion [114]. Substantial interdiffusion at the buried cobalt-copper interface during our annealing process is unlikely because it will degrade the quantum well states strongly [113, 117, 124, 160], contrary to our increasing intensity at $E_{QW} + h\nu$ up to 370 K. Other photoemission studies also show similar evolution of quantum well states due to annealing [160–162].

The spin-resolved 2PPE spectra from 6 ML cobalt films grown at 170 K are displayed in Fig. 4.9a, in comparison with the spectra from the film grown at 330 K. The feature of

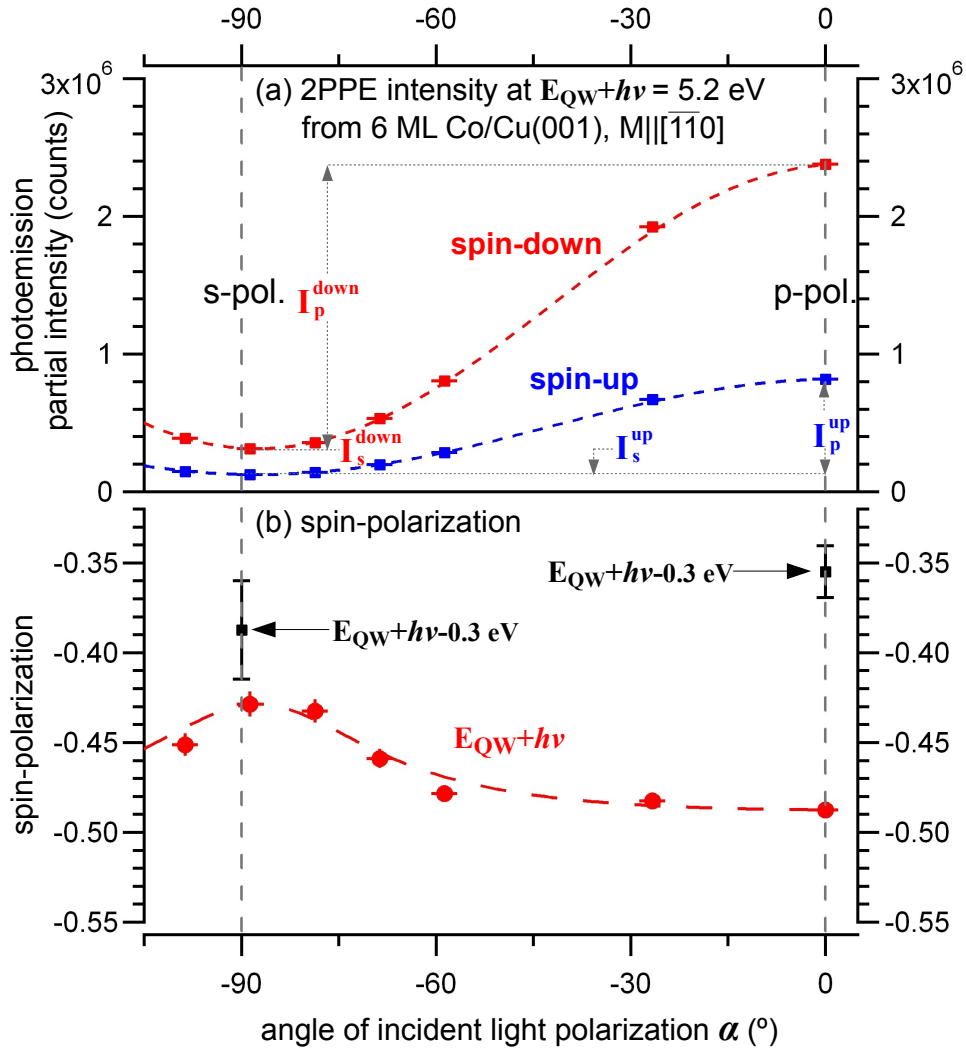


Figure 4.7: The (a) spin-resolved photoemission intensity and (b) spin-polarization measured at the quantum well state feature $E_F + 5.2$ on the 6 ML Co/Cu(001) at $E_{QW} + h\nu$, as a function of the incident light polarization angle α . Photon energy $h\nu$ is 3.1 eV. The sample magnetization is parallel to $[\bar{1}\bar{1}0]$. Dashed curves are the spin-up and spin-down intensities after a phenomenological model (see in text). For comparison, the spin-polarization at $E_{QW} + h\nu - 0.3$ eV is shown as black squares. They are estimated by the data from Fig. 4.6.

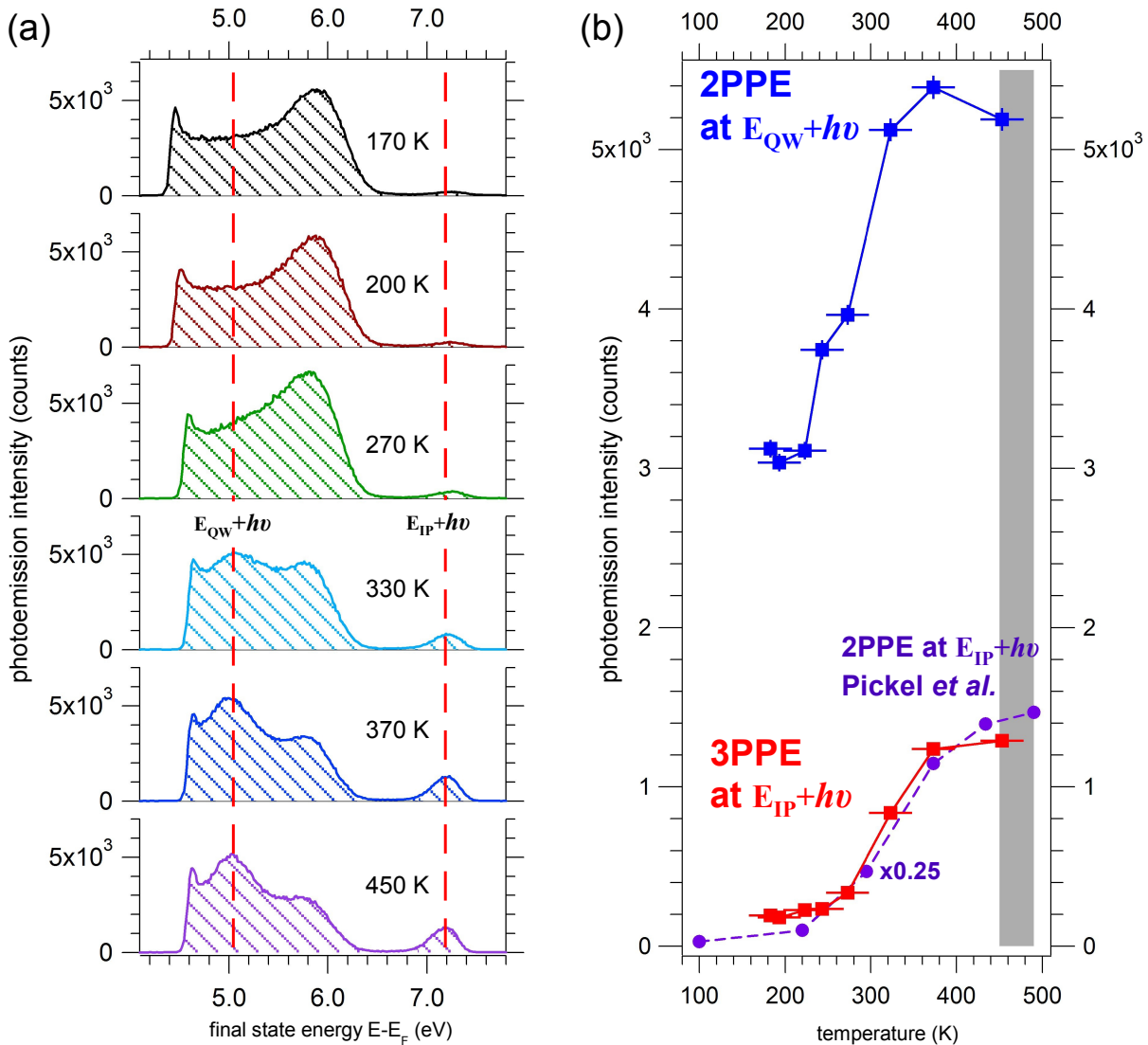


Figure 4.8: (a) Two-photon photoemission (2PPE) spectra taken at different temperatures from the 5 ML cobalt film deposited at 170 K. Photon energy is $h\nu=3.1$ eV and the incident light is p -polarized. The dashed lines mark the features of 2PPE through the quantum well state ($E_{QW} + h\nu$) and three-photon photoemission (3PPE) through the image potential state ($E_{IP} + h\nu$). (b) The 2PPE intensity at $E_{QW} + h\nu$ (blue) and $E_{IP} + h\nu$ (red) as a function of temperature during the measurement. Comparison to 2PPE data by Pickel [159] is shown by circles with dashed line. The gray shaded region indicates the temperature region where diffusion of copper atoms to the surface has been observed [114, 124].

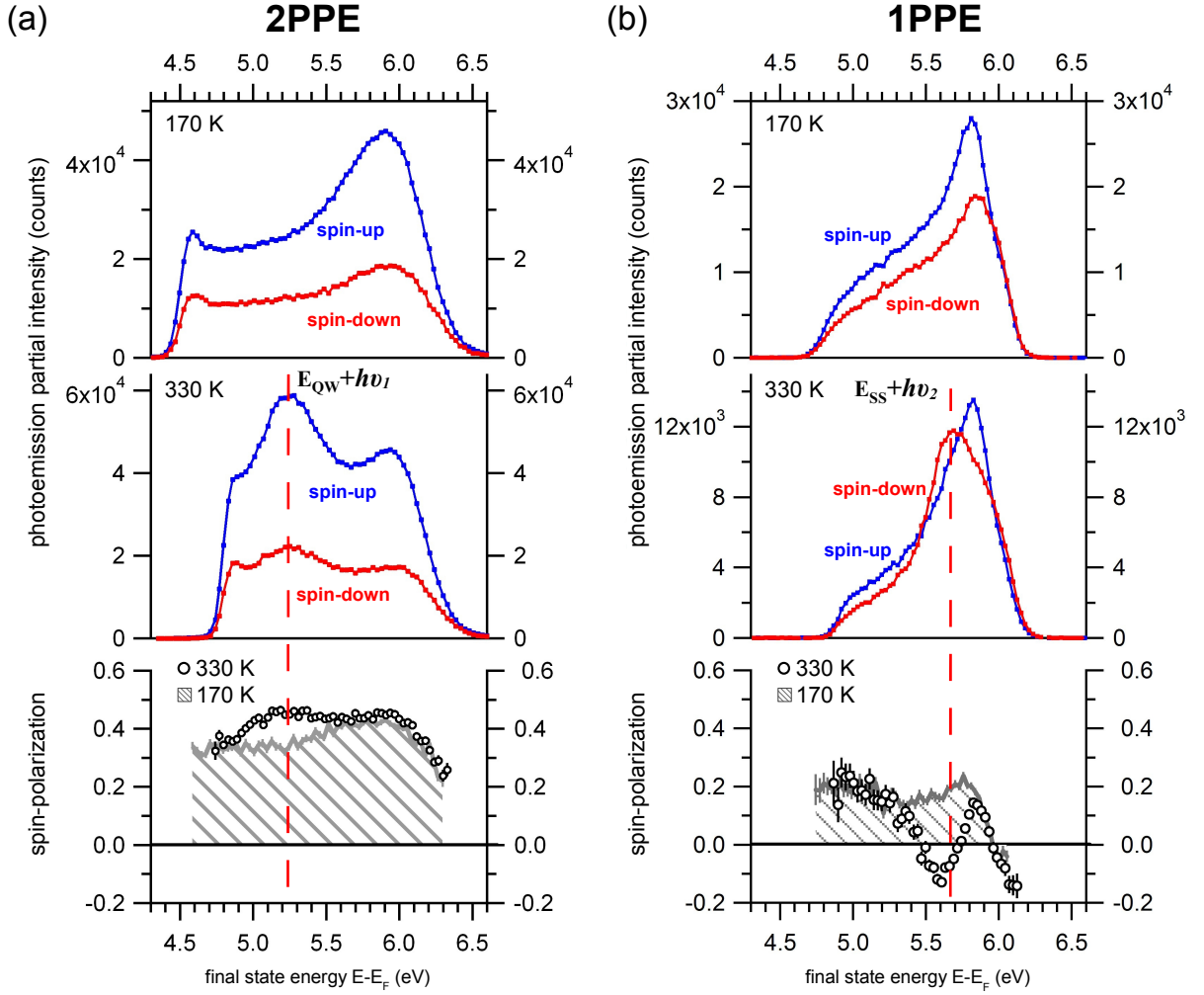


Figure 4.9: Spin-resolved (a) 2PPE and (b) 1PPE spectra from 6 ML cobalt films grown and measured at 170 K (upper panels) and from 6 ML films grown and measured at 330 K (middle panels). The spin-polarization is derived in the lower panels for comparison, in which the largest difference is observed at 2PPE via the quantum well state ($E_{QW} + h\nu_1$). In 1PPE spectra and their spin-polarization, a clear difference due to the minority surface resonance state is observed at $E_{SS} + h\nu_2$. The photon energies used for 2PPE and 1PPE are $h\nu_1 = 3.1$ eV and $h\nu_2 = 6.0$ eV. The light is p -polarized for all the cases.

quantum well state is missing at 5.2 eV for the 170 K grown film (at $E_{QW} + h\nu$), and the spin-polarization is lower by 10% at the same energy. This comparison shows clearly the enhanced spin-polarization at $E_{QW} + h\nu$ when the quantum well state is present. This enhanced spin-polarization at $E_{QW} + h\nu$ due to the quantum well state is consistent with the value derived from the cobalt thickness dependent experiments in section 4.3.1.

In addition, we compare the above 2PPE data with the spin-resolved one-photon photoemission (1PPE) using photon energy $h\nu_2 = 6.0$ eV. The 1PPE spectra are shown in Fig. 4.9b. The major difference between the 170 K grown film (upper panel) and the 330 K grown film (middle panel) is in the spin-down spectrum, whose peak intensity increases noticeably and shifts from 5.85 eV to 5.65 eV ($E_{SS} + h\nu_2$). This leads to a negative spin-polarization near 5.6 eV for the 330 K grown film and is in strong contrast to the overall positive spin-polarization of the 170 K grown film (lower panel). The spin-down feature at

around 5.6 eV coincides with the known energy of the minority occupied surface resonance state on Co/Cu(001) at 0.4 eV below the Fermi level [104, 130]. This is in agreement with our expectation that the surface quality is poor for the low temperature grown films and the surface electronic state is strongly influenced. This comparison between 1PPE and 2PPE will be further discussed in section 5.3.

4.4 Spin-resolved magnetic dichroism

In this section, measurements of magnetic dichroism and spin-resolved photoemission are combined to study the role of the spin-polarized photoelectrons in contributing to the magnetic dichroism. This is done by explicitly analyzing the even and odd components of the spin-polarization upon sample magnetization reversal (section 2.3).

The experiments were performed with circularly polarized light at room temperature. In the measurement we switched the sample magnetization ($\pm M$), the polarization of light ($\pm\sigma$), and the magnetization of the iron film in the spin-detector in sequence so that the eight different photoemission spectra are accumulated independently. After taking into account the finite spin sensitivity of the spin-detector, we obtained the eight spin-resolved partial spectra $I_{\pm s, \pm M}^{\pm\sigma}$, with $\pm s$ denoting the spin-up and spin-down directions parallel to $[\bar{1}10]$ and $[110]$ (Fig. 3.2). The results are displayed in Fig. 4.10a,b for the 7 ML cobalt film and in Fig. 4.11a,b for the 12 ML film.

The magnetic dichroic signal and the photoelectron spin-polarization are derived by relevant combinations of partial intensities. By summing $I_{\pm s, \pm M}^{\pm\sigma}$ over opposite spin directions $\pm s$, we can derive the spin-integrated intensities from which the magnetic dichroic asymmetry $A_{MCD}^{\pm\sigma}$ for each helicity of light is obtained (Eq. 2.3). They are shown in Fig. 4.10c, and Fig. 4.11c. On the other hand, the intensity asymmetry between $I_{\pm s, \pm M}^{\pm\sigma}$ over opposite spin directions gives us the spin-polarization $P_{\pm M}^{\pm\sigma}$ for each sample magnetization and light polarization (Eq. 2.8). They are shown in Fig. 4.10d and Fig. 4.11d. The $P_{\pm M}^{\pm\sigma}$ are similar to previous cases with p -polarized light (Fig. 4.6a) since the circularly polarized light has also the p -polarized component which contributes dominantly the photoemission intensity as compared to the s -polarized component, as shown in Fig. 4.7.

Moreover, the above four different spin-polarization $P_{\pm M}^{\pm\sigma}$ are analyzed into two components, one of them changes its sign as the sample magnetization is reversed, the "exchange spin-polarization" ($P_{ex}^{\pm\sigma}$), and the other one which does not change sign with the sample magnetization, the "spin-orbit spin-polarization" ($P_{so}^{\pm\sigma}$) [93]. They are defined as the odd ($P_{ex}^{\pm\sigma}$) and even ($P_{so}^{\pm\sigma}$) components of the spin-polarization upon sample magnetization reversal (in Eq. 2.9 and Eq. 2.10). They are shown in Fig. 4.10e,f and Fig. 4.11e,f.

As we can clearly see from the magnitude of the exchange spin-polarization $P_{ex}^{\pm\sigma}$ in Fig. 4.10e for 7 ML film, it dominates the measured photoelectron spin-polarization. This reflects the fact that the measured spin-polarization of photoelectrons almost changes its sign completely when the sample magnetization is reversed (Fig. 4.10d). The rest spin-

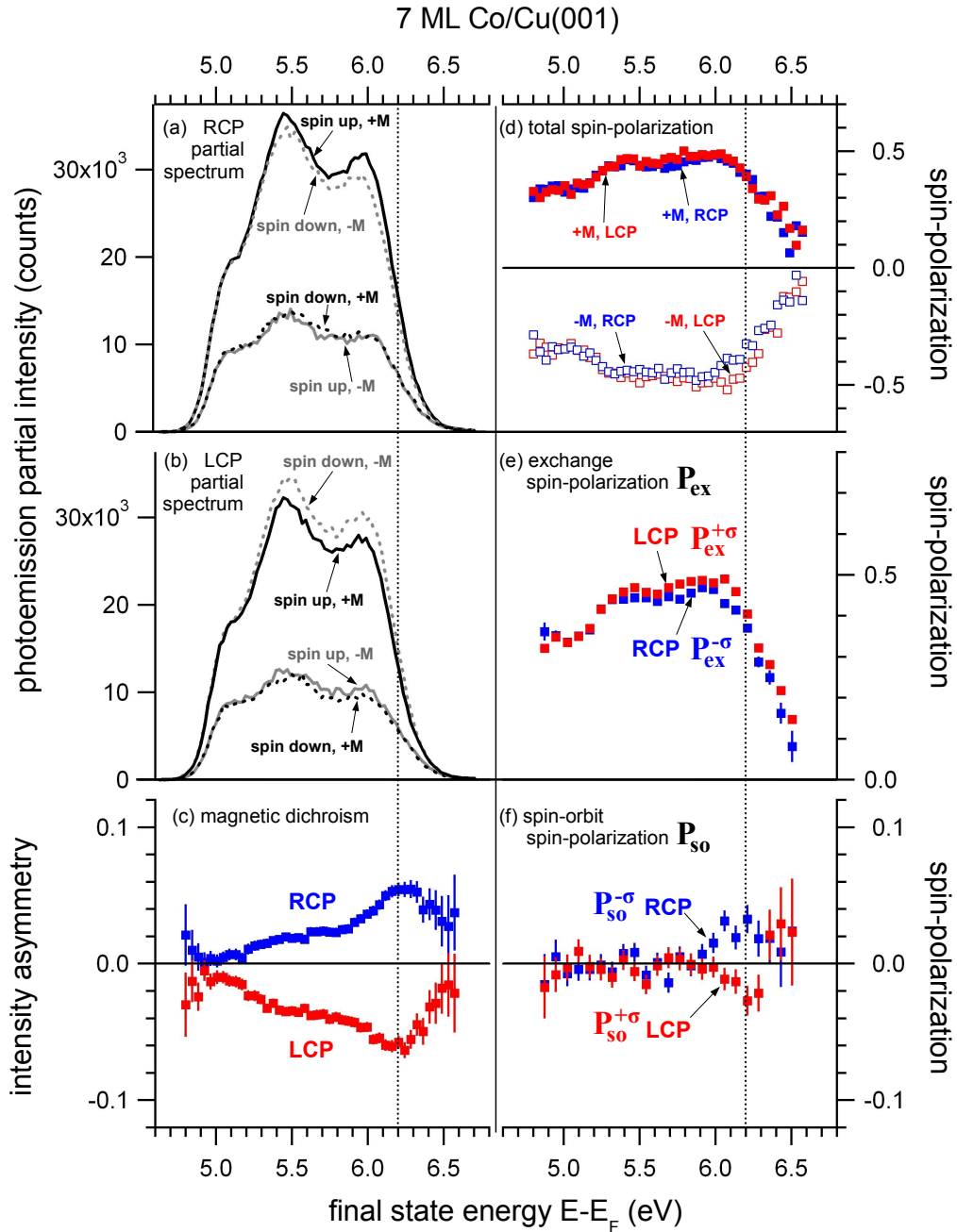


Figure 4.10: The eight spin-resolved photoemission spectra $I_{\pm S, \pm M}^{\pm \sigma}$ measured from a 7 ML cobalt film for magnetization directions along $+M : [110]$ and $-M : [\bar{1}\bar{1}0]$ with (a) right- and (b) left-circularly polarized light ($\pm\sigma$). $h\nu=3.1$ eV. (c) Magnetic circular dichroic signal A_{MCD}^{σ} , (d) total spin-polarization $P_{\pm M}^{\pm \sigma}$, (e) exchange spin-polarization $P_{ex}^{\pm \sigma}$ and (f) spin-orbit spin-polarization $P_{SO}^{\pm \sigma}$. Dashed lines mark the photoemission from the Fermi level. The peak feature of spectra in (a) and (b) are 2PPE through the unoccupied quantum well state.

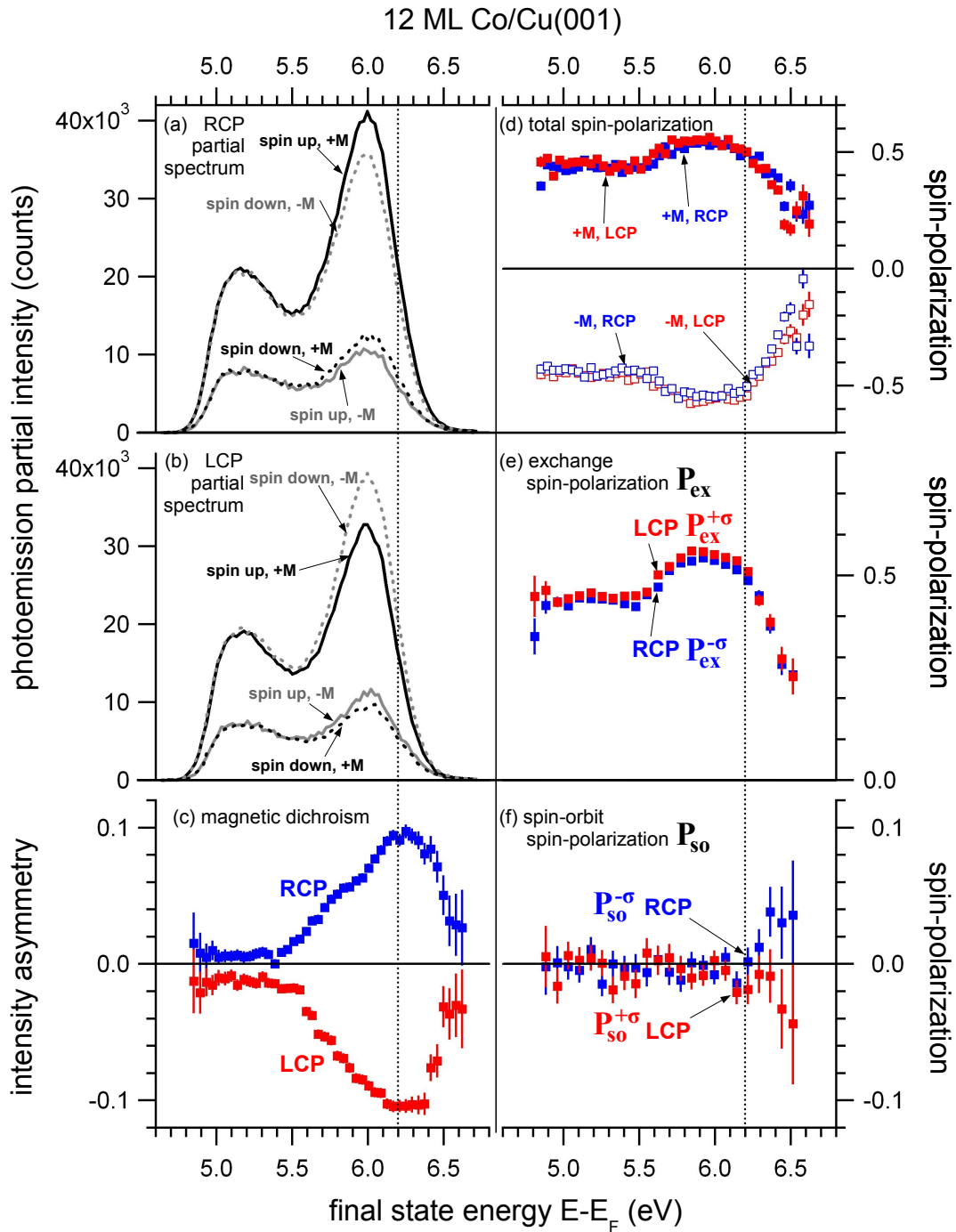


Figure 4.11: Same as Fig. 4.10, but for 12 ML Co/Cu(001).

polarization which does not reverse with magnetization ($P_{so}^{\pm\sigma}$) is within our resolution smaller than 1% over the energy range from 4.9 to 5.9 eV, and shows small signature at around the 6.0 eV, where the photoemission takes place from near the Fermi level. This small signal in $P_{so}^{\pm\sigma}$ is in coincidence in energy to the largest magnetic dichroic signal $A_{MCD}^{\pm\sigma}$ around the Fermi level in Fig. 4.10c. Both $P_{so}^{\pm\sigma}$ and $A_{MCD}^{\pm\sigma}$ reverse upon light helicity reversal. This implies a relation between the spin-orbit spin-polarization $P_{so}^{\pm\sigma}$ and the magnetic dichroism, which will be discussed in section 5.4. For the case of 12 ML cobalt film, the exchange spin-polarization $P_{ex}^{\pm\sigma}$ also dominates the photoelectron spin-polarization as shown by the large magnitude in Fig. 4.11e. The spin-orbit spin-polarization $P_{so}^{\pm\sigma}$ in Fig. 4.11f is smaller than the statistical error over the whole investigated energy range from 4.9 eV to 6.4 eV.

Our results show that the exchange spin-polarization dominates the photoelectron spin-polarization in our experiments. This is in contrast to many core-level photoemission experiments from ferromagnetic materials [66, 90–92], in which the strength of spin-orbit coupling is large in the core level and the exchange interaction due to the spin-polarized valence electrons is small. This will be further discussed in section 5.4.

4.5 Excitation power dependence

It has been shown by several groups that the incident laser power may strongly influence the precise energy position as well as the energy broadening of spectral features through the different density of photoelectrons above the sample. The origins of this effect are the Coulomb interaction between the photoelectrons themselves (space-charge) and between photoelectron and their mirror charges in the sample [163–165]. In the following, the incident power dependent spectral shift and broadening in magnetic dichroism and spin-polarization are summarized for reference. The incident power of the laser beam has been measured just before the entrance lens of the chamber. The diameter of the focus spot at the sample is estimated to be in the order of 50 μm .

Based on the experimental conditions, the number of photoelectrons per pulse can be estimated. The total number of electrons emitted from the sample during every single laser pulse is estimated from the sample current, which is around 1 nA with incident laser power of 80 mW on Cu(001) and 3 nA on Co/Cu(001). Considering the repetition rate 81 MHz of our laser pulses, this gives an estimation of a total amount of 80 and 200 electrons/pulse on Cu(001) and Co/Cu(001). The number of photoelectrons going through the energy analyzer for each laser pulse is evaluated by numerical integration of the photoemission spectrum in Fig. 4.12 and then divided by the integration time for acquiring the spectra and divided by the repetition rate. This gives a value of 0.3–1.0 electron/pulse. With these parameters, the induced energy broadening (δE) and energy shift (E_S) of an assumed 40 fs Gaussian electron pulse can be estimated by models in the literature: $\delta E \leq 10$ meV and $E_S \leq 10$ meV according to Hellmann *et al.* [164], and

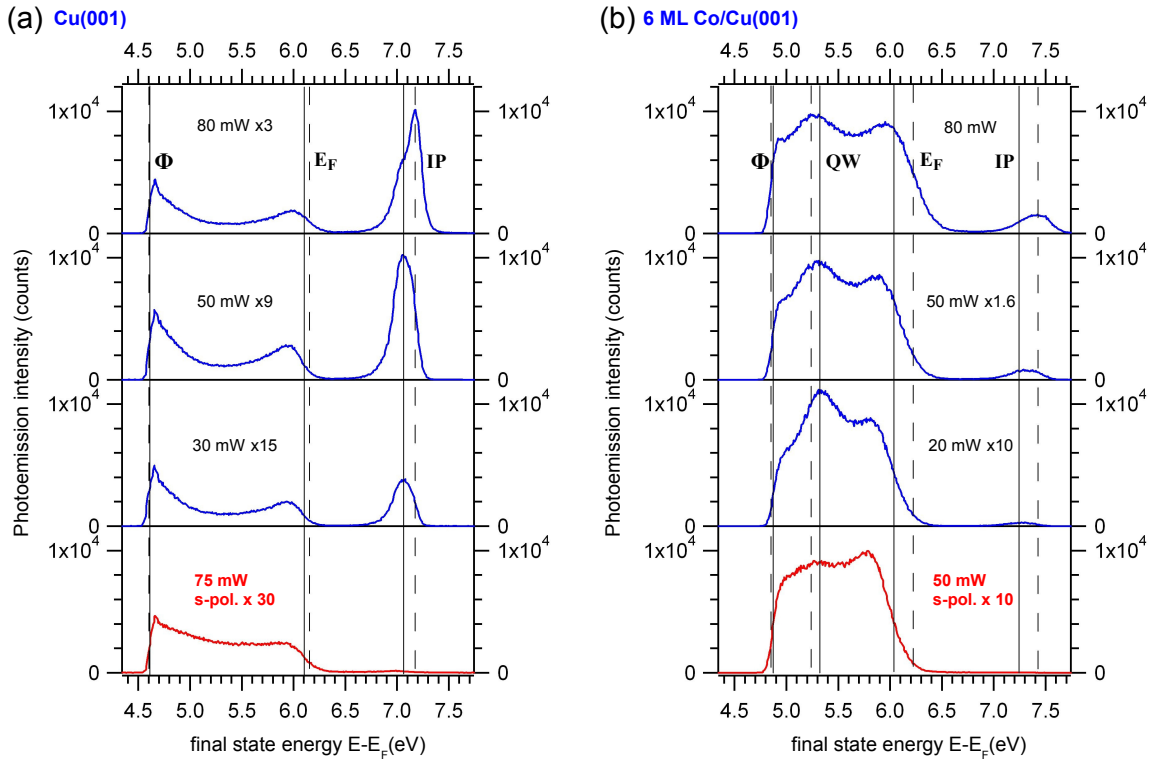


Figure 4.12: Photoemission spectra measured from (a) Cu(001) and (b) a 6 ML cobalt film on Cu(001). The central photon energy is 3.06 eV for both cases and the incident light is p -polarized. Three solid/dashed lines mark the vacuum edge (Φ), the photoemission Fermi edge (E_F) and the peak from $n=1$ image potential state (IP) determined from the spectra measured with high/low power (80/30 mW in (a) and 80/20 mW in (b)). In (b) the features of the cobalt unoccupied quantum well state are also marked (QW).

$\delta E \leq 70$ meV according to Passlack *et al* [163].

The dependence of photoemission spectra on the incident laser power for p -polarized light is displayed in Fig. 4.12. In the top panel of Fig. 4.12a, the spectra taken on Cu(001) with average power 80 mW show the vacuum level cutoff feature at a final state energy of 4.6 eV and the Fermi level feature at 6.15 eV. The three-photon photoemission through the image potential states gives rise to a peak at around 7.15 eV. These features are marked by the vertical dashed lines. The same features determined from the spectra measured with 30 mW are marked by the solid lines, which are located roughly at the same energies as those determined from the spectra measured with s -polarized light in the bottom. From this comparison we clearly observe, as the laser power is reduced from 80 mW to 30 mW, that the vacuum cutoff remains at the same energy around 4.6 eV, whereas the feature from the Fermi level shifts by about 0.05 eV and the image potential state peak shift by 0.1 eV.

We further investigate the power dependence in the spectra measured from cobalt films in Fig. 4.12b. The feature from the Fermi level shifts to lower energy by 0.2 eV when we reduced the laser power from 80 mW to 20 mW, and the peak due to photoemission through the quantum well state shifts to higher energy by 0.1 eV. The image potential state peak moves to lower energy by 0.2 eV.

From these laser power dependent measurements we can have an estimation that the space charge effect is almost negligible at 20-30 mW incident laser power, which is determined by the agreement of Fermi level features in the spectra obtained by the p -polarized light with that of the s -polarized light, as shown in the lowest two panels in Fig. 4.12a and Fig. 4.12b.

More importantly, we compare the photoemission spectra from 7 ML cobalt films for 80 mW and 20 mW laser incident power, measured with circularly polarized light. In Fig. 4.13a, the spectra for two opposite magnetization directions ($+M : [110], -M : [\bar{1}\bar{1}0]$) are shown in the upper and middle panels for 80 mW and 20 mW, and the intensity asymmetry upon sample magnetization reversal is derived in the bottom panel. The features of vacuum level, quantum well states and the Fermi edge are determined from the spectra and marked by the vertical lines. There is a difference in the dichroic signal between the results obtained with 80 mW and 20 mW, which is a shift in energy by about 50 meV. Despite this shift, contribution from the unoccupied quantum well state and from the Fermi level are clearly seen for both cases.

In Fig. 4.13b the spin-resolved photoemission spectra are shown, where we also mark the spectral features. As displayed in the bottom panel, the observed spin-polarization does not show significant differences beyond the statistical error. For both cases, the spin-polarization is dominated by the spin-up contribution and the slightly enhanced spin-polarization at the quantum well state feature remains visible at around 5.6 eV.

We summarize that we do observe a spectral shift in the photoemission spectra, which depends on the incident laser power and originates from the excitation density of photoelectrons above the surface. This gives rise to an energy shift $E_S \leq 0.2$ eV at photoemission from the Fermi level between the average incident power density 2.6 GW/cm² and 0.6 GW/cm² during the laser pulse for p -polarized light, and $E_S \leq 0.05$ eV for the circularly polarized light. Comparing the observation between these two incident power densities, we conclude a corresponding deviation in the values of magnetic dichroic signal and spin-polarization as 2% and 5%. These effects, however, do not influence our conclusion of the spin-resolved and magnetic dichroic measurements.

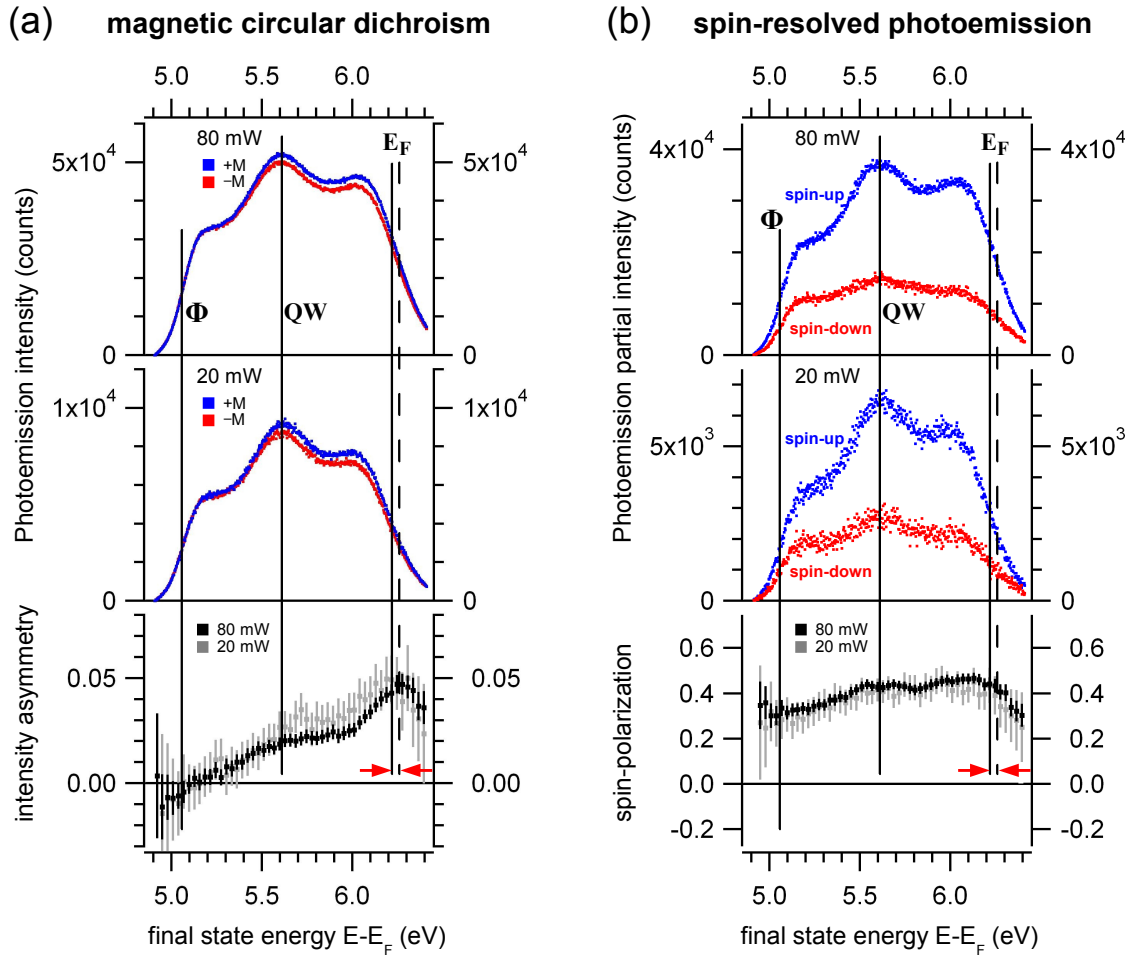


Figure 4.13: Comparison of (a) magnetic circular dichroism and (b) spin-resolved photoemission acquired with right circularly polarized light at two different average power of incident light, 20 mW and 80 mW, with the same acquiring time. The sample is 7 ML Co/Cu(001). The photon energy is 3.11 eV. The vertical solid and dashed lines mark the features of the vacuum edge (Φ), the quantum well state (QW) and the photoemission Fermi edge (E_F). The energy of Fermi edges are estimated by the position at half intensity of the d -band feature at 6.1 eV. These is a visible shift by 50 meV between E_F in the spectra for incident laser power of 20 mW to 80 mW (arrows).

Chapter 5

Discussion

In this chapter, the experimental results of chapter 4 are discussed. First we compare the characteristics of unoccupied quantum well states in section 5.1 with the theoretical modeling, numerical calculations, as well as previous reports in the literature. The selection rules and the interference between photoemission pathways underlying the magnetic dichroism are discussed in section 5.2. The spin-dependent role of the intermediate states in two-photon photoemission is discussed in section 5.3. The exchange and spin-orbit parts of spin-polarization are discussed in section 5.4. In section 5.5 and section 5.6 the intensity oscillation during cobalt film growth and the photoemission probing depth are discussed.

5.1 Characterization of unoccupied quantum well states

5.1.1 Energy dispersion

The comparison between Fig. 4.1a and Fig. 4.1b indicates that the dispersive photoemission feature as a function of cobalt thickness is due to an unoccupied state in the cobalt films. In Fig. 5.1 the intermediate state energy of this unoccupied state is shown by the black squares. These energy values are derived by subtracting their final state energies in Fig. 4.1a by the photon energy. Since their energies depend characteristically on the cobalt thickness, it is plausible to assign them to quantum well states in the cobalt film. To support this assignment, a model calculation is performed, based on the phase accumulation of the electron wave function being scattering between the cobalt film surface and the cobalt-copper interface, in the direction perpendicular to the film surface [99]. The majority states from the cobalt unoccupied *sp*-band are selected in our model since the spin-resolved measurements (Fig. 4.6a) have shown a dominant majority spin signal at these unoccupied state features (discussion in section 5.1.2). The one-dimensional phase accumulation model imposes a restriction on the total phase change of wave function after a round trip between the interface and the surface, which is required to be a multiple of

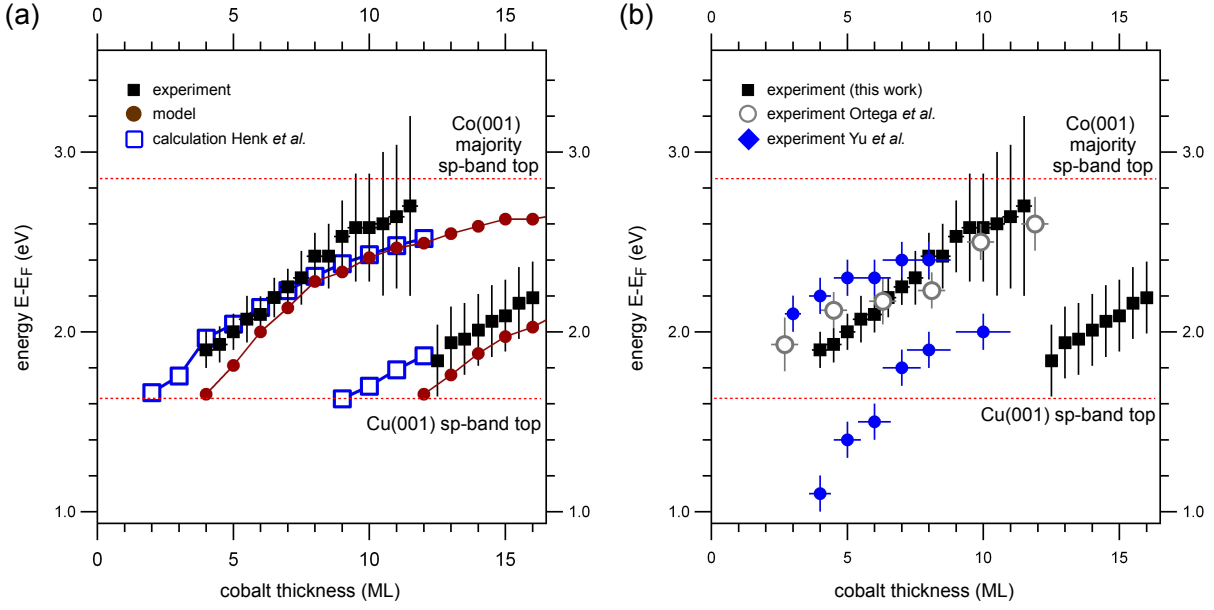


Figure 5.1: (a) The dispersion of unoccupied quantum well states as a function of cobalt thickness. Black squares show experimental data extracted from Fig. 4.1a. The solid circles are calculated by the phase accumulation model for majority states (Eq. 5.1 [99]). The blue empty squares are from the numerical calculation for majority states in the cobalt thin film by Henk [47]. (b) Comparison to the inverse photoemission experiments from Ortega *et al.* [136] and Yu *et al.* [135].

2π . This is explicitly written as [99]:

$$2k_{\perp}(E)t + \phi_C(E) + \phi_B(E) = 2m\pi. \quad (5.1)$$

The dependence of wave vector $k_{\perp}(E)$ on the energy E is extracted from the bulk band structure of fct cobalt (Fig. 2.2) [47], d is the film thickness and m is an integer. The crystal phase $\phi_C(E)$ and the barrier phase $\phi_B(E)$ are the phase shifts of the electron wave function after reflection from the periodic potential of copper substrate and from the surface barrier on the cobalt film. They are modeled by [99]:

$$\phi_C(E) = 2 \sin^{-1} \left[\frac{E - E_L}{E_U - E_L} \right] - \pi \quad (5.2)$$

$$\phi_B(E) = \pi \left[\frac{3.4eV}{\Phi_V - E} \right]^{\frac{1}{2}} - \pi. \quad (5.3)$$

We take $E_L=1.63$ eV for the copper lower bulk band edge $X_{4'}$ and 2.85 eV for the cobalt majority lower band edge at $X_{4'}$. These values are from the numerical calculations by Henk (see: Fig. 2.2) [47]. We use $E_U=7.0$ eV for the copper upper band edge at X_1 from van Gelderen *et al.* [166]. These values are referred to the Fermi level, and they are reasonable as compared to other values in the literature (Tab. 5.1). Φ_V is the cobalt surface work function and is set to a value of 4.75 eV, which is measured from the low energy cutoff in the photoemission spectra (Fig. 4.1a) and is in good agreement to the reported

band edges at X -point	energy with respect to the Fermi level
$X_{4'}$ copper	1.63 eV [47] ; 1.6 eV [166] ; 1.8 eV [171]
X_1 copper	7.0 eV [166] ; 7.1 eV [105] ; 7.8 eV [167]
$X_{4'}$ cobalt, majority	2.85 eV [47] ; 2.5 eV [167] ; 2.4 eV [166]

Table 5.1: Values of the energy of band edges in fcc copper and fct cobalt band structures reported in the literature.

value 4.72 eV in the literature [167]. The crystal phase ϕ_C in Eq. 5.2 is an empirical form [99] which has an approximated energy dependence [168] and a change of π over the band gap. The surface barrier phase ϕ_B is derived from the Wentzel-Kramers-Brillouin (WKB) approximation using an image potential like function ($1/z$) away from the surface with a saturation near the surface [169, 170]. Both the phases ϕ_B and ϕ_C were originally derived from the matching of the wave functions at the interface and at the surface [98, 102].

With $k_{\perp}(E)$, $\phi_C(E)$, and $\phi_B(E)$ given from the bulk band structures of copper and cobalt as mentioned above, the energy at which Eq. 5.1 is satisfied can be solved for each integer thickness of the cobalt film (t is equal to a multiple of the cobalt interlayer spacing $d_{Co} = 1.73 \text{ \AA}$ [108]). The result is shown in Fig. 5.1a by the solid circles. The agreement between our model and experiments in Fig. 5.1a is good, especially for the cobalt thickness above 5 ML. Below 5 ML the use of the bulk cobalt band structure should be less appropriate. The agreement supports our assignment of the dispersive features in two-photon photoemission spectra to the unoccupied quantum well states (Fig. 4.1a). In addition, we compare the data with theoretical calculations by Henk [47] in Fig. 5.1a and inverse photoemission experiments in Fig. 5.1b. Both our experimental data and model agree well with the theoretical calculations, and agree reasonably to the inverse photoemission data from Ortega *et al.* [136], whereas a larger deviation appears when we compare with the spin-resolved inverse photoemission data from Yu *et al.* [135].

In addition to the thickness dependent energy of the quantum well states, the electron density of quantum well states can be estimated for further understanding. By using the nearly free-electron approximation [172], the dispersion of bulk sp -bands of copper and cobalt from Henk [47] are fitted by two plane waves in the region near the first Brillouin zone boundary (X_1 and $X_{4'}$ points). The modeled two plane waves are hybridized by the potential V_{int} with period equal to the interlayer distance d ($d_{Cu(001)} = 1.805 \text{ \AA}$ [121] and $d_{Co(001)} = 1.73 \text{ \AA}$ [108]). In our model, V_{int} is responsible for the band gap in the band structure at X -point in the Brillouin zone. In addition, a constant potential V_0 is used to align the absolute energy position to fit the band structure from Henk [47]. To reproduce the copper band structures along the Δ direction (parallel to the surface normal), we use values of the potential $V_{int}^{Cu} = 2.7 \text{ eV}$ and $V_0^{Cu} = -7.3 \text{ eV}$. To reproduce the lower branch of the cobalt band below the band gap, $V_{int}^{Co} = 3.2 \text{ eV}$ and $V_0^{Co} = -6.6 \text{ eV}$ are used. This nearly-free electron approximation provides us not only the real part of wave vectors at each energy, but also an imaginary part of the wave vector [98, 172, 173], describing the decay of electron wave function within the band gap. The complex wave vector for

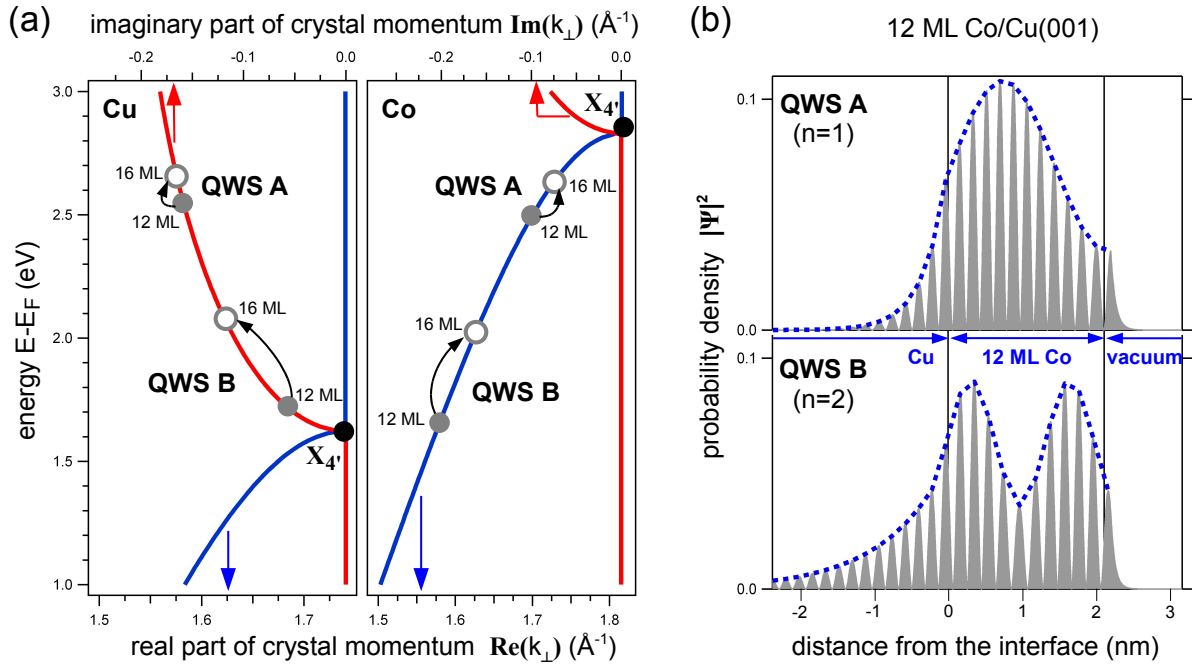


Figure 5.2: (a) Unoccupied bulk band structure of copper (left) and cobalt (right). The real (blue, lower scale) and imaginary (red, upper scale) parts of the wave vector of electronic states along the surface normal ($\overline{\Gamma X}$) are shown as functions of energy (details see in the text) [47]. Solid and empty gray circles mark the energy and wave vector of quantum well states in the cobalt films. As the cobalt thickness increases from 12 ML to 16 ML, Eq. 5.1 is satisfied at other k_\perp as shown by the arrows. (b) Model calculation of the probability density of quantum well states in a 12 ML cobalt film (details in text). QWS A,B have corresponding energy and complex-valued wave vector inside the copper band gap and real wave vectors inside the cobalt film as indicated in (a). Dashed curves are the envelopes of the probability density.

electronic states in copper and cobalt are shown in Fig. 5.2a by the blue and red curves, in the region near the top of the sp -bands ($X_{4'}$) along the $\overline{\Gamma X}$ direction perpendicular to the film surface. The electron wave functions of the quantum well states are obtained by matching the wave functions at the cobalt-copper interface and the cobalt film surface, as imposed by Eq. 5.1, determining the allowed wave vectors inside the cobalt film. The probability density of derived wave functions are shown in Fig. 5.2b for the case of 12 ML cobalt film. For simplicity, the wave function in the vacuum region is approximated by an exponential decay determined by the energy relative to the vacuum level ($\Phi_V \approx 4.75$ eV).

For the 12 ML cobalt film, we have two quantum well states satisfying Eq. 5.1, as indicated by QWS A and QWS B in Fig. 5.2a, with probability density shown in Fig. 5.2b. The envelopes (dashed curves) have one and two maxima for QWS A and B, corresponding to the conventional terminology $n=1$ and $n=2$ quantum well states [96]. If the wave vector k_{\perp} in Eq. 5.1 is replaced by its deviation from the Brillouin zone boundary: $k_{BZ} - k_{\perp}$, with $k_{BZ} = \pi/d_{Co}$, the number of maxima in the envelope (n) and the integer number m in Eq. 5.1 will be identical [101]. This explains the envelopes as a beating pattern of the electron wave function due to the mismatch between the wave vector and the cobalt interlayer periodicity [136]. By Eq. 5.1 this beating pattern (envelope) is matched to the boundary at the interface and the surface. Moreover, as shown in Fig. 5.2b, the quantum well states have a finite probability in the copper substrate. This penetration of quantum well state wave function in the substrate is more pronounced at energies closer to the copper substrate band edge (QWS B) than that at higher energy (QWS A). The same physical picture was also found for quantum well states in Ag/Au(111) [96, 174, 175] and provides explanation for the hybridization between the quantum well states and the bulk substrate electronic bands [176–179]. A similar phenomenon exist as well at the surface side in Fig. 5.2b, where the quantum well states have a tail in the near surface region, allowing a possible hybridization with surface electronic states [180, 181].

By our experimental results and model calculations, the confinement of the quantum well states along the surface normal direction is illustrated. In the directions parallel to the film surface we observed the dispersion with the parallel component of the electron wave vector k_{\parallel} , as shown in the angle-dependent photoemission spectra in Fig. 5.3. A parabolic fit to the dispersion in Fig. 5.3b yields an effective mass about half of the free electron mass ($0.5 m_e$), which is close to the value of $0.46 m_e$ [182] for unoccupied quantum well states which has been found for copper sp -bands at 1 eV above the Fermi level.

This fit value does not, however, necessarily correspond to the real curvature of cobalt sp -bands because the confinement at the interface and surface of the quantum well states depends also on the parallel wave vector k_{\parallel} . This can be easily seen in Fig. 5.3b where the copper band edge depends strongly on k_{\parallel} and consequently provides a k_{\parallel} dependent reflection from the interface. In our phase accumulation model this means a k_{\parallel} dependent phase shift ϕ_C in Eq. 5.2, leading to a quantized momentum k_{\perp} which depends on the value of k_{\parallel} (Eq. 5.1). The resultant energy dispersion of quantum well states, therefore, can not

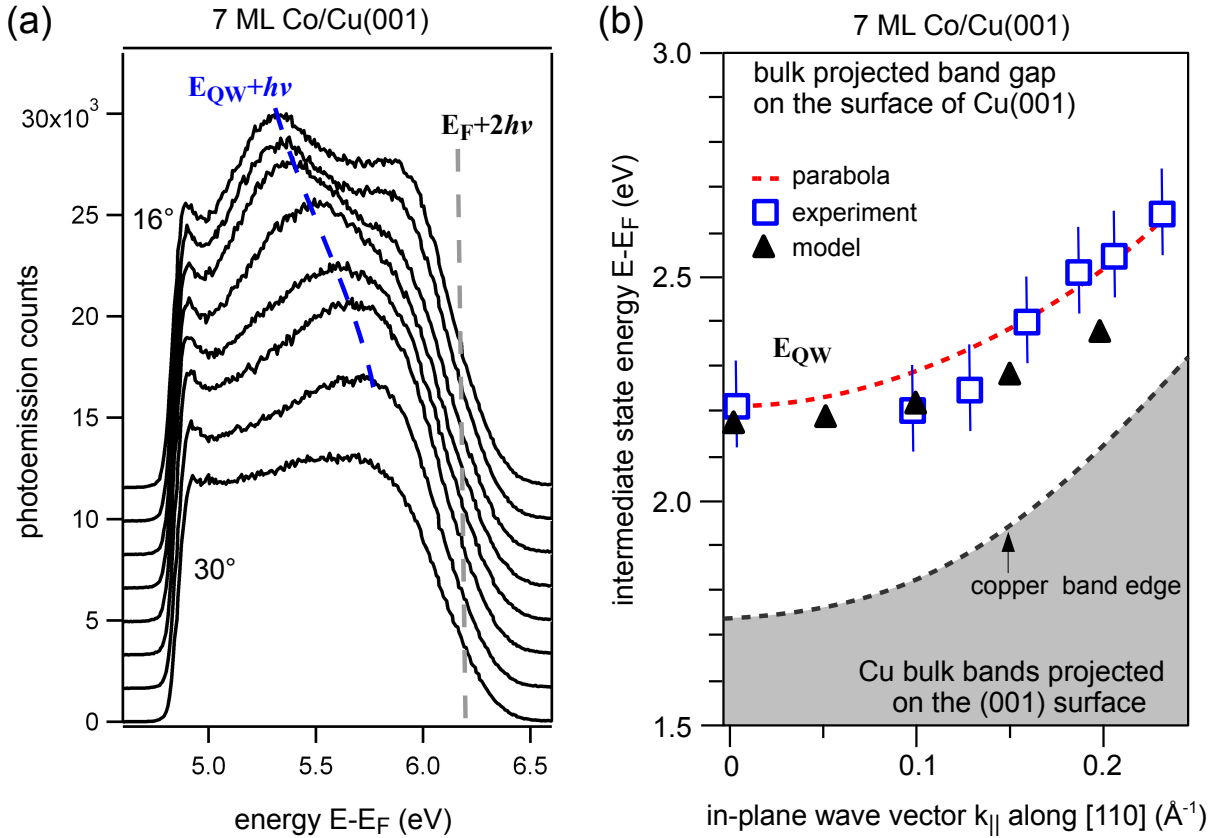


Figure 5.3: (a) Angle-dependent two-photon photoemission spectra from 7 ML Co/Cu(001) measured with p -polarized light and $h\nu=3.09$ eV. The emission angle is 16° to 30° from top to bottom, with 2° step. The spectra are shifted vertically by 1.65×10^3 counts for clarity. (b) Dispersion of quantum well state (E_{QW}) along $\bar{\Gamma}\bar{X}$ is deduced from the off-normal photoemission data in (a) and normal emission data in Fig. 4.1 (blue squares). The filled area indicated the bulk bands projected on the Cu(001) surface [155, 185]. The dashed curve is a parabolic dispersion with effective mass half of the electron. The black triangles are from the phase accumulation model (Eq. 5.1).

be described by a simple relation such as $E(k) = E(k_{\parallel}) + E(k_{\perp})$, in which we assume that k_{\perp} is independent of k_{\parallel} . The dependence of the quantized k_{\perp} on the continuous k_{\parallel} was reported in the literature for quantum well states as well as for the image potential states [183, 184] and can be taken into account by the phase accumulation model including the k_{\parallel} dependence of the copper band gap. The results are shown in Fig. 5.3b by the black triangles. For simplicity, only the dispersion of the lower band edge of copper is considered, and the effective mass of the cobalt sp -band along [110] is modeled as half of the free electron mass. The deviation between the model calculation and the parabolic dispersion in our case is still small due to the limited k_{\parallel} range under our investigation.

5.1.2 Spin character and spin-orbit coupling

In our spin-resolved measurements in Fig. 4.6a the majority spin signal dominates the two-photon photoemission through the unoccupied quantum well states. Since the experiments for data in Fig. 4.6a were performed with linearly polarized light, the non-relativistic

selection rules in our geometry preserve the electron spin in the optical transition [23]. The dominant majority signal in photoemission measured at the final state energy consequently indicates the majority intermediate and initial states in the photoemission process. The unoccupied quantum well states, involved as intermediate states here, are therefore of majority spin character.

The spin-resolved 2PPE spectra from 6 ML and 9 ML Co/Cu(001) with p -polarized light are shown in Fig 5.4a and Fig 5.4b, compared with the theoretical band structure. For both cases, the one-photon transition from majority bands below the Fermi level (E_F) to unoccupied quantum well states is possible as indicated by the arrows. This leads to higher 2PPE intensity at the final state energy one photon energy higher than the quantum well states, and this is observed as a peak in 6 ML spin-up spectrum as well as a shoulder in the 9 ML spin-up spectrum. The majority Δ_5 band near E_F has less dispersion near the X -point, indicating a higher density of states and explains the increasing 2PPE intensity near 6 eV in both spin-up spectra. In the spin-down spectra, we observed features similar to the spin-up spectra with a lower intensity, and there is no apparent feature of minority quantum well states. The data will be further compared with one-photon photoemission, as shown in Fig. 4.9 and discussed in section 5.3.

To further characterize the quantum well states, we now consider not only the exchange splitting between majority and minority bands, but also the spin-orbit interaction. As a result, the electron spin is not a good quantum number to classify the energy bands, and the hybridization between bands of different spatial symmetry (Δ_1 , Δ_5 for example) and different spin occurs. The strongly hybridized regions are marked in Fig 5.4 by the gray circles. Moreover, this hybridization between electronic bands has consequences to the optical transition, leading to the magnetic dichroism in photoemission (section 2.2). As follows, the spin-orbit coupling in the quantum well states is discussed based on our magnetic dichroic measurements.

Here we focus on the magnetic linear dichroism in two-photon photoemission shown in Fig. 4.2 and Fig. 4.3. They are summarized in Fig. 5.5. The magnetic linear dichroism shows a maximum dichroic asymmetry of about 10% at the feature of quantum well states (dashed lines), and at the same energies a small magnetic circular dichroic signal 3% is also observed, overlapping with a larger contribution near 6.0 eV. Since spin-orbit coupling is required for forming magnetic dichroism, our observations indicate the influence of spin-orbit coupling in the two-photon photoemission process through the intermediate quantum well states. To identify the source of spin-orbit coupling in the electronic structure, we take the calculated cobalt band structure as a reference. As shown in Fig. 5.4, the cobalt initial states which are relevant for photoexcitation through the quantum well states show a spin-orbit hybridization between Δ_5 and Δ_2 majority bands at about $E_F-0.6$ eV (gray circle), and a spin-orbit influenced minority surface resonance at $E_F-0.4$ eV [130]. A significant effect from these initial states on the observed dichroism is not compatible with the fact that the dichroic signal of the dispersing quantum well state feature for

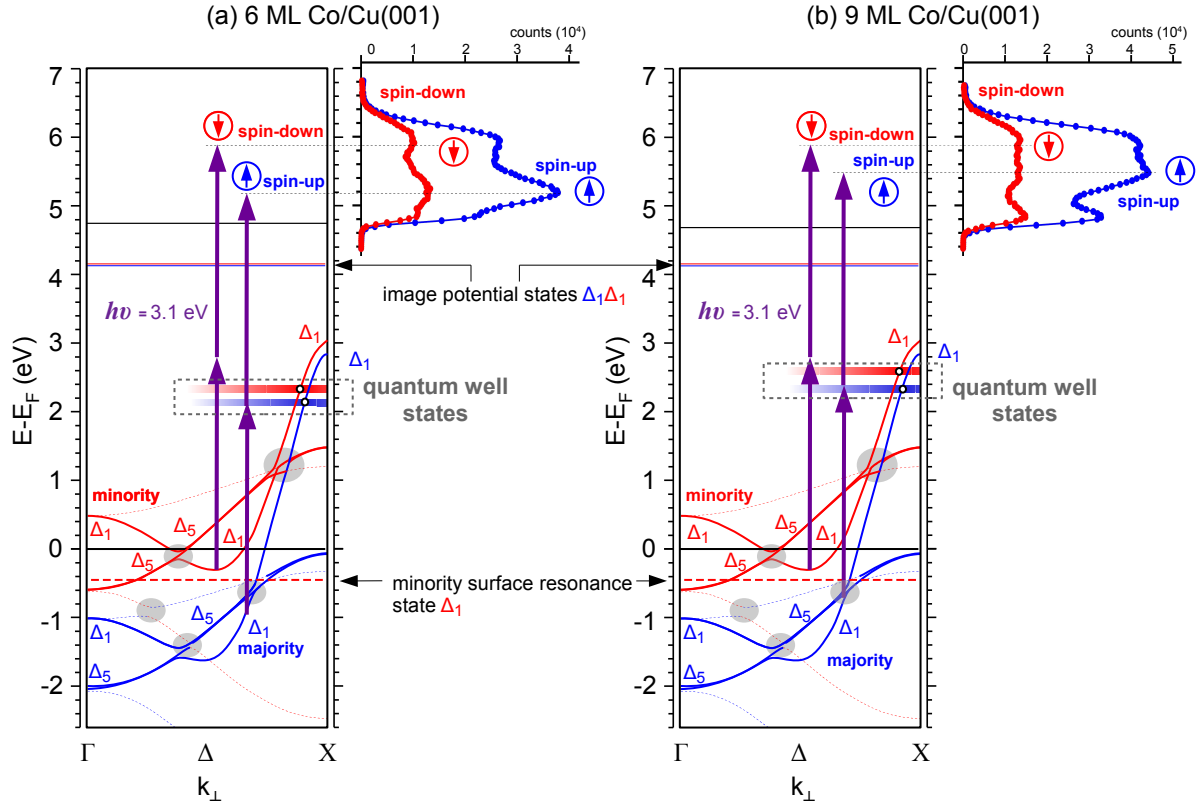


Figure 5.4: The relativistic electronic structure of Co/Cu(001) along the surface normal ($k_{\perp} \parallel [001]$) [104]. The unoccupied sp -bands and quantum well states (circles) are calculated by Henk [47], accompanying with an illustrative broadening in crystal momentum $\Delta k_{\perp} \approx 0.5\Gamma\bar{X}$. The size of this broadening is three times of the interval between quantized k_{\perp} at the film thickness 6 ML. The reason for the quantization of k_{\perp} is due to the finite thickness. The spin-resolved 2PPE spectra obtained with p -polarized light are shown for comparison. The majority and minority bands are indicated by blue and red curves. The solid curves represent bands dominated by Δ_1 or Δ_5 bands, which are accessible in our normal emission geometry by p - and s -polarized light. The dashed curves are dominated by symmetry of Δ_2 and Δ_2' . Gray circles indicate the spin-orbit hybridization which mixes bands of different spatial symmetries. The minority surface resonance state is at 0.4 eV below E_F [104, 130] and the exchange-split image potential states are around 4.1 eV above E_F [39]. The vertical arrows indicate the photon energy 3.1 eV and illustrate the transition from majority and minority bands.

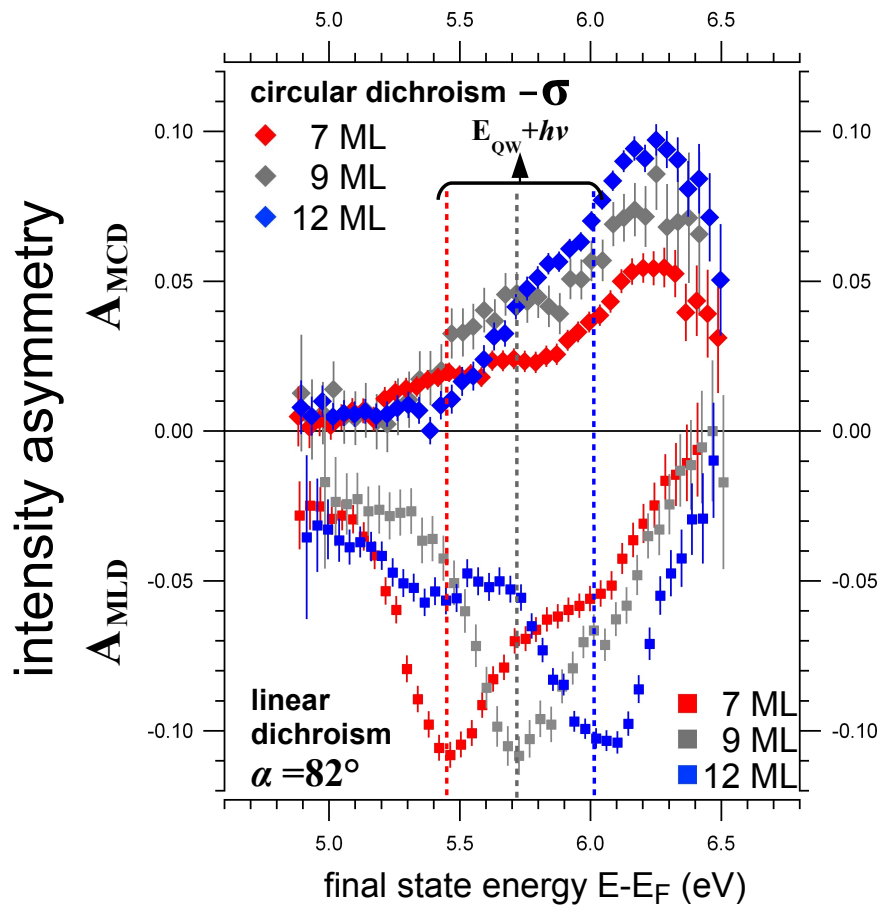


Figure 5.5: The dichroic signals in two-photon photoemission spectra for different cobalt thickness, as summarized from Fig. 4.2 and Fig. 4.3. Dashed lines mark the features of quantum well states in the spectra.

linearly polarized light shows almost no variation in Fig. 5.5 while the relevant initial states move through the strongly variable region of the band structure between $E_F-0.8$ eV and $E_F-0.2$ eV.

Concerning the final states, which are required to have Δ_1 symmetry for our normal emission geometry (Fig. 3.2), we can exclude final state diffraction [186, 187] and surface transmission [188, 189] effects because they are forbidden in a normal-emission geometry with magnetization and optical plane along a high symmetry crystal direction [187, 189]. This is also supported by the zero signals in the linear polarization dependent measurements as shown in Fig. 4.5, where we obviously have $A_{MLD}(\alpha = 0^\circ, \pm 90^\circ) = 0$, which will not be strictly satisfied if the photoemission direction deviates from the optical plane. Since initial and final states are unlikely to dominantly cause our observed dichroic signals, we are lead to consider the intermediate quantum well states. In the cobalt band structure (Fig 5.4), at energy about 1.2 eV above the Fermi level, there is a hybridization between the unoccupied sp -bands and the unoccupied cobalt minority d -band due to spin-orbit coupling [47]. This specific hybridization point is about 1.5 eV lower in energy than the intermediate quantum well states we observed (2.4 to 2.9 eV above E_F). In this case, the strength of spin-orbit coupling decreases gradually from the hybridization point up to the energy region of quantum well states and the phase difference between hybridized bands of different spatial symmetry does not have a sign change in the observable range. This generally leads to a single-signed magnetic dichroism in both A_{MCD} and A_{MLD} [188] and is in agreement with the observed dichroic signal throughout our investigation (Fig. 5.5).

We also exclude the possible contribution of magneto-optical effects to the dichroic signal in photoemission. The magneto-optical effect can lead to to magnetic dichroism, when the incident polarized light is transmitted into the sample differently depending on the sample magnetization [190]. The Kerr rotation and ellipticity can change the polarization of transmitted light and consequently influence the photoemission intensity. This is, however, contradicted by our observation in Fig. 4.5 of an α -independent shift angle $\Delta\alpha$ in A_{MLD} , which in addition is too large for a linear magneto-optical rotation as estimated from known magneto-optical constants ($\theta_{Kerr} \approx 0.5^\circ$ at $h\nu = 3$ eV [191]).

Following the above qualitative considerations, the magnetic dichroism in our observation is ascribed to the spin-orbit coupling in the intermediate unoccupied quantum well states. This picture is confirmed recently by the numerical calculations from Henk [47] where direct one-photon photoemission from the quantum well states is considered and is discussed in section 5.2. The dominant majority character of the quantum well states in our observation is consistent with the absence of a zero point in the magnetic dichroic signal (Fig. 5.5) due to marginal spin-orbit interaction away from the hybridization point. For the case of strong spin-orbit hybridization, the spin character of electronic bands can change across the spin-orbit hybridization gap and gives rise to a sign change of spin-polarization [43, 47].

5.2 Tuning interference between photoexcitation channels in ferromagnets

To explain the magnetic linear dichroic signals we observed, an interpretation based on an incoherent sum of contributions from p - and s -polarized light is insufficient, since no dichroic signal can be detected under the action of p - or s -polarized incident light alone (section 4.2). Rather, an explanation based on a *coherent* superposition of the transitions induced by the p - and s -polarized light is required. In our experiment we used variable linear polarization of light defined by the angle α (Fig. 3.2). Considering the one-photon photoemission (1PPE) intensity $I^{\pm M}$ in our geometry after Eq. 2.6, the intensity depends on the magnetization and is a function of α :

$$I^{fi,\pm M}(E_f) \propto \cos^2 \alpha \left(\sin^2 \theta \left| E \mu_{\perp}^{fi,+M} \right|^2 + \cos^2 \theta \left| E \mu_{\parallel,p}^{fi,+M} \right|^2 \right) + \sin^2 \alpha \left| E \mu_{\parallel,s}^{fi,+M} \right|^2 \pm \sin 2\alpha \times \Re \left[E^2 \sin \theta \mu_{\perp}^{fi,+M} \mu_{\parallel,s}^{fi,+M*} \right]. \quad (5.4)$$

This result is obtained by Eq. 2.6 using the notation in Fig. 2.1a, which describes the linearly polarized light by $(E_{\perp}, E_{\parallel,s}, E_{\parallel,p}) = (E \cos \alpha \sin \theta, E \sin \alpha, E \cos \alpha \cos \theta)$ for our geometry. θ is the angle of refraction in the sample. The material optical response is neglected at this moment and can be included by the Fresnel coefficients, which gives a complex value of angle θ [78, 192].

The magnetization dependent intensities in Eq. 5.4 vary as functions of the incident linear polarization (angle α). Experimentally we measured the magnetization dependent intensities of two-photon photoemission (2PPE) through the quantum well states in Fig. 4.5 and the polarization dependence is very pronounced. The data are reproduced here in Fig. 5.6 and are compared to the analytical 1PPE form in Eq. 5.4 in the following. This comparison is based on the assumption that the initial states of 2PPE do not contribute strongly to the polarization dependence of the photoemission intensity and the magnetic dichroic signal. Based on these two assumptions, we can effectively compare the transition between intermediate state and the final state in 2PPE to the 1PPE formula in Eq. 5.4. For the magnetic dichroic signal in 2PPE via quantum well states, the contribution of initial states is examined experimentally in Fig. 5.5. The magnetic linear dichroic signal follows the dispersion of quantum well states as a function of cobalt thickness and does not show strong dependence on the initial states that are coupled. This observation suggests a relative weak contribution in the dichroic signal from the initial states in 2PPE through the quantum well states.

For better comparison, we decompose the photoemission intensity into components which are the sum of intensities over sample magnetization $\pm M$ (I^{sum}) and the difference between intensities with $\pm M$ (I^{diff}). The analytical results follow from Eq. 5.4 as:

$$\begin{aligned}
I^{fi,sum}(E_f) &= I^{fi,+M} + I^{fi,-M} \\
&\propto \underbrace{\cos^2 \alpha \left(2 \sin^2 \theta |E\mu_{\perp}^{fi,+M}|^2 + 2 \cos^2 \theta |E\mu_{\parallel,p}^{fi,+M}|^2 - 2 |E\mu_{\parallel,s}^{fi,+M}|^2 \right)}_A \\
&\quad + \underbrace{2 |E\mu_{\parallel,s}^{fi,+M}|^2}_B \\
I^{fi,diff}(E_f) &= I^{fi,+M} - I^{fi,-M} \propto \sin 2\alpha \times \underbrace{\Re \left[2E^2 \sin \theta \mu_{\perp}^{fi,+M} \mu_{\parallel,s}^{fi,+M*} \right]}_{-C} \quad (5.5)
\end{aligned}$$

The experimentally observed difference and sum intensities $I^{fi,diff}(E_f)$ and $I^{fi,sum}(E_f)$ as well as the magnetic dichroic asymmetry ($A_{MLD} = I^{fi,diff}/I^{fi,sum}$) are shown in Fig. 5.6. They are compared with the analytical results from Eq. 5.5 (solid curves). We use the experimental values A, B and C in Fig. 5.6 to model the analytical terms relating to the transition dipole matrix elements in Eq. 5.5. This leads to: $I^{sum}(\alpha) = A \cos^2(\alpha) + B$ and $I^{diff}(\alpha) = -C \sin(2\alpha)$. As we can see in Fig. 5.6, the α -dependent variation A is much larger than the α -independent intensity B and the magnetization difference intensity C. As we go back to Eq. 5.5, the experimental findings $A > B, C$ means that the transition dipole elements between quantum well states and the 2PPE final state satisfy the condition $\mu_{\perp} > \mu_{\parallel,s}$ or $\mu_{\parallel,p} > \mu_{\parallel,s}$. This is consistent with the expectation $\mu_{\perp} \gg \mu_{\parallel,s}$ as a result of the dominant Δ_1 symmetry of the sp -bands, where the quantum well states are derived (Fig. 5.4), and the Δ_1 symmetry of the final states in our normal emission geometry.

From the experimentally determined relative size of A, B, and C, we have $AB \gg C^2$ and Eq. 5.5 can be approximated to give a simple description of the magnetization dependent intensity $I^{\pm M}(\alpha)$:

$$\begin{aligned}
I^{\pm M}(\alpha) &= \frac{I^{sum}(\alpha) \pm I^{diff}(\alpha)}{2} \\
&\propto \frac{A}{2} \cos^2 \alpha + \frac{B}{2} \mp \frac{C}{2} \sin 2\alpha \\
&= \frac{A}{2} \left(\cos^2 \alpha \mp \frac{2C}{A} \sin \alpha \cos \alpha \right) + \frac{B}{2} \\
&= \frac{A}{2} \left(\cos \alpha \mp \frac{C}{A} \sin \alpha \right)^2 + \frac{B}{2} - \frac{C^2}{2A} \sin^2 \alpha \\
&= \frac{A^2 + C^2}{2A} \left(\frac{A}{\sqrt{A^2 + C^2}} \cos \alpha \mp \frac{C}{\sqrt{A^2 + C^2}} \sin \alpha \right)^2 + \frac{B}{2} - \frac{C^2}{2A} \sin^2 \alpha \\
&= \frac{A^2 + C^2}{2A} [\cos(\alpha \pm \Delta\alpha/2)]^2 + \frac{B}{2} - \frac{C^2}{2A} \sin^2 \alpha \\
&\approx \frac{A^2 + C^2}{2A} \cos^2(\alpha \pm \Delta\alpha/2) + \frac{B}{2} \quad (5.6)
\end{aligned}$$

Here we use a notation: $\Delta\alpha = 2 \tan^{-1}(C/A)$. The result of this approximation is the phenomenological expression used in Fig. 4.5a for the magnetization dependent 2PPE

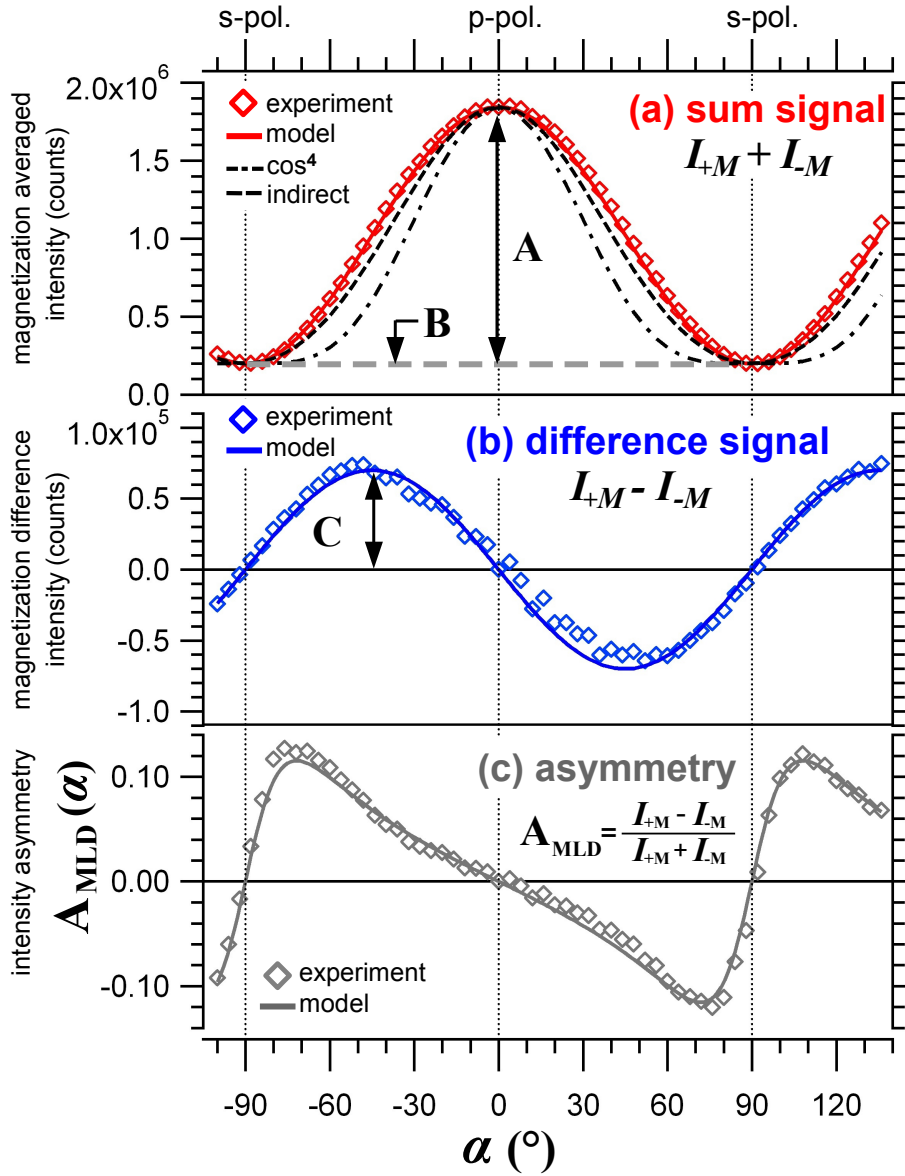


Figure 5.6: Magnetic linear dichroism in two-photon photoemission (2PPE) through the quantum well state in 7 ML Co/Cu(001) from Fig. 4.5. The tilt angle α of the electric field vector of the incident light is defined in Fig. 3.2. Photoemission intensities (a) sum, (b) difference, and (c) asymmetry over sample magnetization reversal are derived from the raw intensities in Fig. 4.5a. Solid curves are functional forms according to the one-photon photoemission model in Eq. 5.5: $I^{sum}(\alpha) = A \cos^2(\alpha) + B$ and $I^{diff}(\alpha) = -C \sin(2\alpha)$, with parameters A, B and C indicated. In (a), the dashed-dotted curve is a $A \cos^4 \alpha + B$ function for describing a 2PPE process with Δ_1 symmetry of initial, intermediate and final states, plus a background intensity B. The dashed curve is the modeled α -dependence based on indirect 2PPE process [61].

intensity $I^{\pm M}$. The experimental shift angle $\Delta\alpha$ is thus traced back to the ratio between transition dipole moments.

The $A \cos^2 \alpha$ variation of the measured sum intensity I^{sum} in Fig. 5.6a can provide us with further information about the dominant symmetry of the initial states in two-photon photoemission (2PPE). If we have all initial, intermediate and final states with dominant Δ_1 symmetry (2PPE process: $\Delta_1 \rightarrow \Delta_1 \rightarrow \Delta_1$), for example, I^{sum} should show a variation as $\cos^4 \alpha$ function because the transitions can only be coupled by the electric field perpendicular to the surface from the p -polarized component according to the selection rules [56, 57, 61]. This variation is shown in Fig. 5.6 by the dashed-dotted curve and does not agree with the data. If we have the initial states with Δ_5 symmetry, we have a 2PPE process $\Delta_5 \rightarrow \Delta_1 \rightarrow \Delta_1$ and the intensity I^{sum} varies as $\cos^2 \alpha$ because only the second transition $\Delta_1 \rightarrow \Delta_1$ requires the p -polarized component of electric field. The polarization (α) dependence of the first transition $\Delta_5 \rightarrow \Delta_1$ can be estimated by the electric field component parallel to the surface using the known angle of incidence and the Fresnel coefficients [78] (index of refraction $n=1.61+3.05i$ at 3 eV [193]). The transition $\Delta_5 \rightarrow \Delta_1$ turns out to be α -independent because the strength of the electric field parallel to the surface, which is responsible for the $\Delta_5 \rightarrow \Delta_1$ transition, is the same for s - and p -polarized light ($E_{\parallel,s} = E\sqrt{0.15}e^{-i45^\circ} \sin \alpha$, $E_{\parallel,p} = E\sqrt{0.15}e^{-i57^\circ} \cos \alpha$). The resultant α -dependence for 2PPE process $\Delta_5 \rightarrow \Delta_1 \rightarrow \Delta_1$ varies as $\cos^2 \alpha$ and shows the same variation as the 1PPE formula in Eq. 5.5 (solid curve in Fig. 5.6a).

We also compare our polarization dependent 2PPE intensity with another model, which has been used to identify the symmetry of adsorbate states on metals by Wolf *et al.* [61]. In this model, the mechanism of a polarization dependent 2PPE intensity comes from the indirect 2PPE process, in which the intermediate states are populated by an amount proportional to the absorption of light. The absorption of light is given by the absorbance A , defined as $A=(1 - |r|^2)$. r is the complex Fresnel reflection coefficient and depends on the incident polarization of light [78]. For the incident light of photon energy 3 eV, the absorbance is 0.32 for s -polarized light and 0.48 for p -polarized light in our geometry, and their difference gives rise to an α -dependent population in the intermediate state. According to the model from Wolf *et al.* [61], the population of the intermediate quantum well state varies as $0.48 \cos^2 \alpha + 0.32 \sin^2 \alpha$ in our case. By multiplying the α -dependence of transition from the quantum well state to the final state, which are dominated by the $\Delta_1 \rightarrow \Delta_1$ transition with a $\cos^2 \alpha$ dependence, the total variation of 2PPE intensity is proportional to $(0.48 \cos^2 \alpha + 0.32 \sin^2 \alpha) \times \cos^2 \alpha$, which gives us a small but still apparent deviation from our data in Fig. 5.6a (dashed curve).

The above comparison shows that the α -dependence in experiments is consistent with the assumption that the initial states in 2PPE through unoccupied quantum well states have a Δ_5 symmetry. This is reasonable when we refer to the band structure in Fig. 5.4. There are indeed Δ_5 occupied bands near the accessible initial states energy region. Also, the Δ_5 bands have higher density of states due to its less dispersion as compared to the

Δ_1 bands and could therefore dominate as initial states in our 2PPE process.

We further compare our results with theoretical first-principle calculations performed by Henk [47]. By a fully relativistic multiple-scattering method (layer Korringa-Kohn-Rostocker), Henk investigated the electronic structure of cobalt thin films grown on Cu(001) [47]. The bulk cobalt band structure of fct cobalt (2% tetragonal compression) was calculated as shown in Fig. 5.7. The circles in Fig. 5.7a and Fig. 5.7b highlight the hybridization between electronic bands due to spin-orbit coupling. The unoccupied quantum well states were calculated, and are used in Fig. 5.1a to compare with our experimental observations. The quantum well states are located in the energy range labeled by the gray areas in Fig. 5.7, just above the strongly spin-orbit hybridized region (circles). To confirm the observed magnetic dichroism in 2PPE by theoretical calculations, Henk used a one-step photoemission calculation [194, 195] and calculated the 1PPE intensity from the quantum well states in a 6 ML cobalt film on Cu(001) at 2.15 eV above the Fermi level. This calculation was performed by assuming the originally unoccupied quantum well state to be populated and act as the initial state in the 1PPE with incident photon energy 3.1 eV. This theoretical 1PPE process couples the same quantum well state with the same final state as in the experimental 2PPE process through the intermediate quantum well state. The 1PPE intensities from the quantum well states for two opposite directions of sample magnetization ($\pm M$ as in experiments) are shown in Fig. 5.8a. The intensity difference upon magnetization reversal is shown in Fig. 5.8b and the intensity asymmetry, which corresponds to the dichroic signal, is shown in Fig. 5.8c. In addition, the influence of material optical response, which gives rise to refraction of light in the material, is included by the Fresnel's coefficients calculated from the tabulated index of refraction. Inclusion of the optical response leads to a pronounced change in the dichroic signal calculated in Fig. 5.8c.

We compare the results from the calculations (Fig. 5.8) with the experiments (Fig. 5.6). The calculated intensity in Fig. 5.8a varies in a similar way as in the experiments in Fig. 5.6a, with maximum at $\alpha = 0^\circ$ indicating the dominant Δ_1 symmetry of the unoccupied quantum well states. This is also in agreement with the calculated band structure in Fig. 5.7a that the sp -bands in the gray areas, from which the quantum well states are derived, are dominated by the Δ_1 symmetry. The calculated intensity difference upon magnetization reversal in Fig. 5.8b is similar to the experimental results in Fig. 5.6b. Both of them have maxima near $\alpha = \pm 45^\circ$ and nodes at $\alpha = 0^\circ, \pm 90^\circ$. Both the calculated (Fig. 5.8c) and measured (Fig. 5.6c) intensity asymmetry have maximum around $\alpha = \pm 75^\circ$ and their shape are in good agreement. This comparison shows that the dichroic signal can be explained by only considering the spin-orbit coupling in the quantum well states and its influence to the one-photon transition from the quantum well states to the final states. This confirms the origin of observed dichroic signal as a result of the spin-orbit coupling in the quantum well states.

Looking at the calculated dichroic asymmetry in Fig. 5.8c closely, we see a large in-

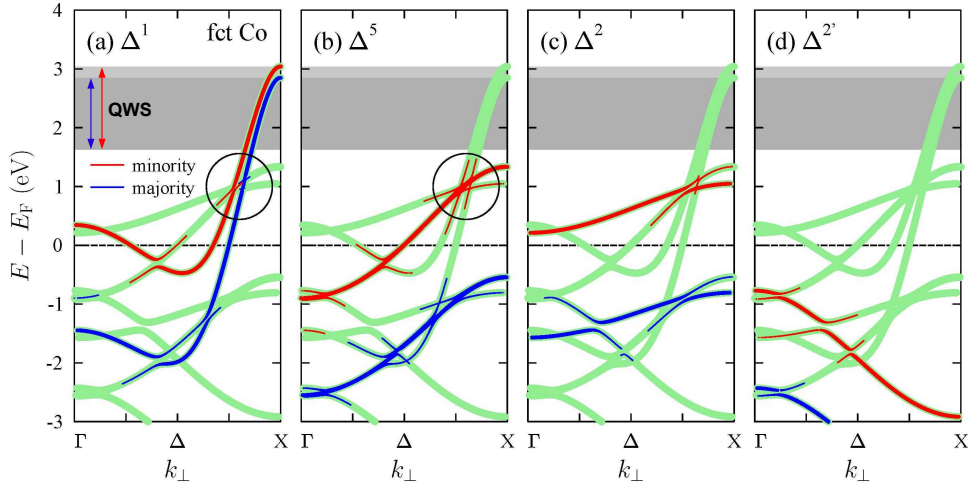


Figure 5.7: Band calculations of fct cobalt by Henk [47]. (a),(b) Electronic bands are shown by the green curves. They are decomposed into components satisfying different spatial symmetry properties in (a)-(d), as indicated by the blue and red curves for the majority spin and the minority spin bands. The minimum weight that is displayed in each column is 1%. The circles around 1 eV above the Fermi level (E_F) indicate the hybridization between different symmetry components in the electronic bands due to spin-orbit coupling. The gray areas show the energy range where the unoccupied quantum well states exist, blue arrow for majority and red arrow for minority states.

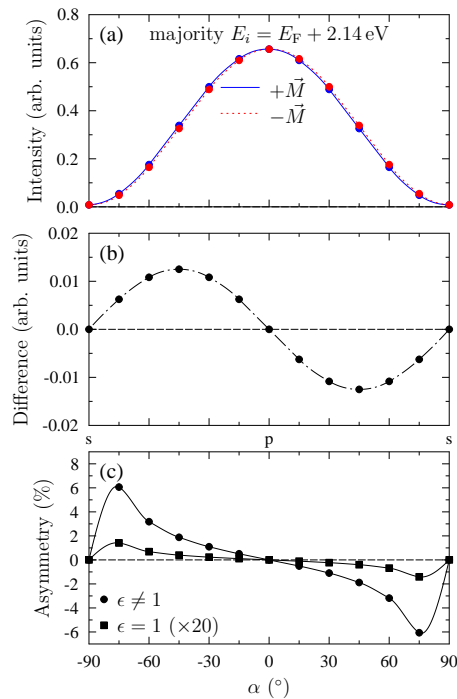


Figure 5.8: Theoretical one-photon photoemission intensity from the majority quantum well states in 6 ML cobalt thin films. Photon energy is 3.1 eV and the incident polarization of light is varied between p - and s -polarization as defined by the angle α . Sample magnetization $\pm M$ and the polarization angle α correspond to the situation in the experiments (Fig. 3.2 and Fig. 5.6).

crease in the *magnitude* of the signal when we introduce the effect of refraction by the Fresnel coefficients. The increased magnitude corresponds better to the experimental observation in Fig. 5.6c. The complex index of refraction ($n = \epsilon^2 = 1.61 + 3.05i$ at 3 eV [193]) leads to complex Fresnel coefficients, describing the phase shifts and magnitude changes of p - and s -polarized components of light in the sample after refraction [78]. Due to the phase shift between the p - and s -polarized components, the linearly polarized light becomes elliptically polarized in the cobalt films, with exception for only pure p - or s -polarized incident light. The magnetic dichroism therefore includes contribution not only from the magnetic linear dichroism with purely linearly polarized light, but also contribution from the magnetic circular dichroism with circularly polarized light. This phenomena was pointed out by Henk earlier [68]. To see the influence of refraction to the magnetic dichroic signals analytically, we refer to the term labeled as C in Eq. 5.5, which governs the size of the magnetic difference intensity. The relative phase between electric field components is introduced into C through the angle of refraction θ , which is a complex number in material with complex index of refraction [192]. The magnitude of the dichroic signal is therefore altered when the complex index of refraction is introduced. The α -dependence, which is determined by the factor $\sin 2\alpha$ before the term C in Eq. 5.5, however, is independent of the angle of refraction and is therefore not influenced by the refraction. This is seen in Fig. 5.8c by the same α -dependence for the cases $\epsilon \neq 1$ and $\epsilon = 1$.

In Fig. 5.6b and Fig. 5.6c, the magnetic dichroic signal is seen in the form of the intensity difference and the asymmetry. At $\alpha = \pm 90^\circ$ or 0° there is only one excitation channel coupled by s - or p -polarized light and no dichroism is observed. When both s - and p -polarized components exist and with equal intensities ($\alpha = 45^\circ$), the intensity difference in Fig. 5.6b reaches its maximum, indicating a mechanism which requires both p - and s -polarized components. This is nicely explained by the interference model (solid curves in Fig. 5.6 and Eq. 5.4). By tuning the incident polarization of light, the interference between photoexcitation channels coupled by p - and s -polarized components is suppressed at $\alpha = \pm 90^\circ$ and 0° according to Eq. 5.5 as well as shown by the zero signal in our observation in Fig. 5.6b.

5.3 Comparison between one- and two-photon photoemission

Here we discuss the electronic states involved in one- and two-photon photoemission (1PPE and 2PPE). These electronic states are: the initial states below the Fermi level, the final states above the vacuum level, and the intermediate states between the Fermi and vacuum levels. They are schematically shown in Fig. 5.9. As one can intuitively see in Fig. 5.9, the 1PPE and 2PPE processes could share the same initial and final states, provided the photon energy for 1PPE is exact twice of that for 2PPE ($h\nu_2 = 2h\nu_1$).

One of the possible initial states in our case are the spin-polarized electronic states in the cobalt film. The other candidates are the electronic states in the copper substrate. Since the optical extinction length λ_0 is much larger than the film thickness (12 ML \approx 2 nm), the initial states in the copper substrate can also be photoexcited. The optical extinction length can be estimated from the electric field decay inside the cobalt film according to the imaginary part of the index of refraction $\text{Im}(n)$ [192]. The optical penetration depth (λ_o) is [192]: $\lambda_o = [\frac{4\pi\text{Im}(n_{Co})}{400nm}]^{-1} \approx 10$ nm for photon energy 3.0 eV derived from $n = 1.61 + 3.05i$ [193], and $\lambda_o = [\frac{4\pi\text{Im}(n_{Co})}{200nm}]^{-1} \approx 9$ nm from $n = 1.36 + 1.78i$ for photon energy 5.98 eV [193].

The final states of both 1PPE and 2PPE are located in a cobalt band gap and are described by evanescent waves decaying inside the cobalt film and propagating in the vacuum [50, 196]. The decay length is estimated to be about 4 to 5 Å in the energy range 4.5 to 6.5 eV above the Fermi level by the slowly varying imaginary part of the wave vector perpendicular to the sample surface $\text{Im}(k_{\perp}) \approx 0.22\text{Å}^{-1}$ in that energy range. This value can be obtained from the nearly-free-electron band structure as we previously mentioned in section 5.1.1. The decay behavior of the final state provides us the surface sensitivity in our present experiments and is discussed in section 5.6. The other cause of the surface sensitivity in photoemission is the electron mean free path for electrons propagating in the cobalt films, which is 2 to 3 nm at energy 2 eV above E_F for majority electrons and first decreases toward higher energy [197, 198], and then increases after about 20-50 eV [199]. Further discussion on the depth range of photoemission is in section 5.6 where we compare the thickness dependent dichroic signals and spin-polarization together.

Since the energy levels of the initial and the final states in our 1PPE and 2PPE experiments are similar, it is expected that the large difference between 1PPE and 2PPE is due to the intermediate state, which plays no role in 1PPE but is relevant in 2PPE [55, 61–63, 200]. This effect has been shown in Fig. 4.1, where a direct comparison between 2PPE in Fig. 4.1a and 1PPE in Fig. 4.1b allows to identify the spectral feature due to the presence of the unoccupied quantum well states. The similar *d*-band features in both 1PPE and 2PPE from near the Fermi level in Fig. 4.1 are consistent with the expectation that the initial states are common in 1PPE and 2PPE. In addition, we refer to the spin-polarization in 1PPE and 2PPE data in Fig. 4.9, which are summarized here in Fig. 5.10. Fig. 5.10a provides evidence that the minority surface resonance state (SR) observed in 1PPE contributes negligibly to 2PPE. This is indicated by the observation that the spin-polarization measured from the 330 K grown film (HT) shows a dominant majority signal in 2PPE, and, in strong contrast to the 2PPE, a sign change of the spin-polarization is observed in 1PPE from the same sample. For the measurements on the 170 K grown film (LT), the spin-polarization of photoelectrons is dominated by the majority signals in both 2PPE and 1PPE.

In Fig. 5.10b, the difference in the spin-polarization between films grown at HT and LT is derived from the data in Fig. 5.10a. In addition to the different size of spin-polarization

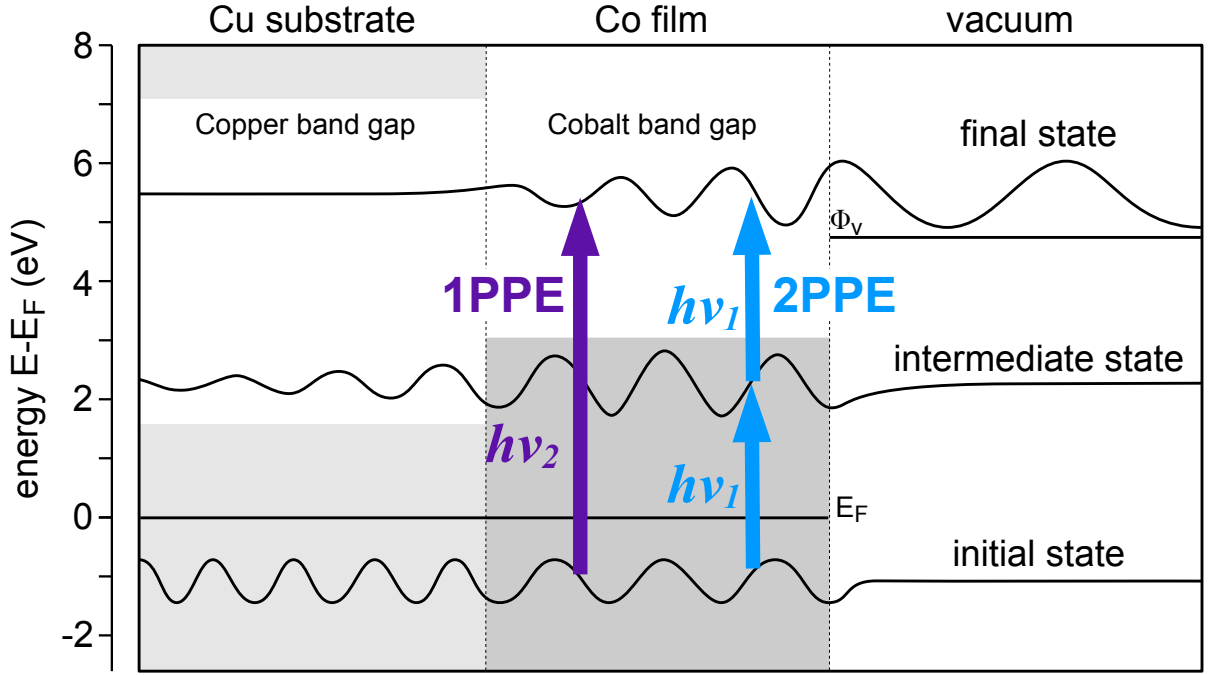


Figure 5.9: Schematic of electronic states in our one- and two-photon photoemission experiments (1PPE and 2PPE). The initial and final states participate in the former process, and additional intermediate state is involved in the latter. The projected bulk bands (gray) and band gap of fcc copper and cobalt along the $\bar{\Gamma}\bar{X}$ direction are shown.

in 1PPE and 2PPE over the whole energy range in Fig. 5.10a, we clearly observe a very different change in the spin-polarization between the 170 K and the 330 K grown sample in Fig. 5.10b. The energy at which a maximum change of spin-polarization occurs in 2PPE coincides with the feature of the unoccupied quantum well state (empty squares in Fig. 5.10b, $E_{QW} + h\nu_1$) and the change of spin-polarization is around +10%. This positive value means that the spin-polarization at this specific energy increases as we go from the 170 K (LT) grown film to the 330 K (HT) grown film, and is closely related to the fact that the unoccupied quantum well state is well developed in the HT-grown film, but not observed in the LT-grown film due to the poor surface quality [160–162].

In one-photon photoemission (1PPE), the maximum change of spin-polarization in Fig. 5.10 is located at around 5.6 eV ($E_{SR} + h\nu_2$). This energy coincides with the spin-down peak in the photoemission spectra (Fig. 4.9b middle panel), coming from the minority surface resonance state at 0.4 eV below the Fermi level [104, 130]. We relate this change of spin-polarization to the poorly ordered surface quality of the 170 K grown sample, on which the surface resonance state is strongly damped. In this comparison between 2PPE and 1PPE with different growth temperature, we can check not only the influence of the growth on different electronic states, *i.e.*, the surface state and the quantum well state are sensitive to the surface quality, but also draw conclusions on the relative importance of the electronic states involved in these two different photoemission processes. From the change of spin-polarization in Fig. 5.10b we conclude a dominating influence of the intermediate majority quantum well states in 2PPE and the influence of initial minority

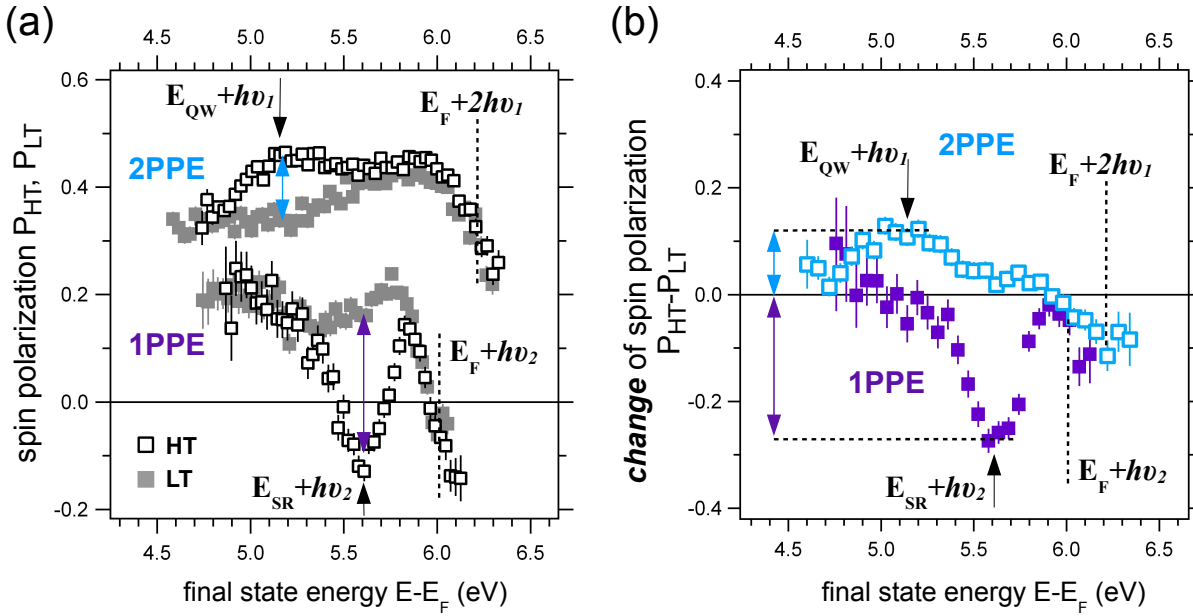


Figure 5.10: (a) Photoelectron spin-polarization in one- and two-photon photoemission (1PPE and 2PPE) from Fig. 4.9, measured from the 6 ML Co/Cu(001) sample grown at 330 K (HT) and 170 K (LT). The photon energies are $h\nu_1=3.1$ eV and $h\nu_2=6.0$ eV. Incident light is p -polarized. (b) The difference in the measured spin-polarization in 1PPE (solid squares) and 2PPE (empty squares) between films grown at 330 K and 170 K. They are derived from (a). E_{SR} and E_{QW} denote the energies of surface resonance state and unoccupied quantum well state.

surface resonance state in 1PPE, and, more importantly, the almost vanishing contribution from the initial minority surface resonance state to the 2PPE signal. The last conclusion is based on the fact that the observed spin-polarization in 2PPE almost shows no change at the corresponding energy of the surface resonance state in Fig. 5.10b ($E_{SR} + 2h\nu_1 = 5.8$ eV).

To check the critical influence of the initial and final states in 1PPE and 2PPE, which can be slightly different due to the small mismatch between photon energies ($h\nu_2=6.0$ eV $<$ $2h\nu_1=6.2$ eV), additional experiments were also performed with the photon energies chosen as $2h\nu_1 = h\nu_2=6.0$ eV (reduced light intensity). The result is shown in Fig. 5.11. Almost the same spin-polarization in 2PPE as the earlier 2PPE case is observed (HT in Fig. 5.10a), especially for the enhancement of spin-polarization at the majority quantum well state ($E_{QW} + h\nu_1 = 5.3$ eV) and the missing contribution from the minority surface resonance state ($E_{SR} + 2h\nu_1 = 5.6$ eV).

Since the initial and final states of 1PPE are at the same energies as those in 2PPE for the chosen condition in Fig. 5.11, the overall higher spin-polarization in 2PPE compared to 1PPE can be interpreted by the spin-conserving photoemission process through the intermediate majority quantum well states. The optical transition occurs between electronic states, with a probability determined by the transition dipole matrix element. In the non-relativistic approximation, the electric dipole operator does not contain any spin dependence and only the states with the same electron spin can be coupled. With a majority quantum well state as the intermediate state, we can only couple it to the ma-

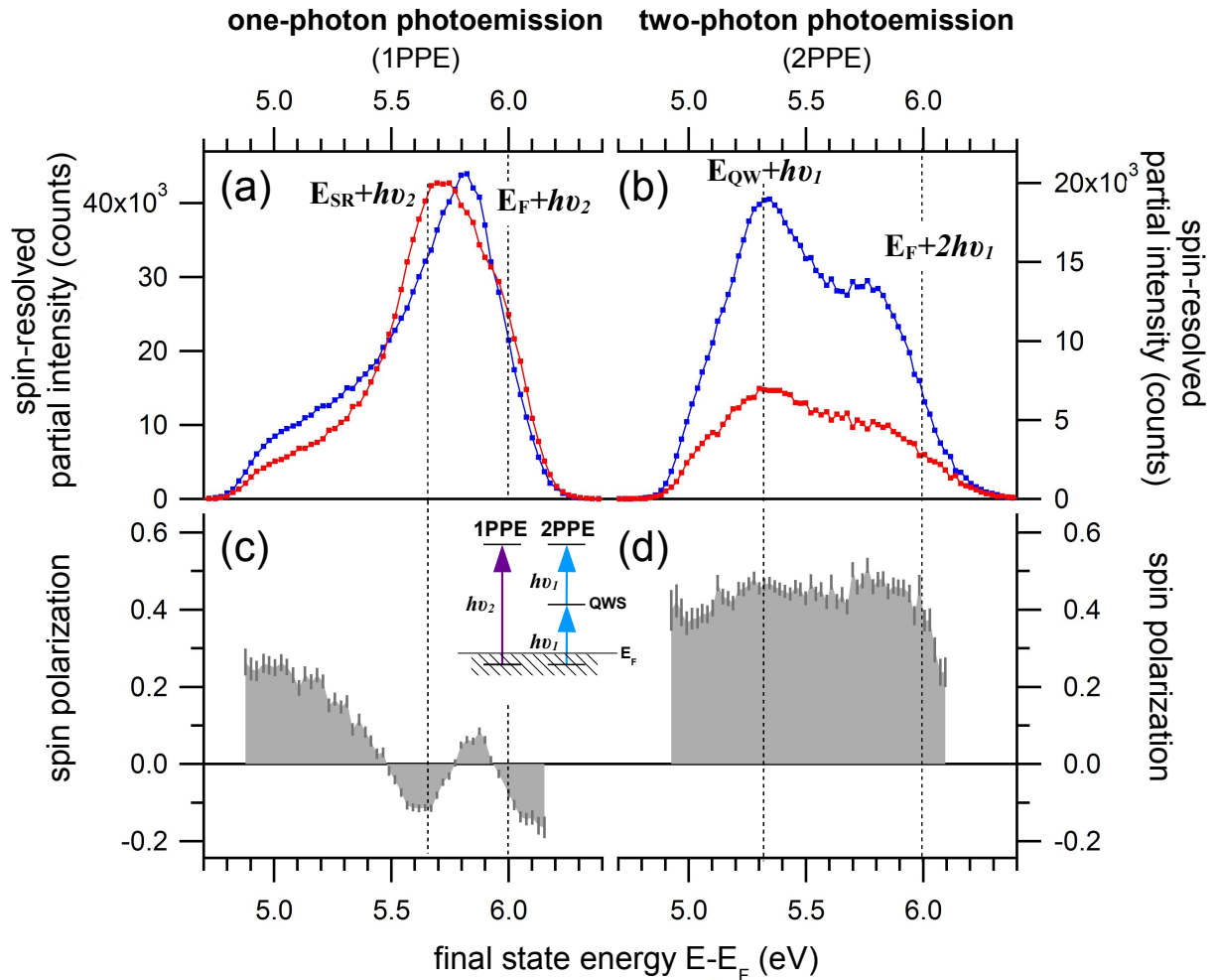


Figure 5.11: Spin-resolved (a) one-photon and (b) two-photon photoemission from 310 K grown 7 ML Co/Cu(001) with photon energy $h\nu_1=3.0$ eV and $h\nu_2=6.0$ eV. The incident light is p -polarized. The spin-polarization for spectra shown in (a) and (b) are displayed in (c) and (d). The features from the minority surface resonance state ($E_{SR} + h\nu_2$) and majority quantum well state ($E_{QW} + 2h\nu_1$) are indicated. Inset shows the different excitation schemes for one- and two-photon photoemission (1PPE and 2PPE).

majority initial state as well as majority final states. This coupling between majority states results in a positive spin-polarization in 2PPE if only majority intermediate state exists and if there are available majority initial states. For the case of 1PPE, no intermediate states should be involved in the optical transition, and both majority and minority initial states can contribute, coupling to the majority and minority final states.

In our present case, the unoccupied *minority* quantum well state derived from the unoccupied *sp*-band is not observed, whose existence in the cobalt film at energies near the majority counterpart has been shown by inverse photoemission experiments and theoretical calculations (exchange splitting between them: $\Delta E_{ex} \approx 0.2 \text{ eV}$) [47, 135]. The absence of unoccupied minority quantum well states in the 2PPE spectra can be discussed from two aspects. The first aspect is concerning the suitable initial states where electrons can be excited into the the minority quantum well states. As shown by the cobalt band structure in Fig. 5.4, the minority initial bands which can be coupled with *p*-polarized light in our normal emission geometry, *i.e.*, the Δ_1 and Δ_5 bands, exist only above 0.6 eV below the Fermi level. This means that, if we consider strict energy conservation in the photoexcitation, that only the minority intermediate states with above energy 2.4 eV can be coupled for incident photon energy 3.0 eV. In addition, if we consider only vertical transitions in k_{\perp} (momentum conservation) as in Fig. 5.4, the available initial states nearest to the minority quantum well states in k_{\perp} at suitable energies are located around $k_{\perp} = 0.5\overline{X}\Gamma$ and -0.3 eV below the Fermi level, indicating a possible transition only to the intermediate state at 2.7 eV above the Fermi level with photon energy 3.0 eV. This value is already close to the top of cobalt minority *sp*-band at *X*-point ($\approx 3.0 \text{ eV}$) in the band structure (Fig. 5.4), and it is already above the minority quantum well states energy for the cobalt thickness range up to 12 ML in numerical calculations [47]. The consideration of the momentum and energy conservation in the optical transition therefore provides us a possible explanation for the absence of 2PPE features from minority quantum well state for the cobalt film in our investigation range.

The second aspect is the shorter lifetime of the minority quantum well states due to the larger phase space for energy relaxation processes as compared to the majority states. This shorter lifetime can result in a spectral broadening and lower intensity in the photoemission spectrum, preventing observation of a sharp feature. Since minority quantum well states are located at higher energy levels than the majority quantum well states, there exist more empty minority states lying energetically below the minority quantum well states than the majority ones below the majority quantum well states. This can be easily seen from the band structure in Fig. 5.4. This difference between minority and majority quantum well states gives rise to a higher probability for electrons in the minority quantum well states to be scattered into lower energy states because there are more empty final states available [201]. The scattering process itself, which mediates the energy relaxation of excited electrons in the quantum well states, is not necessarily spin-dependent and can be such as electron-phonon scattering. There are

also the spin-dependent electron-hole pair excitation (Stoner excitation) [202], as well as the strongly spin-dependent inelastic scattering with spin-waves, which allows, as a consequence of angular momentum conservation, only the minority electrons for the energy loss process that emits the spin-wave [39, 203, 204]. The spin-wave modes in the cobalt thin films could be excited by the minority photoexcited electrons in the unoccupied quantum well states, which are located about 1.5 eV to 2.7 eV above the Fermi level, with energy much more than the spin-wave energy in Co/Cu(001) ($E_{SW} \leq 0.5$ eV [126]). In summary, the higher probability of energy relaxation for excited minority electrons than that of the majority electrons should lead to a shorter lifetime of photoexcited minority electrons, and consequently a more severe broadening of minority quantum well states in the photoemission spectra [39].

In addition, we consider the overlap between the initial occupied states and the unoccupied quantum well states, which plays an important role in the transition matrix element of photoexcitation. The initial cobalt bands in the bulk band structure and the quantum well states have their dominant weighting in the cobalt film (Fig. 5.2b). In contrast, the surface resonance state has a dominant weighting in the near surface region. This leads to a reduced overlap between the minority surface resonance state and the minority quantum well states as compared to that between the majority bulk bands and the majority quantum well states. Consequently, the transition matrix elements between the minority surface resonance state and the minority quantum well states are smaller than the transition matrix elements between the majority bulk bands and the majority quantum well states. From this we expect a smaller contribution in photoemission intensity from the transition between the minority surface resonance state and the minority unoccupied quantum well states as compared the contribution from the transition between the majority bulk bands and the majority quantum well states.

To summarize, our comparison between spin-resolved one-photon and two-photon photoemission directly reveals the spin-dependent influence of the majority intermediate quantum well state. Due to the spin-conserving optical transition induced by the linearly polarized light, the large difference in the photoelectron spin-polarization between 1PPE and 2PPE comes from the opposite spin alignment between the initial surface resonance state (minority) with the intermediate quantum well state (majority). The former has sizable contribution in 1PPE, leading to a sign change in the spin-polarization, but contributes negligibly in the 2PPE signal. We discussed possible reasons for the absence of spectral features of the unoccupied minority quantum well states by considering the energy- and momentum-conservation in the optical transition as well as the lifetime broadening in the photoemission spectra and the overlap between wave functions.

5.4 Relation between spin-polarization and magnetic dichroism

The spin-resolved photoemission experiments in section 4.4 have shown an additional spin-polarization accompanying the magnetic circular dichroism (P_{so} , Eq. 2.10). This is seen for a 7 ML cobalt film in Fig. 4.10f. In addition, a sign reversal as in the magnetic circular dichroism between right- and left-circularly polarized light also exists in P_{so} , indicating an underlying relation between the magnetic dichroism and the photoelectron spin-polarization in our geometry.

We begin our discussion by looking at the mirror symmetry in our experiments with respect to the optical plane (Fig. 3.2). This is exemplified in Fig. 5.12 for the case of right- and left- circularly-polarized light (RCP/LCP) incident on the sample $\pm M$ for magnetization along $[110]$ and $[\bar{1}\bar{1}0]$. The spin-resolved photoemission intensity is represented by $I_{s,M}^\sigma$, with $\sigma = \pm\sigma$ indicating the left-/right-circularly polarized incident light, and $s = \pm s$ for the spin-up/down partial intensities emitted from a sample magnetization along $[110]$ or $[\bar{1}\bar{1}0]$, as denoted by $M = \pm M$. Since we use a normal emission geometry where the detected photoelectrons are emitting along the surface normal direction in the optical plane (OP), a mirror operation with respect to the optical plane for the whole experimental geometry (m_{OP}) keeps the photoemission intensity (current) invariant because it is the *amount* of photoelectrons per unit time along the surface normal. The mirror operation, however, changes the photoelectron spin, as well as the circular polarization of light and the sample magnetization because they are axial vectors. The effect of this mirror operation on the polarization of light, sample magnetization, the electron spin as well as the photoelectron intensity is summarized in Tab. 5.2.

According to the symmetry properties listed in Tab. 5.2, the necessary relations with different light polarization, magnetization and photoelectron spin (σ, M, s) in order to keep the photoemission intensity $I_{s,M}^\sigma$ invariant can be given. For example, when we use the right-circularly-polarized incident light $+\sigma$ on the sample magnetization $+M$ and measured the spin-up $+s$ intensity as shown in Fig. 5.12a, the mirror operation m_{OP} will transform the whole system into the geometry in Fig. 5.12b with left-circularly-polarized light $+\sigma$, sample magnetization $-M$ and spin-down photoelectron $-s$, while keeping the number of photoelectrons I invariant. From the invariant intensities linked through this mirror transformation m_{OP} between geometries in Fig. 5.12a and Fig. 5.12b, we obtain

physical quantities	before mirroring m_{OP}	after mirroring m_{OP}
light polarization	$+\sigma$	$-\sigma$
sample magnetization	$+M$	$-M$
photoelectron spin	$+s$	$-s$
number of photoelectrons	I	I

Table 5.2: Quantities in the normal-emission photoemission experiments and their symmetry properties upon the mirror operation with respect to the optical plane (m_{OP}).

before mirroring m_{OP}		after mirroring m_{OP}		resultant relation	note		
$+\sigma$	$+M$	$+s$	$-\sigma$	$-M$	$-s$	$I_{+s,+M}^{+\sigma} = I_{-s,-M}^{-\sigma}$	Fig. 5.12c-d Fig. 5.12a-b
		$-s$		$+s$	$I_{-s,+M}^{+\sigma} = I_{+s,-M}^{-\sigma}$		
	$-M$	$+s$		$-s$	$I_{+s,-M}^{+\sigma} = I_{-s,+M}^{-\sigma}$		
		$-s$		$+s$	$I_{-s,-M}^{+\sigma} = I_{+s,+M}^{-\sigma}$		

Table 5.3: Relation between the eight spin-resolved partial intensities linked by the symmetry properties of the mirror operation with respect to the optical plane (m_{OP}), based on the symmetry property of experimental quantities in Tab. 5.2. The cases in the last two lines are illustrated in Fig. 5.12c-d and Fig. 5.12a-b.

a relation $I_{+s,+M}^{-\sigma} = I_{-s,-M}^{+\sigma}$. Similar situations are shown for the spin-resolved intensity in Fig. 5.12c and Fig. 5.12d and the result is $I_{-s,+M}^{-\sigma} = I_{+s,-M}^{+\sigma}$. The sum over spin-up and spin-down intensities gives us a relation $I_{+M}^{-\sigma} = I_{-M}^{+\sigma}$ between the spin-integrated intensity for the case of magnetization $+M$ and $-M$ as shown in Fig. 5.12e and Fig. 5.12f. The relations for all the eight spin-resolved partial intensities obtained through application of m_{OP} are listed in Tab. 5.3, in which the last two rows correspond to the cases in Fig. 5.12.

By using the mirror operation with respect to the optical plane m_{OP} , we can conceive that only four intensities from the total eight spin-resolved intensities ($I_{\pm s, \pm M}^{\pm \sigma}$) are independent, as listed in Tab. 5.3. This is strictly due to our experimental geometry where the sample magnetization and the high symmetry directions of sample surface are aligned in the optical plane, and the photoemission intensities are measured along the surface normal (Fig. 3.2). The reduced number of independent photoemission intensities has direct consequences on the photoelectron spin-polarization as well as for the magnetic dichroism which are derived from these intensities. The magnetic circular dichroism, for instance, is represented by the intensity asymmetry between the spin-integrated number of photoelectrons emitted from the sample with two opposite directions of magnetization $A = (I_{+M} - I_{-M}) / (I_{+M} + I_{-M})$ (Eq. 2.3), and these intensities ($I_{\pm M}$) are related to each other as illustrated in Fig. 5.12e-f as a result of the relation between partial intensities in Tab. 5.3.

For example, the number of photoelectrons are the same when we use right-circularly-polarized light on a $+M$ sample as with incident left-circularly-polarized light on a $-M$ sample ($I_{+M}^{-\sigma} = I_{-M}^{+\sigma}$, explicitly shown in Fig. 5.12e-f as a result of the sum over last two rows in Tab. 5.3). Similarly, we will also have the counterpart $I_{+M}^{+\sigma} = I_{-M}^{-\sigma}$, as a result of $I_{+s,+M}^{+\sigma} = I_{-s,-M}^{-\sigma}$ and $I_{-s,+M}^{+\sigma} = I_{+s,-M}^{-\sigma}$ from the first two rows in Tab. 5.3. These identities give rise to a relation between the magnetic dichroic signal obtained by the right- and left-circularly-polarized light ($A_{MCD}^{-\sigma}$ and $A_{MCD}^{+\sigma}$) as follows:

$$A_{MCD}^{-\sigma} = \frac{I_{+M}^{-\sigma} - I_{-M}^{-\sigma}}{I_{+M}^{-\sigma} + I_{-M}^{-\sigma}} = \frac{I_{-M}^{+\sigma} - I_{+M}^{+\sigma}}{I_{-M}^{+\sigma} + I_{+M}^{+\sigma}} = -A_{MCD}^{+\sigma} \quad (5.7)$$

For the second equality we use the identities in Tab. 5.3. The last equality follows directly from the definition of dichroic asymmetry (Eq. 2.3). The result in Eq. 5.7 indicates

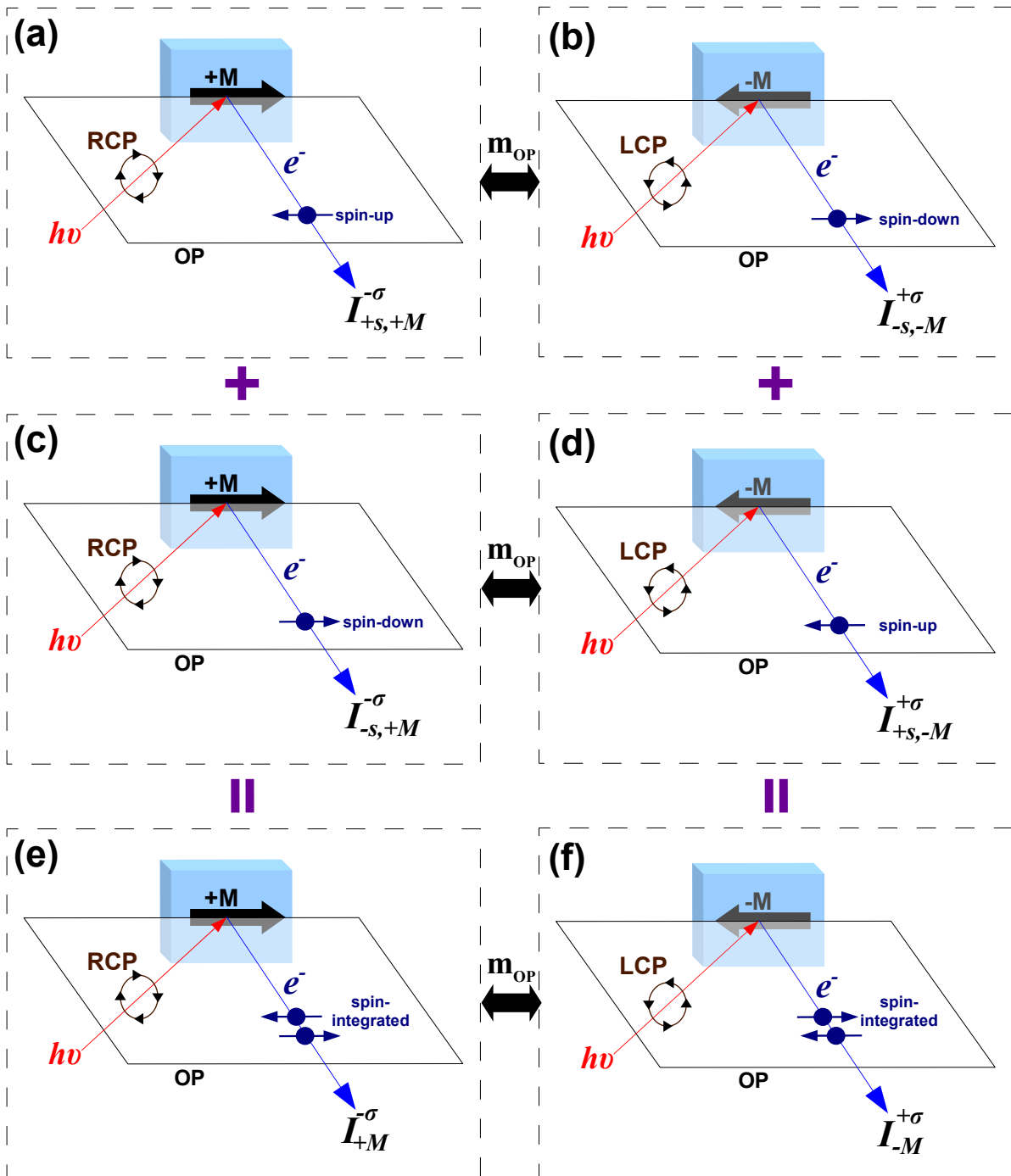


Figure 5.12: The symmetry pairs of spin-resolved photoemission intensities upon mirror operation (m_{OP}) on the optical plane (OP). (a) and (b) show the spin-up and down intensities emitted from a $+M$ sample, excited by a right- and left-circularly polarized light. They form a symmetry pair because a mirroring of geometry in (a) to the OP leads to geometry in (b). Likewise, (c) and (d) form a symmetry pair as well as (e) and (f). The spin-integrated intensity in (e) is simply the sum of (a) and (c), and (f) is the sum of (b) and (d).

derived quantity from $I_{\pm s, \pm M}^{\pm\sigma}$	relation lead by m_{OP}
magnetic circular dichroism	$A_{MCD}^{-\sigma} = -A_{MCD}^{+\sigma}$
photoelectron spin-polarization	$P_{+M}^{-\sigma} = -P_{-M}^{+\sigma} ; P_{-M}^{-\sigma} = -P_{+M}^{+\sigma}$
exchange spin-polarization	$P_{ex}^{-\sigma} = P_{ex}^{+\sigma}$
spin-orbit spin-polarization	$P_{so}^{-\sigma} = -P_{so}^{+\sigma}$

Table 5.4: Symmetry relations for magnetic dichroism and photoelectron spin-polarization. These are based on the partial intensities with relations in Tab. 5.3 linked by the mirror operation with respect to the optical plane (m_{OP}).

that the magnetic circular dichroic signal changes its sign when we switch from right- to left-circularly polarized light. This is satisfactorily fulfilled by our experimental magnetic dichroism shown in Fig. 4.2, Fig. 4.10 and Fig. 4.11 within an accuracy of 1%. More importantly, as a result of the reduced independent partial intensities in Tab. 5.3, symmetry relations also exist for the photoelectron spin-polarization ($P_{\pm M}^{\pm\sigma}$):

$$\begin{aligned}
P_{+M}^{-\sigma} &= \frac{I_{+s,+M}^{-\sigma} - I_{-s,+M}^{-\sigma}}{I_{+s,+M}^{-\sigma} + I_{-s,+M}^{-\sigma}} = \frac{I_{-s,-M}^{+\sigma} - I_{+s,-M}^{+\sigma}}{I_{-s,-M}^{+\sigma} + I_{+s,-M}^{+\sigma}} = -P_{-M}^{+\sigma} \\
P_{-M}^{-\sigma} &= \frac{I_{+s,-M}^{-\sigma} - I_{-s,-M}^{-\sigma}}{I_{+s,-M}^{-\sigma} + I_{-s,-M}^{-\sigma}} = \frac{I_{-s,+M}^{+\sigma} - I_{+s,+M}^{+\sigma}}{I_{-s,+M}^{+\sigma} + I_{+s,+M}^{+\sigma}} = -P_{+M}^{+\sigma}
\end{aligned} \tag{5.8}$$

Further consequences for the spin-polarization can be found, when we use the above relations to derive the spin-orbit- and exchange-polarization (P_{so} and P_{ex}) from Eq. 2.9 and Eq. 2.10 where the values of the spin-polarization measured from different directions of the sample magnetization are compared:

$$\begin{aligned}
P_{so}^{-\sigma} &= \frac{P_{+M}^{-\sigma} + P_{-M}^{-\sigma}}{2} = \frac{-P_{-M}^{+\sigma} - P_{+M}^{+\sigma}}{2} = -P_{so}^{+\sigma} \\
P_{ex}^{-\sigma} &= \frac{P_{+M}^{-\sigma} - P_{-M}^{-\sigma}}{2} = \frac{-P_{-M}^{+\sigma} + P_{+M}^{+\sigma}}{2} = P_{ex}^{+\sigma}
\end{aligned} \tag{5.9}$$

The above symmetry properties of magnetic circular dichroic signals and spin-polarization are summarized in Tab. 5.4. This indicates the relevant symmetry properties of the magnetic dichroism as well as of the photoelectron spin-polarization which we show in section 4.2 and section 4.4. The sign reversal for both the magnetic dichroic signal and spin-orbit spin-polarization upon reversal of the light helicity can be seen as a consequence of the symmetry of mirroring with respect to the optical plane m_{OP} , which is a symmetry plane of the sample in our case. According to the analytical and numerical calculations [65, 68], the mechanism responsible for this correspondence between dichroism and spin-polarization is the interference between photoexcitation channels.

The necessity to have both spin-orbit and exchange interaction in a magnetic dichroic valence band photoemission phenomena is understood as discussed in section 2.2 and section 5.2. The spin-orbit interaction provides a hybridization in the electronic structure, leading to an interference between photoexcitation channels, and exchange interaction gives rise to a macroscopic magnetization as a reference from the symmetry point of

view. This has been shown explicitly in section 5.2 in line with the theories as well as experiments reported in the literature [21, 65, 69, 70, 75, 76]. This interference between photoexcitation channels leads to an intensity change in the photoemission, and a constant contribution in the photoelectron spin-polarization with respect to the sample magnetization reversal [65, 68]. This constant contribution in the spin-polarization is defined phenomenologically in Eq. 2.10 as $P_{so}^{\pm\sigma}$ [93]. In contrast, the spin-polarization due to exchange interaction changes its sign as the magnetization changes ($P_{ex}^{\pm\sigma}$, Eq. 2.9). The definitions of $P_{so}^{\pm\sigma}$ and $P_{ex}^{\pm\sigma}$ are formulated by Henk [93] and are in accordance with the definitions in spin-polarized low-energy electron scattering [94], where the exchange and spin-orbit scattering asymmetries (A_{ex}, A_{so}) are also defined to represent the scattering potentials due to exchange and spin-orbit interactions [26, 205]. In addition to the issue whether the exchange scattering asymmetry can represent the sample magnetization [206], the scattering asymmetries and potentials are not explicitly involved in the photoemission as in the electron scattering experiments.

Our observations in Fig. 4.10 as well as in Fig. 4.11 show a dominating exchange spin-polarization ($P_{ex}^{\pm\sigma}$) over the spin-orbit spin-polarization ($P_{so}^{\pm\sigma}$). This result can be explained by the relatively weak spin-orbit coupling as compared to the exchange interaction in the valence band structure of cobalt within our energy range. The strength of spin-orbit coupling can be roughly estimated by the spin-orbit splitting ($\Delta E_{so} \approx 0.10$ eV around $0.4\overline{\Gamma X}$ between split Δ_1 bands [43, 47]) and compared to the exchange splitting ($\Delta E_{ex} \approx 1.5$ eV at Γ for both Δ_1 and Δ_5 bands [43, 47]). In magnetic dichroic experiments in core-level photoemission, a strong spin-orbit coupling is present with a weak apparent exchange splitting ($\Delta E_{so} \approx 13$ eV, $\Delta E_{ex}^{2p_{1/2}} \approx 0.3$ eV, $\Delta E_{ex}^{2p_{3/2}} \approx 0.5$ eV for Fe $2p$ levels [29]), leading to a size of spin-orbit spin-polarization P_{so} that is comparable to the exchange spin-polarization P_{ex} [66, 90–92].

The symmetry relations as well as the principles regarding the size of exchange and spin-orbit spin-polarization can also be applied to the magnetic linear dichroism. Then, we have to replace the circular polarization of light $\pm\sigma$ by the linear polarization $\pm\alpha$. The spin-orbit spin-polarization P_{so} in the linear dichroism is, however, below our experimental uncertainty of about 2% even though there is a dichroic signal of about 10% at $\alpha = 82^\circ$. Besides, we need to disentangle the small signal P_{so} from the weak but still detectable α dependence of the total spin-polarization as shown in Fig. 4.7b. The small signal of P_{so} is assigned to the small spin-orbit hybridization between the Δ_1 and Δ_5 electronic states in the quantum well states, as discussed in section 5.1.2 and section 5.2.

5.5 Photoemission intensity oscillations as a function of cobalt thickness

We observed oscillations in the photoemission intensity during the cobalt film growth as shown in Fig. 4.1. The period of the oscillation was assigned to have monolayer (ML) peri-

odicity in Fig. 5.13. This assignment is in agreement with the cobalt thickness estimation based on the calibrated evaporation rate as well as other information such as the onset of ferromagnetic signal in magnetic dichroism (Fig. 4.4), the quantum well state energy dispersion (section 5.1) and the characteristic initial double layer growth. As shown by the photoemission intensities at fixed final state energies in Fig. 5.13, the oscillations are detectable up to 5 ML and generally exist for all the measured energies (dashed lines). Moreover, the phase of oscillation in the two-photon photoemission (2PPE) energy range (b,c panels) is shifted by half of a monolayer from the oscillation in the three-photon photoemission (3PPE). This can be seen clearly by the peak positions, which locate at integer thickness in 3PPE (a) but half-integer thickness in 2PPE (b,c). The weak oscillation amplitude at 2 ML coincides with the initial bilayer growth mode of cobalt on Cu(001) [106, 108]. Similar oscillations are also observed in the work function as shown in Fig. 5.13d.

Since the oscillations exist for different energies, we exclude an origin from specific electronic states proposed by Eckstein *et al.* [207] as well as a surface stoichiometry change during film growth, which were used to interpret the photoemission intensity oscillation during growth of semiconductor compounds [208]. The variation of photoemission intensities due to variation in the sample work function can also be excluded, since it should give rise to an in-phase oscillation for all energies, hardly explaining the phase difference between 2PPE and 3PPE. Although the minimum of 2PPE intensities agree with the maximum of the work function at 2, 3 and 4 ML (Fig. 5.13d), the 3PPE shows an enhancement at those integer thicknesses. We relate our observation to the periodic change of densities of adatoms as well as step edges during the layer-by-layer growth of cobalt films on Cu(001) [106]. The adatom or step edge density can lead to additional momentum scattering events for the photoexcited electrons, which breaks the momentum conservation within the surface ($\Delta k_{\parallel} \neq 0$) and alters the photoelectron angular distribution. The momentum scattering can mediate additional photoexcited electrons to escape from the surface, which originally have energies higher than the vacuum level but are bound to the surface due to the energy-momentum conservation, leading to an enhanced photoemission intensity. At the same time, the scattering at adatoms or step edges contribute to a decrease of the lifetime of image potential (IP) states, resulting in a lower photoemission intensity in three-photon photoemission (3PPE) through IP states [35, 153]. A line width analysis of the 3PPE feature in Fig. 5.13a does not apparently resolve any oscillation. This can be due to the relatively small variation in the linewidth ($\delta_{\Delta E} \approx 0.07$ eV for Cu/Cu(001)[153]) compared to the line width we observed for the image potential states ($\Delta E \approx 0.3$ eV), which is below our experimental resolution.

Our observation reveals the sensitivity of two-photon photoemission to the surface morphology change. The mechanism could be the adatoms induced scattering of electrons on the surface [35, 153]. The periodic intensity change as a function of overlayer thickness can be used as a tool for monitoring the *in situ* layer-by-layer growth of thin films.

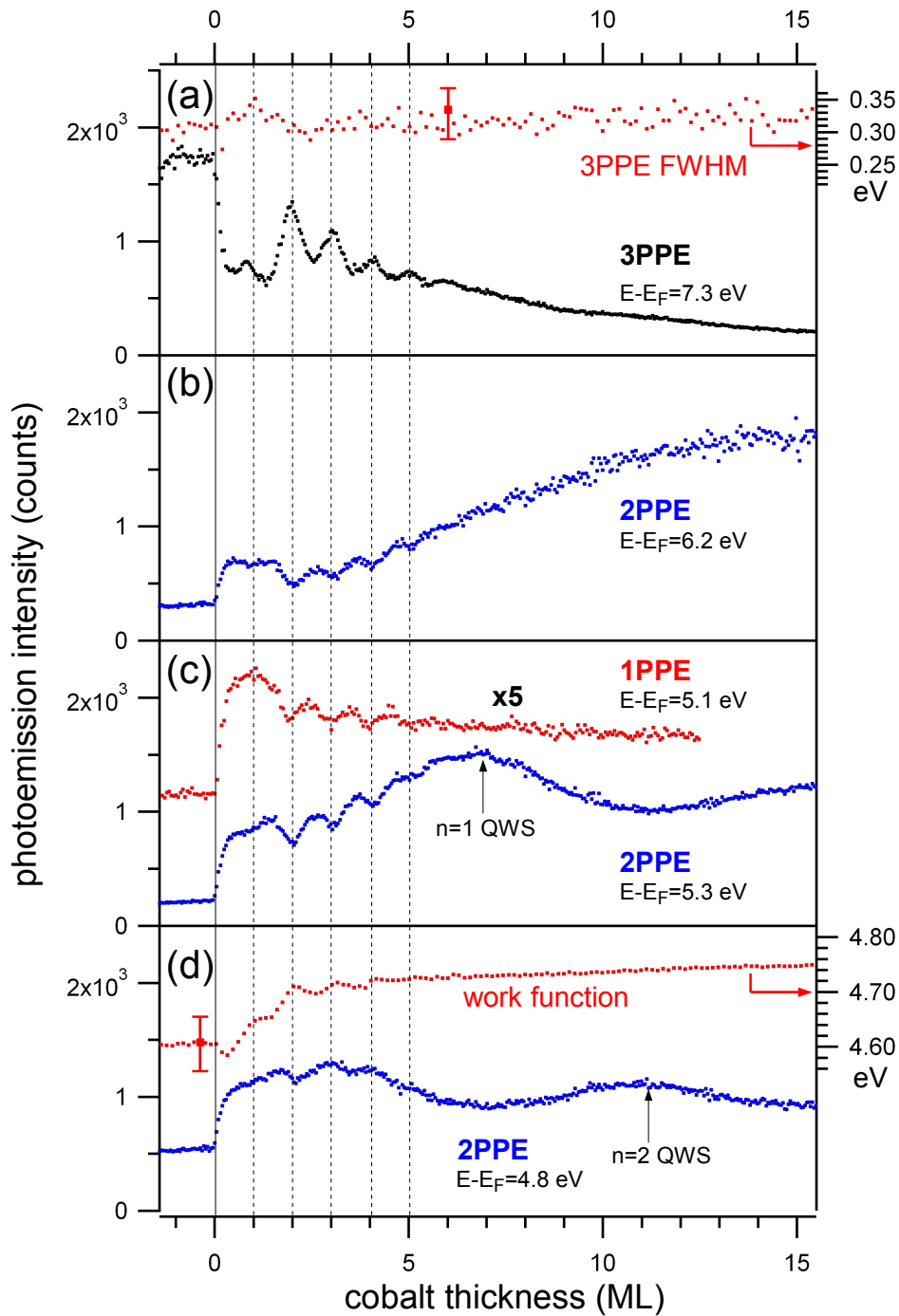


Figure 5.13: Photoemission intensity extracted from Fig. 4.1. Each curve displays the intensity averaged over a 0.2 eV window with central energy indicated. The one-, two- and three-photon photoemission (1PPE, 2PPE and 3PPE) processes are shown. In panel (a) the full-width-at-half-maximum (FWHM) of 3PPE feature is shown and in panel (d) the work function obtained from the low energy cutoff in Fig. 4.1 is displayed, with a 100 meV scale indicating the energy resolution. The features from the unoccupied quantum well states are indicated. For better comparison, the 1PPE intensity has been multiplied by factor of 5.

5.6 Information depth of two-photon photoemission

From the monolayer (ML) oscillations in the photoemission intensity (section 5.5), it is evident that the photoemission process is very surface sensitive. A probing depth of photoemission equal to 1 ML is certainly an overestimation of the surface sensitivity since the oscillation amplitude in Fig. 5.13 is at most only about one third of the total intensity. An estimation from the imaginary part of the wave vector ($\text{Im}k_{\perp}$) within the cobalt band gap at X gives a value of the final state decay length around 4.5 \AA at 6 eV above the Fermi level (section 5.3). Roughly the same value can be obtained from a totally different aspect, which is concerning the photoelectron mean free path limited by the absorption into unoccupied d -bands [201]. From our experiment, an upper bound of the probing depth in two-photon photoemission (2PPE) can be estimated by the thickness dependent magnetic dichroic signal as well as photoelectron spin-polarization as in Fig. 5.14. We estimate a value of around 20 \AA from the saturation of signals at cobalt thickness near 11 ML.

This interpretation of a cobalt thickness dependent dichroic signal and spin-polarization by a finite information depth in the photoemission can only be viewed as an estimation since the properties of cobalt films alter significantly within 5 ML, as also has been investigated by other photoemission studies [104, 133] as well as magneto-optical measurements [125]. Nevertheless, a less pronounced thickness dependence in the occupied electronic structure is observed in the one-photon photoemission data in Fig. 4.1b which shows no apparent change after 3 ML. A better quantitative estimation of photoemission probing depth from the data would require detailed information regarding the change of cobalt electronic structure, and a proper model which describes the decay mechanism of photoelectrons through cobalt layers. A possible mechanism, suitable for our low excitation energy (3 eV or 6 eV) and consequently low final state energy ($\approx 6 \text{ eV}$), is the electron-electron interaction, which could lead to the Stoner excitation and an energy loss of photoexcited electrons. The contribution of Stoner excitation has been shown to dominate in our energy region over the spin-wave scattering in theory [209], giving an inelastic mean free path for minority electrons in the range of 10-60 \AA at 6 eV above the Fermi level in a model cobalt system [209]. This value is comparable with the spin-integrated lifetime extracted from time-resolved two-photon photoemission measurements on cesiated cobalt films, with a value about 1 fs at 3 eV above the Fermi level and resulting an upper bound of the mean free path to be around 30 \AA [40]. The contribution from plasmon excitation is estimated from the "universal curve" [199, 210] and gives a value close to 30 \AA at 6 eV above the Fermi level.

To summarize, the probing depth of two-photon photoemission in our case with 3 eV photon energy is estimated to be around 20 \AA at 6 eV above the Fermi level by the cobalt thickness dependent dichroic signal and spin-polarization of photoelectrons. This value is comparable with the mean free path of photoelectrons when we consider the spin-dependent (spin-wave, Stoner excitation) or spin-independent (plasmon) scattering events

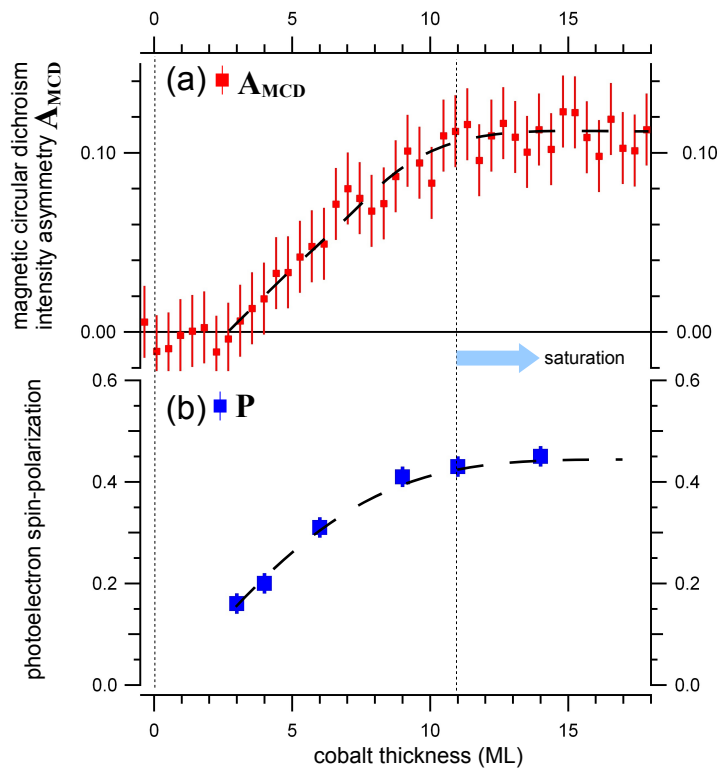


Figure 5.14: (a) Magnetic dichroic signal at $E = E_F + 6.1$ eV and (b) the spin polarization at $E = E_F + 6.2$ eV in two-photon photoemission from near the Fermi level, extracted from the data in Fig.4.4 and Fig.4.6. The vertical dashed lines at 11 ML indicates a saturation of detected signals. Dashed curves are guide to the eyes.

for the photoelectrons.

Chapter 6

Conclusion and outlook

In this work, we used spin-resolved linear and nonlinear photoemission to study electronic properties of ultrathin cobalt thin films grown on Cu(001) surfaces. For the first time, we could demonstrate magnetic dichroism from spectroscopically identified optically excited states, namely the unoccupied quantum well states in Co/Cu(001).

The cobalt majority unoccupied quantum well states are identified by comparing one- and two-photon photoemission. By the cobalt thickness dependent photoemission spectra, the dispersion of majority, unoccupied quantum well states is obtained, and the result is in agreement to an analytical model (phase-accumulation model) based on the bulk cobalt band structure as well as to recent numerical calculations [47]. The reversal of sample magnetization leads to pronounced photoemission intensity changes when circularly, or linearly polarized light that contains both p - and s -polarized components is used. Moreover, as revealed by the cobalt thickness dependence of the dichroic signal, the contribution from the unoccupied quantum well states in the dichroic signal is identified and is attributed to the spin-orbit coupling in the quantum well states, which leads to a mixing between electronic states with different spatial symmetry. This is also confirmed by light polarization-dependent measurements of photoemission intensity and magnetic dichroism.

The spin-resolved two-photon photoemission measurements directly identify the spin-character of relevant electronic states involved in the photoexcitation process. The majority unoccupied cobalt quantum well states and occupied cobalt d -bands are observed. By comparing with spin-resolved one-photon photoemission spectra, we clearly distinguish the significant spin-dependence in the two-photon photoemission process through intermediate majority quantum well states, resulting in an overall majority spin signal in the two-photon photoemission spectra. This majority spin signal strongly contrasts with the sign-changing spin-polarization in the one-photon photoemission. The negligible contribution from the occupied minority cobalt surface resonance state in two-photon photoemission is attributed to a reduced overlap with the minority quantum well states and a shorter lifetime of the minority quantum well states than the majority ones. The role of quantum well states to the spin-dependence of two-photon photoemission is further

checked by comparison of measurements on films grown at different temperatures. Moreover, the spin-polarization for opposite directions of sample magnetization is measured, which in principle helps to disentangle the contribution from exchange and spin-orbit interaction in the photoelectron spin-polarization. The overall spin-orbit spin-polarization is one order of magnitude smaller than the exchange spin-polarization and the small detectable spin-orbit part obeys the general symmetry relations within the accuracy of our experiments.

Besides the demonstration of magnetic dichroism from the unoccupied quantum well states and the spin-dependence in the two-photon photoemission process, this work identifies the relevant initial, intermediate and final states in two-photon photoemission from Co/Cu(001) with photon energy around 3 eV, which can provide a ground for further time-resolved two-photon photoemission measurements. Ideally, such measurements should provide the spin-dependent lifetimes and coherence time in and between the relevant electronic states. In addition, with 3 eV photon energy, nonlinear optical processes such as magnetic second harmonic generation can be studied, which has been demonstrated to depend sensitively on the electronic states involved [211–213]. The nonlinear optical investigations can be nicely combined with two-photon photoemission which helps to identify the electronic states and serves as an additional input for the simultaneously detected nonlinear optical signals, as has been demonstrated on Cu(001) surfaces [214].

Bibliography

- [1] R. Karplus and J. M. Luttinger. Hall effect in ferromagnetics. *Physical Review* **95**, 1154 (1954).
- [2] N. Nagaosa, J. Sinova, S. Onoda, A. H. MacDonald, and N. P. Ong. Anomalous Hall effect. *Review of Modern Physics* **82**, 1539 (2010).
- [3] H. Ebert. Magneto-optical effects in transition metal systems. *Reports on Progress in Physics* **59**, 1665 (1996).
- [4] P. M. Oppeneer. Magneto-optical Kerr spectra in *Handbook of Magnetic Materials, Vol. 13*. Editor: K. H. J. Buschow. North-Holland, Amsterdam (2001).
- [5] K. H. Bennemann. *Nonlinear Optics in Metals*. Clarendon Press, Oxford (1998).
- [6] B. Heinrich and J. F. Cochran. Ultrathin metallic magnetic films: magnetic anisotropies and exchange interactions. *Advances in Physics* **42**, 523 (1993).
- [7] M. T. Johnson, P. J. H. Bloemen, F. J. A. den Broeder, and J. J. de Vries. Magnetic anisotropy in metallic multilayers. *Reports on Progress in Physics* **59**, 1409 (1996).
- [8] C. A. F. Vaz, J. A. C. Bland, and G. Lauhoff. Magnetism in ultrathin film structures. *Reports on Progress in Physics* **71**, 056501 (2008).
- [9] D. Wang, R. Wu, and A. J. Freeman. State-tracking first-principles determination of magnetocrystalline anisotropy. *Physical Review Letters* **70**, 869 (1993).
- [10] J. Fabian and S. Das Sarma. Spin relaxation of conduction electrons in polyvalent metals: theory and a realistic calculation. *Physical Review Letters* **81**, 5624 (1998).
- [11] G. Y. Guo, S. Murakami, T.-W. Chen, and N. Nagaosa. Intrinsic spin Hall effect in platinum: first-principles calculations. *Physical Review Letters* **100**, 096401 (2008).
- [12] R. J. Elliott. Theory of the effect of spin-orbit coupling on magnetic resonance in some semiconductors. *Physical Review* **96**, 266 (1954).
- [13] J. L. Cheng, M. W. Wu, and J. Fabian. Theory of the spin relaxation of conduction electrons in silicon. *Physical Review Letters* **104**, 016601 (2010).
- [14] G. Y. Guo, Y. Yao, and Q. Niu. Ab initio calculation of the intrinsic spin Hall effect in semiconductors. *Physical Review Letters* **94**, 226601 (2005).
- [15] J. Walowski, G. Müller, M. Djordjevic, M. Münzenberg, M. Kläui, C. A. F. Vaz, and J. A. C. Bland. Energy equilibration processes of electrons, magnons, and phonons at the femtosecond time scale. *Physical Review Letters* **101**, 237401 (2008).
- [16] Kh. Zakeri, Y. Zhang, J. Prokop, T.-H. Chuang, N. Sakr, W. X. Tang, and J. Kirschner. Asymmetric spin-wave dispersion on Fe(110): direct evidence of the Dzyaloshinskii-Moriya interaction. *Physical Review Letters* **104**, 137203 (2010).
- [17] M. Hoesch, M. Muntwiler, V. N. Petrov, M. Hengsberger, L. Patthey, M. Shi, M. Falub, T. Greber, and J. Osterwalder. Spin structure of the Shockley surface state on Au(111). *Physical Review B* **69**, 241401 (2004).

- [18] H. Mirhosseini, J. Henk, A. Ernst, S. Ostanin, C.-T. Chiang, P. Yu, A. Winkelmann, and J. Kirschner. Unconventional spin topology in surface alloys with Rashba-type spin splitting. *Physical Review B* **79**, 245428 (2009).
- [19] M. Bode, M. Heide, K. von Bergmann, P. Ferriani, S. Heinze, G. Bihlmayer, A. Kubetzka, O. Pietzsch, S. Blgel, and R. Wiesendanger. Chiral magnetic order at surfaces driven by inversion asymmetry. *Nature* **447**, 190 (2007).
- [20] C. L. Gao, A. Ernst, A. Winkelmann, J. Henk, W. Wulfhekel, P. Bruno, and J. Kirschner. Non-collinear surface spin density by surface reconstruction in the alloy NiMn. *Physical Review Letters* **100**, 237203 (2008).
- [21] W. Kuch and C. M. Schneider. Magnetic dichroism in valence band photoemission. *Rep. Prog. Phys.* **64**, 147 (2001).
- [22] C. M. Schneider, M. S. Hammond, P. Schuster, A. Cebollada, R. Miranda, and J. Kirschner. Observation of magnetic circular dichroism in uv photoemission from ferromagnetic fcc cobalt films. *Physical Review B* **44**, 12066 (1991).
- [23] C. M. Schneider and J. Kirschner. Spin- and angle-resolved photoelectron spectroscopy from solid surfaces with circularly polarized light. *Critical Reviews in Solid State and Materials Sciences* **20**, 179 (1995).
- [24] D. T. Pierce and F. Meier. Photoemission of spin-polarized electrons from GaAs. *Physical Review B* **13**, 5484 (1976).
- [25] J. H. Dil. Spin and angle resolved photoemission on non-magnetic low-dimensional systems. *Journal of Physics: Condensed Matter* **21**, 403001 (2009).
- [26] R. Feder. *Polarized Electrons in Surface Physics*. World Scientific Publishing, Singapore (1985).
- [27] P. D. Johnson. Spin-polarized photoemission. *Reports on Progress in Physics* **60**, 1217 (1997).
- [28] G. Schütz, W. Wagner, W. Wilhelm, P. Kienle, R. Zeller, R. Frahm, and G. Materlik. Absorption of circularly polarized x rays in iron. *Physical Review Letters* **58**, 737 (1987).
- [29] L. Baumgarten, C. M. Schneider, H. Petersen, F. Schäfers, and J. Kirschner. Magnetic x-ray dichroism in core-level photoemission from ferromagnets. *Physical Review Letters* **65**, 492 (1990).
- [30] C. T. Chen, Y. U. Idzerda, H.-J. Lin, N. V. Smith, G. Meigs, E. Chaban, G. H. Ho, E. Pellegrin, and F. Sette. Experimental confirmation of the X-ray magnetic circular dichroism sum rules for iron and cobalt. *Physical Review Letters* **75**, 152 (1995).
- [31] B. T. Thole, P. Carra, F. Sette, and G. van der Laan. X-ray circular dichroism as a probe of orbital magnetization. *Physical Review Letters* **68**, 1943 (1992).
- [32] M. Donath. Spin-resolved inverse photoemission of ferromagnetic surfaces. *Applied Physics A: Materials Science & Processing* **49**, 351 (1989).
- [33] M. Donath. Spin-dependent electronic structure at magnetic surfaces: The low-Miller-index surfaces of nickel. *Surface Science Reports* **20**, 251 (1994).
- [34] H. Petek and S. Ogawa. Femtosecond time-resolved two-photon photoemission studies of electron dynamics in metals. *Progress in Surface Science* **56**, 239 (1997).
- [35] Th. Fauster, M. Weinelt, and U. Höfer. Quasi-elastic scattering of electrons in image-potential states. *Progress in Surface Science* **82**, 224 (2007).
- [36] M. Weinelt. Time-resolved two-photon photoemission from metal surfaces. *Journal of Physics: Condensed Matter* **14**, R1099 (2002).
- [37] M. Weinelt, A. B. Schmidt, M. Pickel, and M. Donath. Spin-polarized image-potential-state electrons as ultrafast magnetic sensors in front of ferromagnetic surfaces. *Progress in Surface Science* **82**, 388 (2007).

-
- [38] W. Wallauer and Th. Fauster. Exchange splitting of image states on Fe/Cu(100) and Co/Cu(100). *Physical Review B* **54**, 5086 (1996).
- [39] A. B. Schmidt, M. Pickel, M. Wiemhöfer, M. Donath, and M. Weinelt. Spin-dependent electron dynamics in front of a ferromagnetic surface. *Physical Review Letters* **95**, 107402 (2005).
- [40] M. Aeschlimann, M. Bauer, S. Pawlik, W. Weber, R. Burgermeister, D. Oberli, and H. C. Siegmann. Ultrafast spin-dependent electron dynamics in fcc Co. *Physical Review Letters* **79**, 5158 (1997).
- [41] O. Andreyev, Yu. M. Koroteev, M. Sánchez Albaneda, M. Cinchetti, G. Bihlmayer, E. V. Chulkov, J. Lange, F. Steeb, M. Bauer, P. M. Echenique, S. Blügel, and M. Aeschlimann. Spin-resolved two-photon photoemission study of the surface resonance state on Co/Cu(001). *Physical Review B* **74**, 195416 (2006).
- [43] M. Pickel, A. B. Schmidt, F. Giesen, J. Braun, J. Minar, H. Ebert, M. Donath, and M. Weinelt. Spin-orbit hybridization points in the face-centered-cubic cobalt band structure. *Physical Review Letters* **101**, 066402 (2008).
- [42] M. Pickel, A. B. Schmidt, M. Weinelt, and M. Donath. Magnetic exchange splitting in Fe above the Curie temperature. *Physical Review Letters* **104**, 237204 (2010).
- [44] K. Hild, J. Maul, G. Schönhense, H. J. Elmers, M. Amft, and P. M. Oppeneer. Magnetic circular dichroism in two-photon photoemission. *Physical Review Letters* **102**, 057207 (2009).
- [45] T. Nakagawa, I. Yamamoto, Y. Takagi, K. Watanabe, Y. Matsumoto, and T. Yokoyama. Two-photon photoemission magnetic circular dichroism and its energy dependence. *Physical Review B* **79**, 172404 (2009).
- [46] C.-T. Chiang, A. Winkelmann, P. Yu, and J. Kirschner. Magnetic dichroism from optically excited quantum well states. *Physical Review Letters* **103**, 077601 (2009).
- [47] C.-T. Chiang, A. Winkelmann, P. Yu, J. Kirschner, and J. Henk. Spin-orbit coupling in unoccupied quantum well states: experiment and theory for Co/Cu(001). *Physical Review B* **81**, 115130 (2010).
- [49] R. Courths and S. Hüfner. Photoemission experiments on Copper. *Physics Reports* **112**, 53 (1984).
- [50] B. Feuerbacher and R. F. Willis. Photoemission and electron states at clean surfaces. *Journal of Physics C: Solid State Physics* **9**, 169 (1976).
- [48] F. Reinert and S. Hüfner. Photoemission spectroscopy - from early days to recent applications. *New Journal of Physics* **7**, 97 (2005).
- [51] C. La-O-Vorakiat, M. Siemens, M. M. Murnane, H. C. Kapteyn, S. Mathias, M. Aeschlimann, P. Grychtol, R. Adam, C. M. Schneider, J. M. Shaw, H. Nembach, and T. J. Silva. Ultrafast demagnetization dynamics at the M edges of magnetic elements observed using a tabletop high-harmonic soft X-ray source. *Physical Review Letters* **103**, 257402 (2009).
- [52] A. L. Cavalieri, N. Müller, Th. Uphues, V. S. Yakovlev, A. Baltuska, B. Horvath, B. Schmidt, L. Blümel, R. Holzwarth, S. Hendel, M. Drescher, U. Kleineberg, P. M. Echenique, R. Kienberger, F. Krausz, and U. Heinzmann. Attosecond spectroscopy in condensed matter. *Nature* **449**, 1029 (2007).
- [53] G. Liu, G. Wang, Y. Zhu, H. Zhang, G. Zhang, X. Wang, Y. Zhou, W. Zhang, H. Liu, L. Zhao, J. Meng, X. Dong, C. Chen, Z. Xu, and X. J. Zhou. Development of a vacuum ultraviolet laser-based angle-resolved photoemission system with a superhigh energy resolution better than 1 meV. *Review of Scientific Instruments* **79**, 023105 (2008).
- [54] B. Krömker, M. Escher, D. Funnemann, D. Hartung, H. Engelhard, and J. Kirschner. Development of a momentum microscope for time resolved band structure imaging. *Review of Scientific Instruments* **79**, 053702 (2008).
- [55] H. Ueba and B. Gumhalter. Theory of two-photon photoemission spectroscopy of surfaces. *Progress in Surface Science* **82**, 193 (2007).

- [56] W. Eberhardt and F. J. Himpsel. Dipole selection rules for optical transitions in the fcc and bcc lattices. *Physical Review B* **21**, 5572 (1980).
- [57] J. Hermanson. Final-state symmetry and polarization effects in angle-resolved photoemission spectroscopy. *Solid State Communications* **22**, 9 (1977).
- [58] M. Hoesch, T. Greber, V. N. Petrov, M. Muntwiler, M. Hengsberger, W. Auwarter, and J. Osterwalder. Spin-polarized Fermi surface mapping. *Journal of Electron Spectroscopy and Related Phenomena* **124**, 263 (2002).
- [59] T. C. Chiang, J. A. Knapp, M. Aono, and D. E. Eastman. Angle-resolved photoemission, valence-band dispersions $E(\vec{k})$, and electron and hole lifetimes for GaAs. *Physical Review B* **21**, 3513 (1980).
- [60] P. Heimann, H. Miosga, and H. Neddermeyer. Photoemission from Au single-crystals. Location of transitions in k space along lines of high symmetry. *Solid State Communications* **29**, 463 (1979).
- [61] M. Wolf, A. Hotzel, E. Knoesel, and D. Velic. Direct and indirect excitation mechanisms in two-photon photoemission spectroscopy of Cu(111) and CO/Cu(111). *Physical Review B* **59**, 5926 (1999).
- [62] W. Schattke, E. E. Krasovskii, R. Díez Muiño, and P. M. Echenique. Direct resolution of unoccupied states in solids via two-photon photoemission. *Physical Review B* **78**, 155314 (2008).
- [63] A. Winkelmann, W.-C. Lin, C.-T. Chiang, F. Bisio, H. Petek, and J. Kirschner. Resonant coherent three-photon photoemission from Cu(001). *Physical Review B* **80**, 155128 (2009).
- [64] W. Wallauer and Th. Fauster. Two-photon excitation processes and linewidths of surface and image states on Cu(111). *Surface Science* **374**, 44 (1997).
- [65] J. Henk, T. Scheunemann, S. V. Halilov, and R. Feder. Magnetic dichroism and electron spin polarization in photoemission: analytical results. *Journal of Physics: Condensed Matter* **8**, 47 (1996).
- [66] Ch. Roth, F. U. Hillebrecht, H. Rose, and E. Kisker. Linear magnetic dichroism in angular resolved Fe 3p core level photoemission. *Physical Review Letters* **70**, 3479 (1993).
- [67] C. M. Schneider and G. Schönhense. Investigating surface magnetism by means of photoexcitation electron emission microscopy. *Reports on Progress in Physics* **65**, R1785 (2002).
- [68] J. Henk and R. Feder. Magnetic circular dichroism in photoemission by linear polarized light. *Physical Review B* **55**, 11476 (1997).
- [69] W. Kuch, M.-T. Lin, W. Steinhögl, C. M. Schneider, D. Venus, and J. Kirschner. Angle-resolved study of magnetic dichroism in photoemission using linearly polarized light. *Physical Review B* **51**, 609 (1995).
- [70] A. Rampe, D. Hartmann, and G. Güntherodt. Linear magnetic dichroism in angle-resolved photoemission spectroscopy from Co(0001) and Fe(110) valence bands in *Spin-Orbit Influenced Spectroscopies of Magnetic Solids*. Editor: H. Ebert and G. Schütz. Springer-Verlag, Berlin (1996).
- [71] E. Merzbacher. *Quantum Mechanics*. John-Wiley and Sons, Inc., New York 3 edition (1998).
- [72] L. M. Falicov and J. Ruvalds. Symmetry of the wave functions in the band theory of ferromagnetic metals. *Physical Review* **172**, 498 (1968).
- [73] C. J. Bradley and A. P. Cracknell. *The Mathematical Theory of Symmetry in Solids*. Clarendon press, Oxford (1972).
- [74] A. Rampe. *Spin-Bahn-Kopplung und zweidimensionale Zustände in ultradünnen, magnetischen Schichten*. PhD thesis Technischen Hochschule Aachen (1999).
- [75] D. Venus. Interrelation of magnetic-dichroism effects seen in the angular distribution of photoelectrons from surfaces. *Physical Review B* **49**, 8821 (1994).

- [76] R. Schellenberg, H. Meinert, A. Perez, and E. Kisker. Symmetry rules in magnetic core-level photoelectron spectroscopy from epitaxial ferromagnetic ultrathin films. *Physical Review B* **64**, 104427 (2001).
- [77] C. M. Schneider, U. Pracht, W. Kuch, A. Chassé, and J. Kirschner. Magnetic dichroism in photoemission as a spin-resolving probe for electronic correlations. *Physical Review B* **54**, R15618 (1996).
- [78] R. M. A. Azzam and N. M. Bashara. *Ellipsometry and Polarized Light*. North-Holland, Amsterdam (1992).
- [79] J. Kessler. *Polarized Electrons*. Springer-Verlag, Berlin (1985).
- [80] E. Kisker, K. Schröder, M. Campagna, and W. Gudat. Temperature dependence of the exchange splitting of Fe by spin-resolved photoemission spectroscopy with synchrotron radiation. *Physical Review Letters* **52**, 2285 (1984).
- [81] C. M. Schneider, P. Schuster, M. S. Hammond, and J. Kirschner. Spin-polarized photoemission from f.c.c.-cobalt above the curie temperature: evidence of short-range magnetic order. *Europhysics Letters* **16**, 689 (1991).
- [82] R. Raue, H. Hopster, and R. Clauberg. Observation of spin-split electronic states in solids by energy-, angle-, and spin-resolved photoemission. *Physical Review Letters* **50**, 1623 (1983).
- [83] H. Hopster, R. Raue, G. Güntherodt, E. Kisker, R. Clauberg, and M. Campagna. Temperature dependence of the exchange splitting in Ni studied by spin-polarized photoemission. *Physical Review Letters* **51**, 829 (1983).
- [84] W. Eberhardt, E. W. Plummer, K. Horn, and J. Erskine. Magnetic exchange splitting of electronic surface states on Ni(110). *Physical Review Letters* **45**, 273 (1980).
- [85] G. Busch, M. Campagna, P. Cotti, and H. Ch. Siegmann. Observation of electron polarization in photoemission. *Physical Review Letters* **22**, 597 (1969).
- [86] U. Bänninger, G. Busch, M. Campagna, and H. C. Siegmann. Photoelectron spin polarization and ferromagnetism of crystalline and amorphous nickel. *Physical Review Letters* **25**, 585 (1970).
- [87] M. Stampanoni, A. Vaterlaus, M. Aeschlimann, and F. Meier. Magnetism of epitaxial bcc iron on Ag(001) observed by spin-polarized photoemission. *Physical Review Letters* **59**, 2483 (1987).
- [88] G. A. Mulhollan, K. Garrison, and J. L. Erskine. Surface magnetism of Gd(0001): evidence of ferromagnetic coupling to bulk. *Physical Review Letters* **69**, 3240 (1992).
- [89] B. T. Jonker, K. H. Walker, E. Kisker, G. A. Prinz, and C. Carbone. Spin-polarized photoemission study of epitaxial Fe(001) films on Ag(001). *Physical Review Letters* **57**, 142 (1986).
- [90] F. U. Hillebrecht, Ch. Roth, H. B. Rose, W. G. Park, E. Kisker, and N. A. Cherepkov. Magnetic linear dichroism in spin-resolved Fe 2*p* photoemission. *Physical Review B* **53**, 12182 (1996).
- [91] F. U. Hillebrecht, Ch. Roth, H. B. Rose, M. Finazzi, and L. Braicovich. Circular magnetic dichroism in spin-resolved Fe 3*p* photoemission. *Physical Review B* **51**, 9333 (1995).
- [92] C. De Nadaï, G. van der Laan, S. S. Dhesi, and N. B. Brookes. Spin-polarized magnetic circular dichroism in Ni 2*p* core-level photoemission. *Physical Review B* **68**, 212401 (2003).
- [93] J. Henk. Temperature-dependent electronic structure, spin-resolved photoemission, and magnetic dichroism of ultrathin ferromagnetic films: Co/Cu(001). *Journal of Physics: Condensed Matter* **13**, 833 (2001).
- [94] D. Venus and H. L. Johnston. Exchange and spin-orbit contributions to spin-polarized LEED rotation curves of magnetic films: Fe/W(001). *Physical Review B* **50**, 15787 (1994).
- [96] T. C. Chiang. Photoemission studies of quantum well states in thin films. *Surface Science Reports* **39**, 181 (2000).

- [95] R. Dingle, W. Wiegmann, and C. H. Henry. Quantum states of confined carriers in very thin $Al_xGa_{1-x}As$ -GaAs- $Al_xGa_{1-x}As$ heterostructures. *Physical Review Letters* **33**, 827 (1974).
- [97] R. M. Kolbas and Jr. N. Holonyak. Man-made quantum wells: a new perspective on the finite square-well problem. *American Journal of Physics* **52**, 431 (1984).
- [99] N. V. Smith, N. B. Brookes, Y. Chang, and P. D. Johnson. Quantum-well and tight-binding analyses of spin-polarized photoemission from Ag/Fe(001) overlayers. *Physical Review B* **49**, 332 (1994).
- [98] N. V. Smith. Phase analysis of image states and surface states associated with nearly-free-electron band gaps. *Physical Review B* **32**, 3549 (1985).
- [101] Y. Z. Wu, A. K. Schmid, M. S. Altman, X. F. Jin, and Z. Q. Qiu. Spin-dependent Fabry-Pérot interference from a Cu thin film grown on fcc Co(001). *Physical Review Letters* **94**, 027201 (2005).
- [100] J. J. Paggel, T. Miller, and T.-C. Chiang. Quantum-well states as Fabry-Pérot modes in a thin-film electron interferometer. *Science* **283**, 1709 (1999).
- [102] P.M. Echenique and J. B. Pendry. Theory of image states at metal surfaces. *Progress in Surface Science* **32**, 111 (1989).
- [103] T. Niizeki, N. Tezuka, and K. Inomata. Enhanced tunnel magnetoresistance due to spin dependent quantum well resonance in specific symmetry states of an ultrathin ferromagnetic electrode. *Physical Review Letters* **100**, 047207 (2008).
- [104] A. B. Schmidt, M. Pickel, T. Allmers, M. Budke, J. Braun, M. Weinelt, and M. Donath. Surface electronic structure of fcc Co films: a combined spin-resolved one- and two-photon-photoemission study. *Journal of Physics D: Applied Physics* **41**, 164003 (2008).
- [105] H. Eckardt, L. Fritsche, and J. Noffke. Self-consistent relativistic band structure of the noble metals. *Journal of Physics F: Metal Physics* **14**, 97 (1984).
- [106] A. K. Schmid and J. Kirschner. In situ observation of epitaxy growth of Co thin films on Cu(001). *Ultramicroscopy* **42-44**, 483 (1992).
- [107] J., R. Allenspach, and U. Drig. Intermixing and growth kinetics of the first Co monolayers on Cu(001). *Surface Science* **383**, L742 (1997).
- [114] G. J. Mankey, M. T. Kief, and R. F. Willis. The effect of microstructure on the magnetic behavior of epitaxial cobalt layers. *Journal of Vacuum Science and Technology A* **9**, (3) 1595-1598 (1991).
- [117] T. Bernhard, R. Pfandzelter, M. Gruyters, and H. Winter. Temperature-dependent intermixing of ultrathin Co films grown on Cu(001). *Surface Science* **575**, 154 (2005).
- [113] M. T. Kief and W. F. Egelhoff. Growth and structure of Fe and Co thin films on Cu(111), Cu(100), and Cu(110): A comprehensive study of metastable film growth. *Physical Review B* **47**, 10785 (1993).
- [108] E. Navas, P. Schuster, C. M. Schneider, J. Kirschner, A. Cebollada, C. Ocal, R. Miranda, J. Cerdá, and P. de Andrés. Crystallography of epitaxial face centered tetragonal Co/Cu(100) by low energy electron diffraction. *Journal of Magnetism and Magnetic Materials* **121**, 65 (1993).
- [109] J. R. Cerdá, P. L. de Andres, A. Cebollada, R. Miranda, E. Navas, P. Schuster, C. M. Schneider, and J. Kirschner. Epitaxial growth of cobalt films on Cu(100): a crystallographic LEED determination. *Journal of Physics: Condensed Matter* **5**, 2055 (1993).
- [110] M. Maglietta, E. Zanazzi, F. Jona, D. W. Jepsen, and P. M. Marcus. LEED structure analysis of a Co001 surface. *Applied Physics A: Materials Science & Processing* **15**, 409 (1978).
- [111] A. Clarke, G. Jennings, R. F. Willis, P. J. Rous, and J. B. Pendry. A LEED determination of the structure of cobalt overlayers grown on a single-crystal Cu(001) substrate. *Surface Science* **187**, 327 (1987).

- [112] J.J. de Miguel, A. Cebollada, J.M. Gallego, S. Ferrer, R. Miranda, C. M. Schneider, P. Bressler, J. Garbe, K. Bethke, and J. Kirschner. Characterization of the growth processes and magnetic properties of thin ferromagnetic cobalt films on Cu(100). *Surface Science* **211-212**, 732 (1989).
- [115] W. Schindler, Th. Koop, A. Kazimirov, G. Scherb, J. Zegenhagen, Th. Schultz, R. Feidenhans'l, and J. Kirschner. Non-coherent growth patches in pseudomorphic films: unusual strain relief in electrodeposited Co on Cu(001). *Surface Science* **465**, L783 (2000).
- [116] W. Weber, A. Bischof, R. Allenspach, C. H. Back, J. Fassbender, U. May, B. Schirmer, R. M. Jungblut, G. Güntherodt, and B. Hillebrands. Structural relaxation and magnetic anisotropy in Co/Cu(001) films. *Physical Review B* **54**, 4075 (1996).
- [118] O. Heckmann, H. Magnan, P. le Fevre, D. Chandesris, and J. J. Rehr. Crystallographic structure of cobalt films on Cu(001): elastic deformation to a tetragonal structure. *Surface Science* **312**, 62 (1994).
- [119] M. B. Stearns. Fe, Co, Ni in *Landolt-Börnstein Zahlenwerte und Funktionen aus Naturwissenschaften und Technik: Neue Serie*. Editor: O. Madelung. Springer-Verlag, Berlin (1986).
- [120] J. Donohue. *The Structure of the Elements*. J. Wiley & Sons Ltd., New York (1974).
- [121] N. W. Ashcroft and N. D. Mermin. *Solid State Physics*. Saunders College Publ., Philadelphia (1976).
- [122] Q. Y. Jin, H. Regensburger, R. Vollmer, and J. Kirschner. Periodic oscillations of the surface magnetization during the growth of Co films on Cu(001). *Physical Review Letters* **80**, 4056 (1998).
- [123] O. Mironets, H. L. Meyerheim, C. Tusche, V. S. Stepanyuk, E. Soyka, P. Zschack, H. Hong, N. Jeutter, R. Felici, and J. Kirschner. Direct evidence for mesoscopic relaxations in cobalt nanoislands on Cu(001). *Physical Review Letters* **100**, 096103 (2008).
- [124] A. K. Schmid, D. Atlan, H. Itoh, B. Heinrich, T. Ichinokawa, and J. Kirschner. Fast interdiffusion in thin films: scanning-tunneling-microscopy determination of surface diffusion through microscopic pinholes. *Physical Review B* **48**, 285 (1993).
- [125] C. M. Schneider, P. Bressler, P. Schuster, J. Kirschner, J. J. de Miguel, and R. Miranda. Curie temperature of ultrathin films of fcc-cobalt epitaxially grown on atomically flat Cu(100) surfaces. *Physical Review Letters* **64**, 1059 (1990).
- [126] R. Vollmer, M. Etzkorn, P. S. Anil Kumar, H. Ibach, and J. Kirschner. Spin-polarized electron energy loss spectroscopy of high energy, large wave vector spin waves in ultrathin fcc Co films on Cu(001). *Physical Review Letters* **91**, 147201 (2003).
- [127] H. P. Oepen, M. Benning, C. M. Schneider, and J. Kirschner. Magnetic domain structure in ultrathin ferromagnetic films. *Vacuum* **41**, 489 (1990).
- [128] M. Kowalewski, C. M. Schneider, and B. Heinrich. Thickness and temperature dependence of magnetic anisotropies in ultrathin fcc Co(001) structures. *Physical Review B* **47**, 8748 (1993).
- [129] P. Krams, F. Lauks, R. L. Stamps, B. Hillebrands, and G. Güntherodt. Magnetic anisotropies of ultrathin Co(001) films on Cu(001). *Physical Review Letters* **69**, 3674 (1992).
- [130] K. Miyamoto, K. Iori, K. Sakamoto, H. Narita, A. Kimura, M. Taniguchi, S. Qiao, K. Hasegawa, K. Shimada, H. Namatame, and S. Blügel. Spin polarized *d* surface resonance state of fcc Co/Cu(001). *New Journal of Physics* **10**, 125032 (2008).
- [133] C. M. Schneider, J. J. de Miguel, P. Bressler, P. Schuster, R. Miranda, and J. Kirschner. Spin- and angle-resolved photoemission from single crystals and epitaxial films using circularly polarized synchrotron radiation. *Journal of Electron Spectroscopy and Related Phenomena* **51**, 263 (1990).
- [131] K. Miyamoto, K. Iori, K. Sakamoto, A. Kimura, S. Q. K. Shimada, H. Namatame, and M. Taniguchi. Spin-dependent electronic band structure of Co/Cu(001) with different thicknesses. *Journal of Physics: Condensed Matter* **20**, 225001 (2008).

- [132] D. Venus, W. Kuch, M.-T. Lin, C. M. Schneider, H. Ebert, and J. Kirschner. Magnetic dichroism in UV photoemission at off-normal emission: Study of the valence bands. *Physical Review B* **55**, 2594 (1997).
- [134] A. Fanelisa, E. Kisker, J. Henk, and R. Feder. Magnetic dichroism in valence-band photoemission from Co/Cu(001): experiment and theory. *Physical Review B* **54**, 2922 (1996).
- [135] D. H. Yu, M. Donath, J. Braun, and G. Rangelov. Spin-polarized unoccupied quantum-well states in ultrathin Co films on Cu(100). *Physical Review B* **68**, 155415 (2003).
- [136] J. E. Ortega, F. J. Himpsel, G. J. Mankey, and R. F. Willis. Quantum-well states and magnetic coupling between ferromagnets through a noble-metal layer. *Physical Review B* **47**, 1540 (1993).
- [137] C. M. Schneider, P. Schuster, M. S. Hammond, H. Ebert, J. Noffke, and J. Kirschner. Spin-resolved electronic bands of FCT cobalt. *Journal of Physics: Condensed Matter* **3**, 4349 (1991).
- [138] J.-C. Diels and W. Rudolph. *Ultrashort Laser Pulse Phenomena*. Academic Press, Amsterdam (2006).
- [139] A. Winkelmann, W.-C. Lin, F. Bisio, H. Petek, and J. Kirschner. Interferometric control of spin-polarized electron populations at a metal surface observed by multiphoton photoemission. *Physical Review Letters* **100**, 206601 (2008).
- [140] M. Hengsberger, F. Baumberger, H. J. Neff, T. Greber, and J. Osterwalder. Photoemission momentum mapping and wave function analysis of surface and bulk states on flat Cu(111) and stepped Cu(443) surfaces: A two-photon photoemission study. *Physical Review B* **77**, 085425 (2008).
- [141] N. F. Mott. The scattering of fast electrons by atomic nuclei. *Proceedings of the Royal Society of London. Series A* **124**, 425 (1929).
- [142] D.T. Pierce, R.J. Celotta, M.H. Kelley, and J. Unguris. Electron spin polarization analyzers for use with synchrotron radiation. *Nuclear Instruments and Methods in Physics Research Section A: Accelerators, Spectrometers, Detectors and Associated Equipment* **266**, 550 (1988).
- [143] J. Kirschner and R. Feder. Spin polarization in double diffraction of low-energy electrons from W(001): experiment and theory. *Physical Review Letters* **42**, 1008 (1979).
- [144] J. Sawler and D. Venus. Electron polarimeter based on spin-polarized low-energy electron diffraction. *Review of Scientific Instruments* **62**, 2409–2418 (1991).
- [145] D. Yu, C. Math, M. Meier, M. Escher, G. Rangelov, and M. Donath. Characterisation and application of a SPLEED-based spin polarisation analyser. *Surface Science* **601**, 5803 (2007).
- [146] D. Tillmann, R. Thiel, and E. Kisker. Very-low-energy spin-polarized electron diffraction from Fe(001). *Zeitschrift für Physik B Condensed Matter* **77**, 1 (1989).
- [147] Th. Dodt, D. Tillmann, R. Rochow, and E. Kisker. Spin and energy dependence of the electron current absorbed by α -Fe(001) Thin Films. *Europhysics Letters* **6**, 375 (1988).
- [148] F. U. Hillebrecht, R. M. Jungblut, L. Wiebusch, Ch. Roth, H. B. Rose, D. Knabben, C. Bethke, N. B. Weber, St. Manderla, U. Rosowski, and E. Kisker. High-efficiency spin polarimetry by very-low-energy electron scattering from Fe(100) for spin-resolved photoemission. *Review of Scientific Instruments* **73**, 1229 (2002).
- [149] R. Bertacco and F. Ciccacci. Oxygen-induced enhancement of the spin-dependent effects in electron spectroscopies of Fe(001). *Physical Review B* **59**, 4207 (1999).
- [150] R. Bertacco, D. Onofrio, and F. Ciccacci. A novel electron spin-polarization detector with very large analyzing power. *Review of Scientific Instruments* **70**, 3572 (1999).
- [151] T. Okuda, Y. Takeichi, Y. Maeda, A. Harasawa, I. Matsuda, T. Kinoshita, and A. Kakizaki. A new spin-polarized photoemission spectrometer with very high efficiency and energy resolution. *Review of Scientific Instruments* **79**, 123117 (2008).

- [152] A. Winkelmann, D. Hartung, H. Engelhard, C.-T. Chiang, and J. Kirschner. High efficiency electron spin polarization analyzer based on exchange scattering at Fe/W(001). *Review of Scientific Instruments* **79**, 083303 (2008).
- [153] M. Weinelt, C. Reuss, M. Kutschera, U. Thomann, I.L. Shumay, T. Fauster, U. Hfer, F. Theilmann, and A. Goldmann. Decay and dephasing of image-potential states due to surface defects and disorder. *Applied Physics B: Lasers & Optics* **68**, 377 (1999).
- [154] J. Reif, C. Rau, and E. Matthias. Influence of magnetism on second harmonic generation. *Physical Review Letters* **71**, 1931 (1993).
- [155] F. Bisio, M. Nývlt, J. Franta, H. Petek, and J. Kirschner. Mechanisms of high-order perturbative photoemission from Cu(001). *Physical Review Letters* **96**, 087601 (2006).
- [156] J. N. Eckstein, C. Webb, S.-L. Weng, and K. A. Bertness. Photoemission oscillations during epitaxial growth. *Applied Physics Letters* **51**, 1833 (1987).
- [157] A. Laamouri, M. Djafari Rouhani, A. M. Gue, N. Fazouan, and D. Esteve. Photoemission applied to the in situ study of epitaxial growth: theoretical modelling. *Surface and Interface Analysis* **18**, 505 (1992).
- [158] T. Nakagawa and T. Yokoyama. Magnetic circular dichroism near the Fermi level. *Physical Review Letters* **96**, 237402 (2006).
- [159] M. Pickel. *Image-potential states as a sensor for magnetism*. PhD thesis in Freien Universität Berlin (2007).
- [160] K. Meinel, A. Beckmann, M. Klaua, and H. Bethge. The dependence of quantum-well features in photoemission on film quality. *physica status solidi (a)* **150**, 521 (1995).
- [161] D.-A. Luh, C.-M. Cheng, C.-T. Tsai, K.-D. Tsuei, and J.-M. Tang. Transition from disorder to order in thin metallic films studied with angle-resolved photoelectron spectroscopy. *Physical Review Letters* **100**, 027603 (2008).
- [162] D. A. Evans, M. Alonso, R. Cimino, and K. Horn. Observation of quantum size effects in photoemission from Ag islands on GaAs(110). *Physical Review Letters* **70**, 3483 (1993).
- [163] S. Passlack, S. Mathias, O. Andreyev, D. Mittnacht, M. Aeschlimann, and M. Bauer. Space charge effects in photoemission with a low repetition, high intensity femtosecond laser source. *Journal of Applied Physics* **100**, 024912 (2006).
- [164] S. Hellmann, K. Rossnagel, M. Marczyński-Bühlow, and L. Kipp. Vacuum space-charge effects in solid-state photoemission. *Physical Review B* **79**, 035402 (2009).
- [165] X. J. Zhou, B. Wannberg, W. L. Yang, V. Brouet, Z. Sun, J. F. Douglas, D. Dessau, Z. Hussain, and Z. X. Shen. Space charge effect and mirror charge effect in photoemission spectroscopy. *Journal of Electron Spectroscopy and Related Phenomena* **142**, 27 (2005).
- [166] P. van Gelderen, S. Crampin, and J. E. Inglesfield. Quantum-well states in Cu/Co overlayers and sandwiches. *Physical Review B* **53**, 9115 (1996).
- [167] G. J. Mankey, R. F. Willis, and F. J. Himpsel. Band structure of the magnetic fcc pseudomorphs: Ni(100), Co(100), and Fe(100). *Physical Review B* **48**, 10284 (1993).
- [168] M. A. Mueller, A. Samsavar, T. Miller, and T.-C. Chiang. Probing interfacial properties with Bloch electrons: Ag on Cu(111). *Physical Review B* **40**, 5845 (1989).
- [169] E.G. McRae and M.L. Kane. Calculations on the effect of the surface potential barrier in LEED. *Surface Science* **108**, 435 (1981).
- [170] R. E. Dietz, E. G. McRae, and R. L. Campbell. Saturation of the image potential observed in low-energy electron reflection at Cu(001) surface. *Physical Review Letters* **45**, 1280 (1980).
- [171] F. J. Himpsel and J. E. Ortega. Electronic structure of Cu(100), Ag(100), Au(100), and Cu₃Au(100) from inverse photoemission. *Physical Review B* **46**, 9719 (1992).

- [172] N. Memmel. Monitoring and modifying properties of metal surfaces by electronic surface states. *Surface Science Reports* **32**, 91 (1998).
- [173] F. Forstmann. The concepts of surface states. *Progress in Surface Science* **42**, 21 (1993).
- [174] W. Jaskólski, V. R. Velasco, and F. García-Moliner. Electronic states in a metallic quantum well. *Physica Scripta* **43**, 337 (1991).
- [175] A. Beckmann, M. Klaua, and K. Meinel. Bound states in the sp-band gap of Ag/Au(111) thin films. *Physical Review B* **48**, 1844 (1993).
- [176] E. Rotenberg, Y. Z. Wu, J. M. An, M. A. Van Hove, A. Canning, L. W. Wang, and Z. Q. Qiu. Non-free-electron momentum- and thickness-dependent evolution of quantum well states in the Cu/Co/Cu(001) system. *Physical Review B* **73**, 075426 (2006).
- [177] N. J. Speer, S.-J. Tang, T. Miller, and T.-C. Chiang. Coherent electronic fringe structure in incommensurate silver-silicon quantum wells. *Science* **314**, 804 (2006).
- [178] A. M. Shikin, A. Varykhalov, G. V. Prudnikova, D. Usachov, V. K. Adamchuk, Y. Yamada, J. D. Riley, and O. Rader. Origin of spin-orbit splitting for monolayers of Au and Ag on W(110) and Mo(110). *Physical Review Letters* **100**, 057601 (2008).
- [179] S.-J. Tang, L. Basile, T. Miller, and T.-C. Chiang. Breakup of quasiparticles in thin-film quantum wells. *Physical Review Letters* **93**, 216804 (2004).
- [180] K. He, T. Hirahara, T. Okuda, S. Hasegawa, A. Kakizaki, and I. Matsuda. Spin polarization of quantum well states in Ag films induced by the Rashba effect at the surface. *Physical Review Letters* **101**, 107604 (2008).
- [181] T. Hirahara, T. Nagao, I. Matsuda, G. Bihlmayer, E. V. Chulkov, Yu. M. Koroteev, P. M. Echenique, M. Saito, and S. Hasegawa. Role of spin-orbit coupling and hybridization effects in the electronic structure of ultrathin Bi films. *Physical Review Letters* **97**, 146803 (2006).
- [182] F. G. Curti, A. Danese, and R. A. Bartynski. Experimental and model theoretical dispersions of unoccupied metallic quantum well states in the Cu/fccCo/Cu(100) system. *Physical Review Letters* **80**, 2213 (1998).
- [183] Y. Z. Wu, C. Y. Won, E. Rotenberg, H. W. Zhao, F. Toyoma, N. V. Smith, and Z. Q. Qiu. Dispersion of quantum well states in Cu/Co/Cu(001). *Physical Review B* **66**, 245418 (2002).
- [184] K. Giesen, F. Hage, F. J. Himpsel, H. J. Riess, W. Steinmann, and N. V. Smith. Effective mass of image-potential states. *Physical Review B* **35**, 975 (1987).
- [185] G. A. Burdick. Energy band structure of copper. *Physical Review* **129**, 138 (1963).
- [186] C. Westphal, A. P. Kaduwela, C. S. Fadley, and M. A. Van Hove. Photoelectron-diffraction effects and circular dichroism in core-level photoemission. *Physical Review B* **50**, 6203 (1994).
- [187] F. U. Hillebrecht, H. B. Rose, T. Kinoshita, Y. U. Idzerda, G. van der Laan, R. Denecke, and L. Ley. Photoelectron diffraction in magnetic linear dichroism. *Physical Review Letters* **75**, 2883 (1995).
- [188] D. Venus. Interpretation of magnetic dichroism in angle-resolved UV photoemission from valence bands. *Journal of Magnetism and Magnetic Materials* **170**, 29 (1997).
- [189] H. P. Oepen, K. Hünlich, and J. Kirschner. Spin-dependent photoemission intensities from solids. *Physical Review Letters* **56**, 496 (1986).
- [190] G. K. L. Marx, H. J. Elmers, and G. Schönhense. Magneto-optical linear dichroism in threshold photoemission electron microscopy of polycrystalline Fe films. *Physical Review Letters* **84**, 5888 (2000).
- [191] D. Weller, G. R. Harp, R. F. C. Farrow, A. Cebollada, and J. Sticht. Orientation dependence of the polar Kerr effect in fcc and hcp Co. *Physical Review Letters* **72**, 2097 (1994).

- [192] M. Born and E. Wolf. *Principles of optics*. Cambridge University Press, Cambridge (1999).
- [193] P. B. Johnson and R. W. Christy. Optical constants of transition metals: Ti, V, Cr, Mn, Fe, Co, Ni, and Pd. *Physical Review. B* **9**, 5056 (1974).
- [194] J. Braun. The theory of angle-resolved ultraviolet photoemission and its applications to ordered materials. *Reports on Progress in Physics* **59**, 1267 (1996).
- [195] J. Henk. Theory of low-energy electron diffraction and photoelectron spectroscopy from ultra-thin films in *Handbook of Thin Film Materials*. Editor: H. S. Nalwa. Academic Press, San Diego (2001).
- [196] R. Courths, H. Wern, G. Leschik, and S. Hüfner. Gap emission in ultraviolet photoemission experiments. *Zeitschrift für Physik B Condensed Matter* **74**, 233 (1989).
- [197] W. H. Rippard and R. A. Buhrman. Spin-dependent hot electron transport in Co/Cu thin films. *Physical Review Letters* **84**, 971 (2000).
- [198] A. Kaidatzis, S. Rohart, A. Thiaville, and J. Miltat. Hot electron transport and a quantitative study of ballistic electron magnetic imaging on Co/Cu multilayers. *Physical Review B* **78**, 174426 (2008).
- [199] M. P. Seah and W. A. Dench. Quantitative electron spectroscopy of surfaces: A standard data base for electron inelastic mean free paths in solids. *Surface and Interface Analysis* **1**, 2–11 (1979).
- [200] S. Ramakrishna and T. Seideman. Coherent spectroscopy in dissipative media: Time-domain studies of channel phase and signal interferometry. *The Journal of Chemical Physics* **124**, 244503 (2006).
- [201] G. Schönhense and H. C. Siegmann. Transmission of electrons through ferromagnets. *Annalen der Physik* **2**, 465 (1993).
- [202] J. Hong and D. L. Mills. Spin dependence of the inelastic electron mean free path in Fe and Ni: explicit calculations and implications. *Physical Review B* **62**, 5589 (2000).
- [203] M. Plihal, D. L. Mills, and J. Kirschner. Spin wave signature in the spin polarized electron energy loss spectrum of ultrathin Fe films: theory and experiment. *Physical Review Letters* **82**, 2579 (1999).
- [204] T. Balashov, A. F. Takács, W. Wulfhekel, and J. Kirschner. Magnon excitation with spin-polarized scanning tunneling microscopy. *Physical Review Letters* **97**, 187201 (2006).
- [205] S. F. Alvarado, R. Feder, H. Hopster, F. Ciccacci, and H. Pleyer. Simultaneous probing of exchange and spin-orbit interaction in spin polarized low energy electron diffraction from magnetic surfaces. *Zeitschrift für Physik B Condensed Matter* **49**, 129 (1982).
- [206] J. Kirschner. Temperature effects in spin-polarized low-energy electron diffraction from ferromagnets: Fe(110). *Physical Review B* **30**, 415 (1984).
- [207] J. N. Eckstein, C. Webb, S.-L. Weng, and K. A. Bertness. Photoemission oscillations during epitaxial growth. *Applied Physics Letters* **51**, 1833 (1987).
- [208] A. Laamouri, M. Djafari Rouhani, A. M. Gue, N. Fazouan, and D. Esteve. Photoemission applied to the *in situ* study of epitaxial growth: theoretical modelling. *Surface and Interface Analysis* **18**, 505 (1992).
- [209] J. Hong and D. L. Mills. Theory of the spin dependence of the inelastic mean free path of electrons in ferromagnetic metals: A model study. *Physical Review B* **59**, 13840 (1999).
- [210] H. Lüth. *Solid Surfaces, interfaces and thin films*. Springer, Berlin (2001).
- [211] T. A. Luce, W. Hübner, and K. H. Bennemann. Theory for spin-polarized oscillations in nonlinear optics due to quantum well states. *Physical Review Letters* **77**, 2810 (1996).
- [212] T. A. Luce, W. Hübner, A. Kirilyuk, Th. Rasing, and K. H. Bennemann. Theory for the nonlinear optical response of quantum-well states in ultrathin films. *Physical Review B* **57**, 7377 (1998).

- [213] R. Vollmer. Magnetization-induced second harmonic generation from surfaces and ultrathin films in *Nonlinear Optics in Metals*. Editor: K. H. Bennemann. Clarendon Press, Oxford (1998).
- [214] F. Bisio, A. Winkelmann, W.-C. Lin, C.-T. Chiang, M. Nývlt, H. Petek, and J. Kirschner. Band structure effects in surface second harmonic generation: the case of Cu(001). *Physical Review B* **80**, 125432 (2009).

Acknowledgment

This work can not be finished without support from many people. I would like to thank the longstanding scientific and financial support from Prof. Jürgen Kirschner, allowing me not only to learn how to complete the study but also to appreciate the necessary disciplines for doing research. Special thanks to Dr. Aimo Winkelmann for the fruitful discussion as well as taking care of me with the experiments. I would like to thank the invaluable technical assistance from Mr. Frank Helbig and Mr. Matthias Schröder.

In addition, I would like to thank the inspiring discussion with our friendly visitors. Discussion with Prof. Hrvoje Petek for the physics of photoemission and the common sense of aligning optics is extremely helpful. Doing experiments with Dr. Francesco Bisio is joyful not only in the sense of getting good results but also in the sense of knowing what to look for.

I would like to thank Prof. Minn-Tsong Lin in Taiwan for introducing me to the institute before the start of my study. Near the end of my study I enjoyed very much during the experiments the accompany of Mr. Mariusz Pazgan, Dr. Akin Ünal, and Mr. Martin Ellguth. I also would like to thank the critical discussion with Dr. Christian Tusche.

The strong support from the infrastructure, the workshops as well as the library of our institute is gratefully acknowledged. I also would like to thank Mrs. Neuber for her German classes.

Last but not at least importance, I would like to thank my family and friends.

Erklärung

Hiermit erkläre ich, dass ich die vorliegende Dissertation

Spin and magnetization dependent two-photon photomission
from ultrathin ferromagnetic cobalt films

selbständig und ohne fremde Hilfe verfasst und keine anderen als die von mir angegebenen Quellen und Hilfsmittel benutzt habe. Die den benutzten Werken wörtlich oder inhaltlich entnommenen Stellen sind als solche kenntlich gemacht.

Ich erkläre, dass ich mich früher nicht um den Doktorgrad beworben habe.

Halle (Saale), 30 Juni 2010
Cheng-Tien Chiang

Lebenslauf

Name: Chiang
Vorname: Cheng-Tien
Geburtsdatum: 26.06.1984
Geburtsort: Taipeh, Taiwan
Geschlecht: männlich
Familienstand: ledig

2002-2005 Physik-Studium an der National Taiwan University, Taipeh, Taiwan

2005-2007 Masterarbeit an der National Taiwan University, Taipeh, Taiwan
Thema: Morphology, electronic and magnetic structure of Mn/Cu₃Au(100)
studied by scanning tunneling microscopy and spectroscopy
Gutachter: Prof. Dr. Minn-Tsong Lin

seit 2007 wissenschaftlicher Mitarbeiter am Max-Planck-Institut für
Mikrostrukturphysik in Halle(Saale)
Thema: Spin and magnetization dependent two-photon photoemission
from ultrathin ferromagnetic cobalt films
Gutachter: Prof. Dr. Jürgen Kirschner

Publikationsliste

Artikel:

C.-T. Chiang, A. Winkelmann, P. Yu, J. Kirschner, J. Henk
Spin-orbit coupling in unoccupied quantum well states: Experiment and theory for Co/Cu(001)
Physical Review B **81** (11), 115130/1-9 (2010)

C.-T. Chiang, A. Winkelmann, P. Yu, J. Kirschner
Magnetic dichroism from optically excited quantum well states
Physical Review Letters **103** (7), 077601/1-4 (2009)

A. Winkelmann, W.-C. Lin, C.-T. Chiang, F. Bisio, H. Petek, J. Kirschner
Resonant coherent three-photon photoemission from Cu(001)
Physical Review B **80** (15), 155128/1-9 (2009)

F. Bisio, A. Winkelmann, W.-C. Lin, C.-T. Chiang, M. Nývlt, H. Petek, J. Kirschner
Band structure effects in surface second harmonic generation: the case of Cu(001)
Physical Review B **80** (12) 125432/1-8 (2009)

H. Mirhosseini, J. Henk, A. Ernst, S. Ostanin, C.-T. Chiang, P. Yu, A. Winkelmann, J. Kirschner
Unconventional spin topology in surface alloys with Rashba-type spin splitting
Physical Review B **79** (24), 245428/1-5 (2009)

A. Winkelmann, D. Hartung, H. Engelhard, C.-T. Chiang, J. Kirschner
High efficiency electron spin polarization analyzer based on exchange scattering at Fe/W(001)
Review of Scientific Instruments **79** (8), 083303/1-6 (2008)

W.-C. Lin, S.-S. Wong, P.-C. Huang, C.-B. Wu, B.-R. Xu, C.-T. Chiang, H.-Y. Yen, and M.-T. Lin
Controlled growth of Co nanoparticle assembly on nanostructured template Al₂O₃/NiAl(100)
Applied Physics Letters **89** (15), 153111/1-3 (2006)

M.-G. Lin, T.-L. Yang, C.-T. Chiang, H.-C. Kao, J.-N. Lee, W. Lo, S.-H. Jee, Y.-F. Chen, C.-Y. Dong, S.-J. Lin
Evaluation of dermal thermal damage by multiphoton autofluorescence and second harmonic generation microscopy
Journal of Biomedical Optics **116** (6), 064006/1-6 (2006)

Vortrag:

C.-T. Chiang, A. Winkelmann, J. Kirschner
Spin-polarized two-photon photoemission from Co/Cu(001) via unoccupied quantum well states
Spring meeting of the German physical society (DPG)
Regensburg, Germany, 2010

C.-T. Chiang, A. Winkelmann, J. Kirschner
Magnetic circular dichroism in two-photon photoemission from Co/Cu(001)
Spring meeting of the German physical society (DPG)
Dresden, Germany, 2009

C.-T. Chiang, A. Winkelmann, J. Kirschner
Real time observation of multiphoton photoemission and surface second harmonic generation during the growth of Fe on Cu(001)
Spring meeting of the German physical society (DPG)
Berlin, Germany, 2008

Poster:

C.-T. Chiang, A. Winkelmann, J. Henk, P. Yu, J. Kirschner
Unoccupied quantum well states in ultrathin cobalt films studied by two-photon photoemission
Ultrafast phenomena in cooperative systems, Gordon research conference
Galveston, Texas, USA, 2010

C.-T. Chiang, A. Winkelmann, P. Yu, J. Kirschner
Study of magnetic dichroism in two-photon photoemission from ultrathin cobalt films
20th International colloquium on magnetic films and surfaces
Berlin, Germany, 2009
(poster prize)

C.-T. Chiang, A. Winkelmann, F. Bisio, W.-C. Lin, H. Petek, J. Kirschner
Three-photon photoemission from Cu(001) studied with spin and time resolution
6th conference on ultrafast surface dynamics
Kloster Banz, Germany, 2008